Molekulare Mechanismen in Zelldifferenzierung und Zellteilung

Molecular Mechanisms in Cell Differentiation and Cell Division

DISSERTATION

der Fakultät für Chemie und Pharmazie
der Eberhard-Karls Universität Tübingen

zur Erlangung des Grades eines Doktors
der Naturwissenschaften

2006

vorgelegt von

Arminja Nadine Kettenbach

Die vorliegende Arbeit wurde unter der Anleitung von

Prof. Dr. Frank D. McKeon

in der Zeit von März 2003 bis August 2006, am Institut für Zellbiologie an der Harvard Medical School, Boston, USA, durchgeführt.

Prof. Dr. Hans-Georg Rammensee vom Interfakultären Institut für Zellbiologie, Abteilung Immunologie, Eberhard-Karls-Universität Tübingen, Deutschland, übernahm die Vertretung der Arbeit vor der Fakultät fuer Chemie und Pharmazie der Eberhard-Karls-Universität Tübingen.

WIDMUNG

Meiner Mutter in grosser Dankbarkeit gewidmet.

Table of Contents

Part I – Mice deficient for TA-p63

Part II – Checkpoint signaling

Abbreviations

For amino acids the suggestions of the IUPAC-IUB-commission for biological nomenclature [*Eur. J. Biochem.* **1984**, *138*, 9-37] were applied.

AER	apical ectodermal ridge
AMP-PNP	adenylylimidodiphosphate
Amp	ampicillin
APC	anaphase-promoting complex
APS	ammonium persulfat
ATP	adenosine triphosphate
BSA	bovine serum albumine
Bub	budding inhibited by benomyl
BubR1	Bub-related 1
C	carbon
Ca	calcium
Car	carbenicillin
cDNA	complementary DNA
CDK	cyclin-dependent kinase
Cl	chlor
CK	cytokeratin
CRS	cytoplasmic retention signal
DAB	diaminobenzidine tetrahydrochloride
DAPI	4',6-diamidino-2-phenylindole dihydrochloride
DEAE	diethylaminoethane
DMEM	Dulbecco´s Modified Eagle's Medium
DMP	dimethylpimelimidate
DMSO	dimethylsulfoxide
∆N-	non-transactivating
DNA	deoxyribose nucleic acid
DNase	deoxyribonuclease
dNTP	desoxyribonucleosidtriphosphate
DTT	dithiothreitol
E. coli	*Escherichia coli*
EDTA	ethylenediaminetetraacetic acid
et al.	and others
EtOH	ethanol
FACS	fluorescence activated cell sorting
FIAU	1-(2-Deoxy-2-fluoro-ß-D-arabinofuranosyl)-5-iodouracil
Fig.	figure
FSH	follicle stimulating hormone
FTICR	Fourier-transform ion cyclotron resonance
FT-MS	Fourier-transform mass spectrometry
GFP	green fluorescent protein
Hec1	Highly expressed in cancer
HEPES	N-[2-Hydroxyethyl]piperazine-N'-[2-ethanesulfonic acid]
Hr	hour
HRP	horseradish peroxidase
Ig	immunglobulin

IPTG	isopropyl-β-D-thiogalactopyranoside
λ	wavelength
LB	Luria-Bertani
K1	Keratin 1
K5	Keratin 5
K8	Keratin 8
K10	Keratin 10
K14	Keratin 14
K18	Keratin 18
kDa	kilo Dalton
KO	knock-out
LH	Luteinizing hormon
M	molar
Mad	mitotic arrest deficient
MeOH	Methanol
Mg	magnesium
min	minute
MOPS	3-(N-Morpholino)propanesulfonic acid
mRNA	messenger RNA
MS	mass spectrometry
MW	molecular weight
m/z	mass/charge ratio
N	nitrogen
Na	sodium
Neo	neomycin resistant gene
OD	optical density
ORF	open reading frame
P	phosphor
PAGE	Polyacrylamide-Gel-Electrophoresis
PBS	phosphate-buffered saline
PCR	Polymerase Chain Reaction
PEG	polyethylene glycol
PGK	phosphoglycerol kinase
PI	propidium iodide
PP2A	protein phosphatase 2A
PVDF	polyvinylidenfluoride
RNA	ribonucleic acid
RNase	ribonuclease
rpm	rounds per minute
RP-HPLC	reversed-phase high-performance liquid chromatography
RT	room temperature
SAM	sterile-alpha motif
SDS	sodium dodecylsulfate
Sgo	shugoshin
siRNA	small interfering RNA
SMC	structural maintenance of chromosome
t	time
TA	transactivating
TBS	tris-buffered saline

TBST	tris-buffered saline with Tween
TEMED	N,N,N',N'-tetramethylethylenediamin
TID	transactivation inhibitory domain
TK	thymidine kinase
Tris	tris(hydroxymethyl)aminomethane
μLC	micro liquid chromatography
V	volume
WT	wild-type

PART I - Mice deficient for TA-p63

1.   Summary

p63 is one of three members of the p53 family of transcription factors. Transcription of the p63 gene gives rise to two different N-terminal isoforms, one with (TA-p63) and one without (ΔN-p63) a transactivation domain. Analysis of p63 protein expression in tissues and of mice deficient for all p63-isoforms revealed a function of p63 in epithelial, craniofacial, and limb development. The significance of p63 in epidermal development is further highlighted by the discovery of p63 germline mutations in severe human syndromes with limb defects and ectodermal dysplasia.

Interestingly, the interpretation of p63 function in epidermal development is still controversial. On one hand, p63 is discussed as a commitment factor for the embryonic ectoderms to epidermal lineage, while on the other hand, it is suggested that p63 is a stem cell factor involved in maintenance of proliferative potential and regeneration of epidermal stem cells. Furthermore, there are different opinions about the relative significance of TA- and ΔN-p63 in the commitment to epidermal lineages and in epidermal differentiation.

Recently, studies in mice deficient for more than one p53 family member were conducted to reveal potential cross-regulation between them. Moreover, TA-p63 was found to be implicated in the protection of the female germline by inducing cell death in oocytes upon gamma-irradiation.

The work presented here investigates the function of TA-p63 in the commitment of embryonic ectoderm to epidermal lineages and epithelial development to resolve the controversy about the relative significance of TA- and ΔN-p63 in this process.   Furthermore, phenotypic abnormalities observed in TA-p63(-/-) are described.

2. Introduction

2.1 The gene structure of p63

The p63 (KET, p51, AIS) gene is a recently discovered homologue of the tumor-suppressor p53 [1-4], the most frequently mutated or inactivated gene in human cancer (>50% of all human cancers), and the third member of the p53-protein family, which also includes p53 and p73 [5].   Although the general domain structure of p53, which includes amino-terminal transactivation, DNA-binding and carboxyl-terminal oligomerization domains, is conserved in p63, the p63 gene structure is far more complex than that of p53 [1-4]. The p63 gene gives rise to many different transcripts by utilizing two independent promoters as well as alternative mRNA splicing at its 3' end (Fig.1).

The p63 gene is located on human chromosome 3q27-3q28 and contains 15 exons spread over 200kb. A promoter upstream of exon 1 gives rise to transcripts that contain a p53-like TA-domain. An additional class of TA-isoforms, TA*-transcripts with a 39 amino acid long amino-terminal extension, were found in cDNA libraries from mouse embryos, rat and human tissues [1, 13]. Transcripts with a truncated amino terminus (ΔN-p63) originate from a promoter located in intron 3. While the TA-p63 isoforms are likely to act in a p53-like manner in gene transcription, the ΔN-p63 isoforms are thought to have opposite effects and to function as dominant-negatives towards p53 and TA-p63 isoforms [14].

Besides differential promoter usage, additional p63 gene products are generated by alternative splicing of the carboxyl-terminus. At least three different isoforms (α, β, and γ) have been detected for TA- and ΔN-p63. While all carboxyl-terminal isoforms contain the DNA-binding and oligomerization domains, only the longest α-isoforms contains an additional sterile α-motif (SAM) and transactivation inhibitory (TI) domain [15, 16]. SAM-domains are shown to mediate protein-protein interactions. The TI domain is p63/p73 specific and located carboxyl-terminal from the SAM domain. In transactivation assays, the TI domain was shown to inhibit TA-p63α transcriptional activity, possibly via an intramolecular mechanism [15].
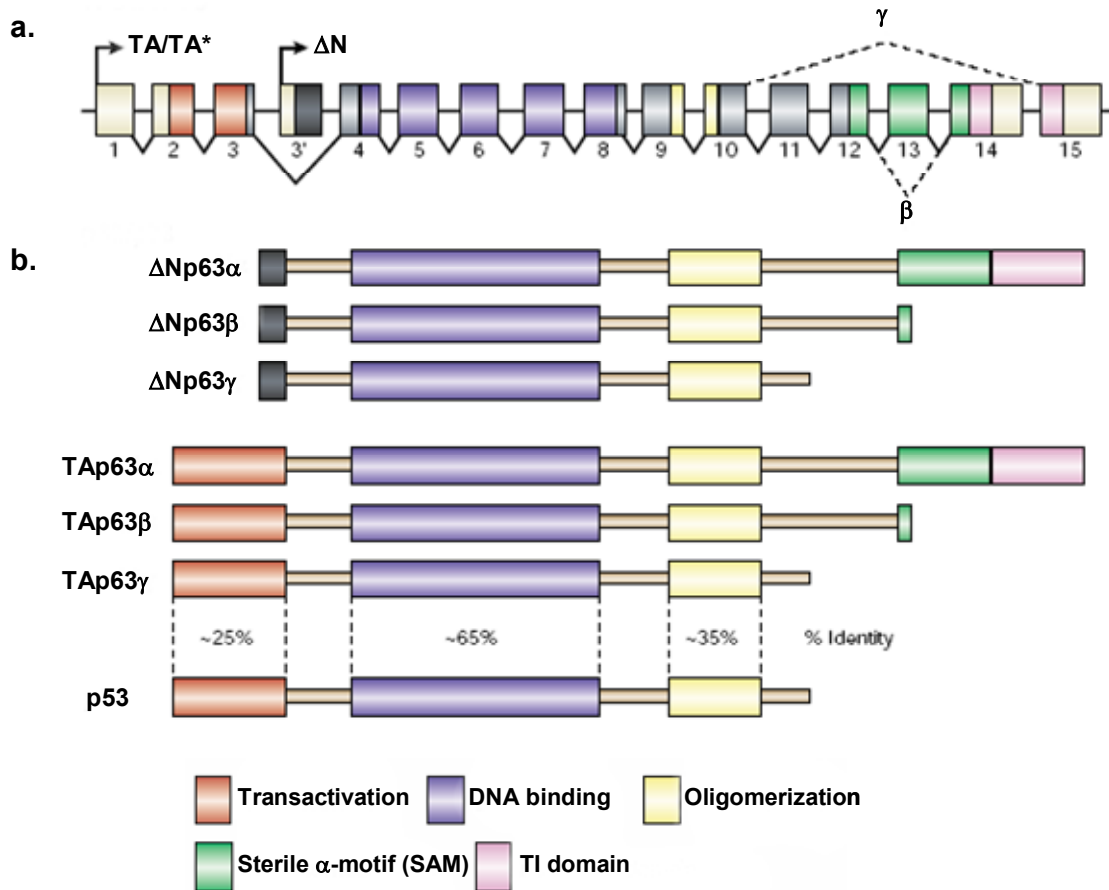
Figure 1 **Gene structure of p63. a.** Intro-exon structure of the human p63 gene. The 15 exons (boxes) of p63 are spread over more than 200kb with intron sizes ranging from few hundred base pairs to 40kb. Transcription of the TA/TA*-isoforms is initiated from a promoter upstream of exon 1. ΔN-mRNA-isoforms are initiated from a cryptic promoter in intron 3. The splicing patterns of the α, β, and γ isoforms are displayed. *Arrows* indicate transcriptional starts. **b.** Domain structure of p53, TA- and ΔN-p63 isoforms with transactivation (TA), DNA binding, oligomerization, sterile α-motif (SAM), and transactivation inhibitory (TI) domain. Adapted from [14].

In its structure and transcriptional activity, TA-p63γ seems to be the most p53-like p63 isoform. In transactivation assays with p53 reporter genes, TA-p63β and γ show transcriptional activation. Conversely, TA-p63α had only minor effects on induction of reporter gene expression due to the inhibitory effect of the TI domain [1, 3, 15]. Furthermore, heterologous overexpression of TA-p63β and γ, but not TA-p63α, induces apoptosis. While TA-p63 isoforms can exhibit p53-like behavior in transactivation and transfection assays, ΔN-p63 isoforms act in a dominant-negative manner towards p53 and TA-p63 isoforms [1].

2.2 Expression of p63

TA- and ΔN-p63 isoforms differ significantly in expression level and pattern. Immunohistochemical analysis of p63 expression with the pan-p63 mouse monoclonal antibody 4A4 in humans and mice revealed strong nuclear staining in the basal layer of epithelial tissues such as the epidermis, cervix, vagina, urogenital tract, prostate, myoepithelium of the breast, and glandular tissue [1, 10] (Fig. 2). Analysis of mRNA expression and protein size in these tissues indicate predominant presence of ΔN-p63α.
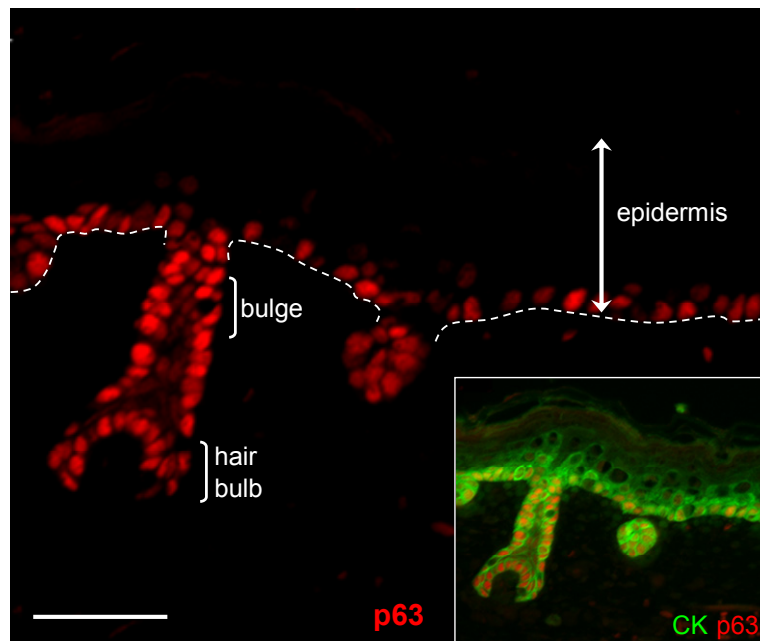
Figure 2 **p63 expression in the basal layer of the epidermis.** Immunofluorescence of newborn mouse epidermis stained with p63 (red) and pan-cytokeratin (green, inset). *bulge*, the bulge of the hair follicle. The dotted line indicates the border between the epidermis and the dermis. Bar, 50μm.

Using TA-p63 specific antibodies (6E6 and 4B2), TA-p63 was detected in the thyroid gland and ovary. p63 expression was previously reported in female and male reproductive organs [17]. Using a ΔN-p63-specific antibody, Kurita et al. were able to detect ΔN-p63 in prostate, cervical, and vaginal epithelium, but not in testis and ovary, which stained positive with a pan-p63 (4A4) antibody, suggesting TA-p63-specific expression. Indeed, TA-p63 expression in the ovaries could be confirmed using a TA-p63-specific antibody, while no TA-p63 staining was detected in testis (Suh et al, submitted). It is likely that the p63

staining found in testis is due to a previously observed cross-reactivity of the pan-p63 antibody with a testis-specific protein (M. Senoo, personal communication).

2.3   Skin morphogenesis and organization

The skin is the body's largest organ, and protects it against dehydration, temperature changes, infection, and injury. Skin consists of the dermis and epidermis separated by the basal lamina. During development, a highly proliferative, single-layered ectoderm covers the surface of the embryo and eventually differentiates into keratinocytes. Papilla cells, derived from the dermal mesenchymal cells, induce hair follicle formation [18-20] The mature epidermis is a stratified squamous epithelium (Fig. 3) in which proliferation is restricted to stem cells and transient-amplifying cells in the interfollicular basal layer and in the bulge of the hair follicle [21]. Stem cells in the basal layer give rise to stratified layers, while those in the hair follicle are required for the continuous renewal of hair and sebaceous glands [20].   Keratinocytes are the major cell type of the epidermis. They originate from the stem cells in the basal layer and undergo squamous differentiation until they reach the stratum corneum.

The stem cells in the interfollicular basal layer undergo asymmetric cell division into a daughter stem cell and a transient amplifying cell [22]. Transient amplifying cells go through additional but limited rounds of cell division, before they differentiate [23]. Both stem cells and transient amplifying cells are characterized by the expression of keratin 8 (K8) and 18 (K18). Furthermore, induced by signals from the underlying mesenchyme, keratinocytes in the basal layer of the epidermis express keratin 5 (K5) and keratin 14 (K14). During mouse embryogenesis, this process starts around day e9.5 and by day e14.5, all epidermal cells express K5 and K14, which is restricted to cells with proliferative potential and is down-regulated upon differentiation [18].

As cells become differentiated and move into suprabasal layers, they strengthen their cytoskeleton, become connected by desmosomes, and start to express K1 and K10 (lower and upper spinous layer), involucrin (upper spinous), profilaggrin   and loricin (granular layer), and filaggrin (stratum corneum). Filaggrin bundles keratins into macrofibrils to make them more resistant to mechanical stress and to give them more tensile strength [24, 25].
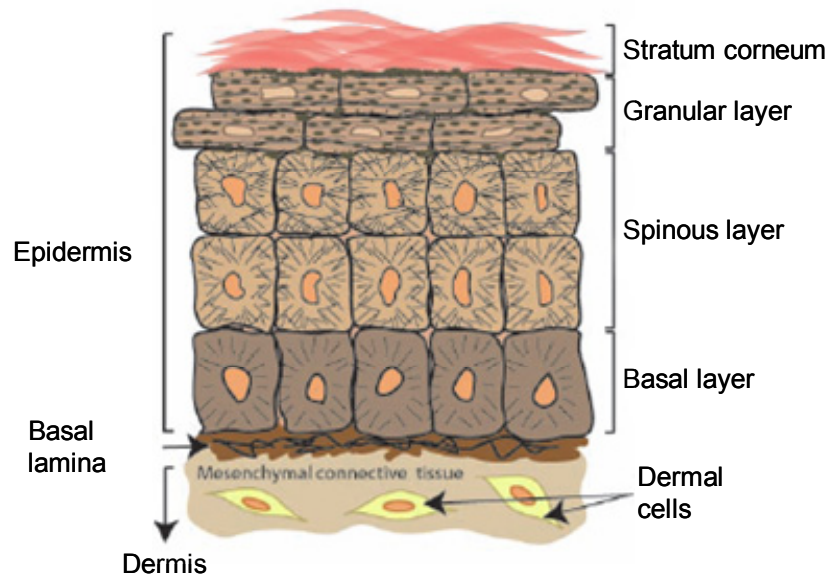
Figure 3 **Histology of skin.** Skin consists of epidermis and dermis which are separated by the basal lamina. Mitotically active cells only exist in the basal layer. As cells differentiate and move outward into the spinous layer, they stop dividing and start to produce cytoskeletal proteins and intercellular connections (desmosomes). This process is completed when cells reach the granular layer where they start to produce an epidermal barrier that protects the body from dehydration and environmental stress before they undergo cell death. These dead proteinaceous cell sacs, squames, form the stratum corneum and are eventually sloughed off. Adapted from [20].

Furthermore, glutamine- and lysine-rich proteins such as involucrin and loricrin are crosslinked in isopeptide bonds by epidermal transglutaminase to form the cornified envelope [26]. During the terminal differentiation process, cells in the stratum corneum undergo programmed cell death and become dead proteinaceous sacs (squames), which eventually detach [27]. In mice, the differentiation process from basal layer to squames takes between 10 and 14 days, demonstrating the great proliferative potential of epidermal stem cells [28].

p63 is highly expressed in the interfollicular basal layer as well as in the bulge and bulb of the hair follicle. As cells differentiate and move outward to the surface of the skin, p63 expression is down-regulated. Recently, p63 was implicated in cell adhesion and loss of p63 expression was shown to lead to loss of adhesion [29]. However, it is not known if downregulation of p63 expression is required for detachment from the basal lamina during stratification.

2.4   Oocyte development and TA-p63

Around day e10 of mouse embryogenesis, primordial germ cells (PGCs) migrate to the gonadal ridge and thereby undergo approximately eight cell cycles to generate a pool of 20,000 germ cells. In the developing female gonad, PGC differentiate into oogonia and further into oocytes. At day e.13.5, oogonia enter meiosis, develop into primordial oocytes, and pass through the leptotene, zygotene and pachytene stages of prophase I before they arrest in the diplotene stage (dictyate arrest) of prophase I around the time of birth [30]. Just before birth, when primordial oocytes are in the zygotene or pachytene stage, the first wave of oocyte death occurs, leaving only 20-30% of the initial number of oocytes behind to be enclosed within follicular granulosa cells (primary follicles). Likely reasons for this oocyte death include growth factor depletion and errors during meiotic cross-overs. For instance, it was shown that mice deficient for enzymes involved in DNA repair and recombination (ATM [31], msh4 and 5 [32, 33], dmc1 [34]) undergo massive oocyte death in the last stages of prophase I.

Furthermore, female mice lacking one X chromosome (XO) (most likely due to failure in chromosome pairing) and humans with Turner (XO) syndrome, undergo massive oocyte death in the fetal ovary [35, 36]. Stimulated by growth factors, the granulosa cells start to proliferate and form a larger follicle (antral follicle) with a cavity (antrum) filled with proteineaous fluid. The oocyte of an antral follicle is still in dictyate arrest and now surrounded by several layers of granulose cells [37]. As the oocyte matures, it requires gonadotropic hormones for its survival. At the stage of the menstrual cycle when levels of follicle stimulating hormone (FSH) are rising, the follicle enters into another growth period, before upon expression of luteinizing hormone (LH) the dictyate arrest is broken and the oocyte finishes meiosis I. With increasing secretion of estrogen, FSH level decline while LH levels still rise, leading to ovulation of the oocyte. After ovulation the remains of the follicle become the corpus luteum and regress (Fig. 4).
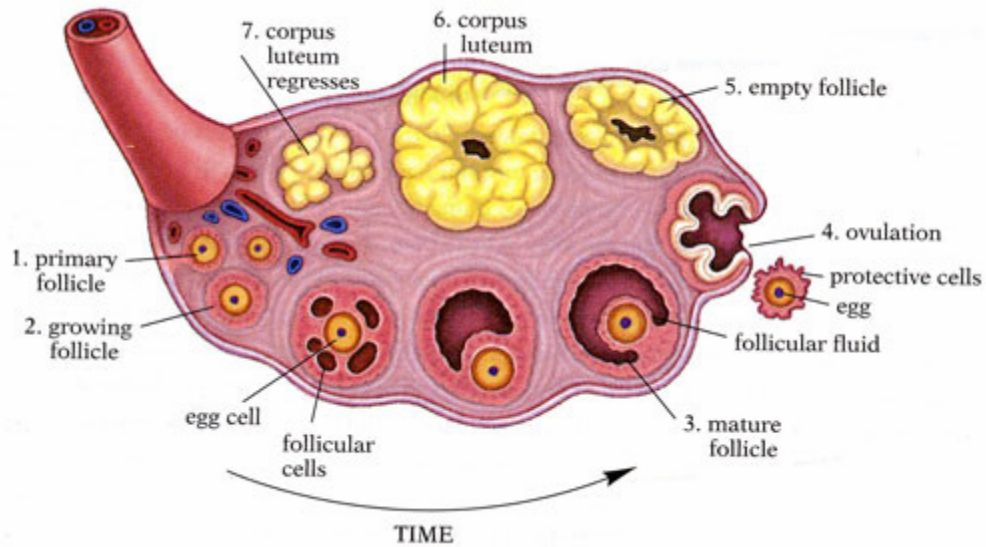
Figure 4 **Oocyte development in the ovary.** Oocytes (egg cells) are enclosed within a follicle of granulose cells that proliferate and form during maturation a multi-layered follicle with fluid-filled cavity. Upon hormonal stimulation ovulation and the remains of the follicle form the corpus luteum and regress. Adapted from (http://instruct1.cit.cornell.edu/courses/biog105 /pages/ demos/ 105/unit8/media/ovary-schematic.jpg)

p63 is expressed early during development in PGCs in undifferentiated gonads. In the mature ovary, p63 expression is highest in primordial oocytes [17]. Using antibodies specific for the TA-domain and the α-tail, we were able to show that TA-p63α is the predominately expressed p63 isoform (Suh et al. submitted). Although p63-deficient mice lack p63 expression in PGC's as well as in oocytes, ovaries from p63-deficient mice developed normally until birth and even further when transplanted under the renal capsule of ovariectomized adult female nude mice [17] (Suh et al, submitted). These observations suggest that p63 is not essential for development and maturation of oocytes into primordial, primary, and secondary follicles, nor corpus luteum.

2.5   Mice deficient for all p63 variants

In 1999, two research laboratories independently generated mice deficient for all p63 isoforms [9, 10]. While Mills et al. generated a p63 deletion by gap repair gene targeting using targeting vectors isolated from previously made library [11], Yang et al. chose a classic homologous recombination approach to

specifically replace exon 6 to 8 with the neomycin resistance gene. Both laboratories found that p63 knockout mice are born alive, but die within hours after birth due to desiccation. The animals have severe defects in epithelial, craniofacial, and limb development (Fig. 5). The epidermis of p63-deficient mice does not stratify and hair follicles and vibrissae are absent. Epithelial appendages like mammary, sebaceous, lachrymal, and salivary glands as well as teeth primordia do not develop. Other stratified epithelia such as that on the tongue, esophagus, and anterior portions of the stomach, cervix, and vagina do exist, but show aberrant differentiation. Furthermore, the forelimbs of p63 knockout mice are truncated and the hindlimbs are completely absent.
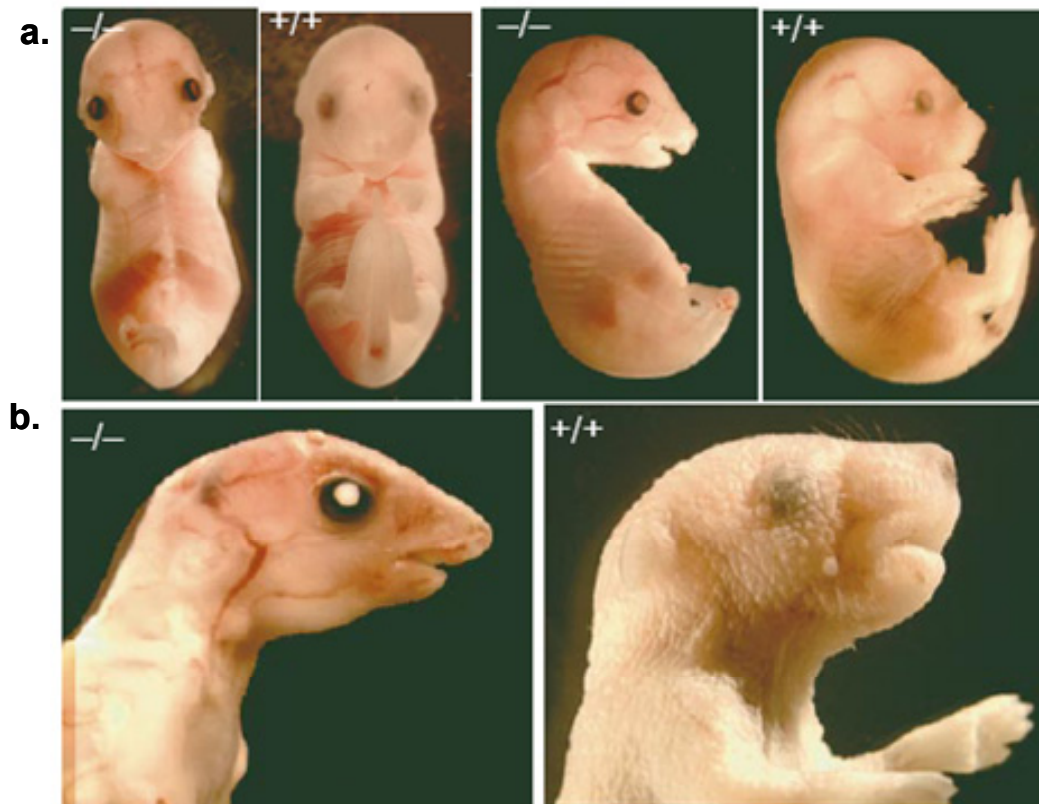
Figure 5   **Mice deficient for all p63-isoforms. a.** Front and side view of wild type and p63-deficient embryos at day e17. Note forelimbs are truncated and hindlimbs are missing.   **b.** Wild type and p63-deficient embryos one day after birth (P1). p63-/- mice have hypoplastic upper and lower jaws. Eyelids, whisker pads, epidermis, vibrissae, pelage follicles and hair shafts are absent. (From [10]).

Many of the observed phenotypes including the limb defects are related to a lack of or insufficient epithelial differentiation and stratification. Limb outgrowth and proximo-distal patterning is initiated early during embryogenesis (day e10.5) by signaling from the apical ectodermal ridge (AER), a thickened ectoderm that covers the tip of the limb bud. In p63-deficient mice, no thickening of the ectoderm and formation of the AER is observed, resulting in severe limb defects.

Although both laboratories observed similar phenotypes, the conclusions they drew from these observations were very different. In their analysis of the epidermis of p63-deficient mice, Mills et al. detected faint staining of keratin 14 (K14), an epidermis-specific marker that is expressed in proliferating keratinocytes [38], but were unable to detect markers of stratified epithelia such as K1, K6, or K10 [39], or markers of terminal differentiation such as loricrin [40, 41] and filaggrin [41, 42]. From the lack of epidermal differentiation and stratification, as well as the absence of epidermal appendages, they concluded that the epidermis of p63-deficient mice does not develop beyond the stage observed on day e9.5. As a result, Mills et al. postulated that p63 is essential for commitment to the epidermal lineage [9, 43].

Yang et al. came to a different conclusion in their investigation of the epidermis of p63-deficient mice. Although they were not able to detect the early differentiation marker K5 (in a later analysis K5 was detected in the epidermis of p63-deficient mice from the laboratory of Frank McKeon, Pinto et al. unpublished observation), Yang et al. found patches of epidermal cells that stained positive for loricrin and involucrin [44] (Fig. 6). Therefore, they concluded that epidermal differentiation and stratification occur in p63-deficient mice and that the observed phenotype results from a depletion of the epidermal stem cell population that lost its self-renewal capacity. They suggest that high p63 expression in epidermal progenitor cells is required for the maintenance of their proliferative potential and that in p63-deficent mice, these cells have lost their self-renewal capacity [10, 14, 45, 46]. This hypothesis is further supported by the observation that conditional ablation of p63 in adult mice causes cellular senescence and accelerated aging [47].
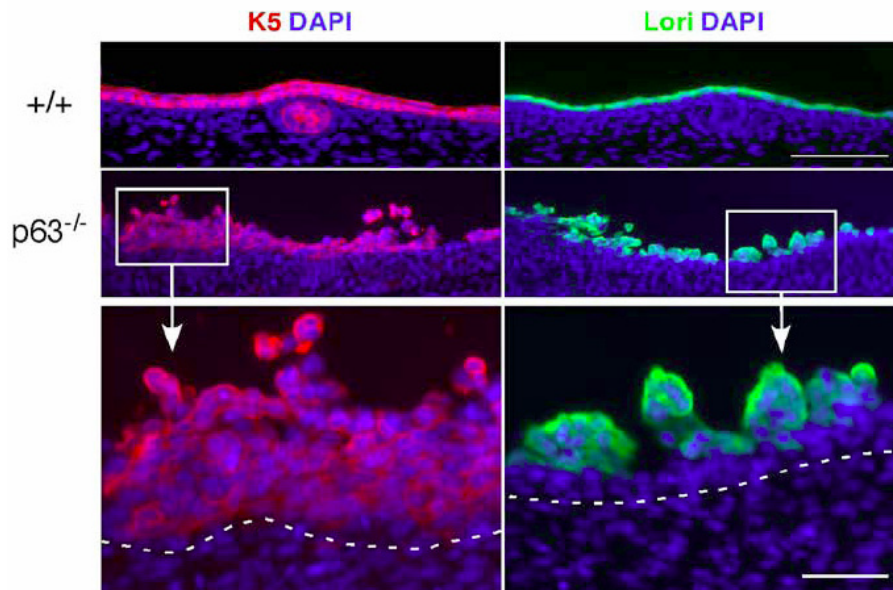
Figure 6 **Expression of differentiation markers in the epidermis of wild type and p63-deficient mice.** Immunofluorescence micrographs of loricrin (Lori, green) and keratin (K5, red) in wild type (top panel) and p63-/- epidermis on day e.16.5. DNA is stained with DAPI (blue). Bar, 200μm. Bottom panels show enlarged view of the insets in middle panel. The dotted lines indicate the border between the epidermis and the dermis. Scale bar is 50μm. (From Pinto et al., submitted)

2.6   TA-p63 *versus* ΔN-p63

Further analysis of p63 function in skin by the laboratory of Dennis Roop led to the observation that, during embryogenesis, TA-p63α is the earliest expressed p63 isoform and that TA-p63α is essential for the commitment of the embryonic ectoderm to epidermal lineages as well as for the initiation of stratification [12]. Therefore, they concluded that the simple epithelium observed in the p63-knockout mouse by Mills et al. is a consequence of the lack of TA-p63α expression. Koster et al. found that only TA-p63α, not ΔN-p63α, was able to induce expression of the early differentiation markers K5 and K14 in epithelial cell lines of different origin. Specifically, they generated transgenic mouse models expressing TA-p63α and ΔN-p63α *in vivo* in the single-layered epithelia of the bronchioles of the lung, which normally do not show p63, K5 or K14 expression, and found that, in this system, only TA-p63α was able to induce squamous metaplasia expressing K5 and K14. As with stratified epithelia during

development, squamous metaplasia is the result of a transition from a single-layered epithelium to a stratified epithelium [48]. Targeted expression of TA-p63α under the K14 promoter in the epidermis from day e8.5 induced hyperplasia of keratinocytes and expression of immature makers in the stratified layer of the epidermis, indicating a delay in the onset of squamous differentiation. Based on these results Koster et al. proposed that TA-p63α is required and sufficient for initiating commitment to the epidermal linage and stratification, but inhibits terminal differentiation and thereby keeps keratinocytes in an immature state. They also suggest that the function of ΔN-p63α, after commitment to the ectodermal linage, is to offset TA-p63α in order to allow stratification and commitment to terminal differentiation [12, 49]. Continued expression of ΔN-p63α in the basal layer of stratified epithelia is essential for their self-renewal capacity and its downregulation is required for induction of terminal differentiation and stratification [12, 49].

Candi et al. tried to complement p63-deficient mice with expression of TA-p63α and ΔN-p63α transgenes under the control of the K5 promoter. Their study showed that the expression of ΔN-p63α led to greater epithelialization and expression of K14 and filaggrin than the expression of TA-p63α [50]. Expression profiling of Saos-2 cells with inducible expression of TA-p63α or ΔN-p63α showed that TA-p63α mainly regulates terminal differentiation markers such as K1, K10, profilaggrin and involucrin, while ΔN-p63α induced the early differentiation marker K14.

2.7   Germline mutation of p63 in human syndromes

While p63 mutations are rarely found in tumors, p63 germline mutations were shown to be the underlying cause of severe human syndromes with limb defects and ectodermal dysplasia, such as Ectrodactyly Ectodermal-Dysplasia-Clefting Syndrome (EEC), Acro-Dermato-Ungual-Lacrimal-Tooth malformation (ADULT), Hay-Wells syndrome or Ankyloblepharon (AEC), Limb-Mammary Syndrome (LMS), Split-Hand/Foot Malformations (SHFM), and Rapp-Hodgkin Syndrome [51, 52]. In all of these cases p63, mutations were heterozygous and

likely act as dominant-negative or gain of function alleles, rather than by haploinsufficiency.

In the case of EEC, nearly all mutations were amino acid substitutions in the DNA binding domain, which reduced the DNA-binding capacity of all-p63-isoforms [53]. In LMS, frame-shift mutations were located in exon 13 and 14 and resulted in truncated protein products missing the TID and parts of the SAM domain of the α-isoform. However, the β and γ isoforms are not affected from these mutations [52]. In AEC, missense mutations are present in the SAM domain that could abolish protein-protein interactions [54]. In ADULT syndromes, mutations affect only ΔN-p63 isoforms. However, in one ADULT patient an unusual mutation in the DNA binding domain which seems to affect transactivation was also found [55, 56]. In less than 10% of SHFM patients, p63 mutations were discovered with variable effects on DNA binding [52].

In summary, most of the mutations found in these syndromes are clustered in the DNA binding domain (EEC) and SAM domain (AEC). Although all syndromes have an overlapping spectrum of defects in ectodermal development affecting limbs, epidermis and its appendages, they also show phenotypical peculiarities which establish a clear genotype-phenotype correlation and reveal distinct functions of p63 and its domains in ectodermal development. Interestingly, many of the identified p63 point mutations are located in regions where p53 inactivating mutations are commonly found such as the DNA-binding domain [14].

2.8   Functional interactions of p53 family members

Although the overall gene structure of p53 with transactivation, DNA-binding, and oligomerization domains are conserved in p63 and p73, an obvious role of the latter two genes as tumor suppressors was not found [14]. However, hints of an involvement of p63 and p73 in p53-dependent processes such as apoptosis are slowly emerging. As described for p63, transcription of the p73 gene gives rise to TA- and ΔN-p73 isoforms with likely opposite functions in regulation of gene transcription. Mouse embryonic fibroblasts deficient for p63 and p73 are impaired in p53-dependent BAX, PERP, and NOXA gene

expression following DNA damage [57]. While p53 was still able to bind to the promoters of growth arrest genes such as p21/WAF and mdm2, no stable association with bax, PERP, and NOXA promoters was observed.   Furthermore, Flores et al. found that upon γ-irradiation, apoptosis in the central nervous systems of p63-/-;p73-/- embryos was similarly impaired as in p53-/- embryos [57]. Investigations of the tumor spectrum in p63+/- and p73+/-, as well as p53+/-;p73+/-, p53+/-;p63+/-, and p63+/-;p73+/- mice showed that instead of lymphomas and sarcomas as seen in p53 mutants, p63 and p73 heterozygotes mainly developed carcinomas and showed signs of premature aging [58]. Mice heterozygous for p53;p63 or p53;p73 developed a more severe and aggressive tumor phenotype with a higher, more metastatic tumor burden. The underlying cause of tumorgenesis in p63- and p73-deficient mice is unclear and analysis of human tumors found that, in some cases, TA-isoforms are upregulated and ΔN-isoforms are down regulated, while others show the opposite [59, 60].

In addition, *in vitro* studies showed that TA-isoforms of p63 and p73 can bind and transactivate a p53 reporter gene, but the significance *in vivo* is unknown [14]. High levels of ΔN-p63 in keratinocytes might act as a dominant-negative against p53; however, upon UV-irradiation, ΔN-p63 levels decrease while p53 is stabilized and induces apoptosis. In a similar fashion, ΔN-p73 might inhibit the apoptotic activity of p53 in sympathetic neurons [61]

These studies illustrate the potential of cross-regulation of TA- and ΔN-isoforms of each gene as well as between the family members and highlight the complex nature of the functional interactions among p53 family members.

3.   Results

3.1   Generation of TA-p63 deficient mice

To investigate the function of TA-p63 *in vivo*, expression of all TA-p63 isoforms was disrupted by homologous recombination in mouse embryonic stem (ES) cells. TA-p63(+/-) ES cells were injected into blastocyts and implanted into pseudo-pregnant foster mothers to generate chimeric mice. Chimeric mice were crossed with wild type mice to achieve germline transmission of the mutant TA-p63 allele.

The murine p63 gene is located on chromosome 16 and spreads over >200kb (Fig. 7). While a promoter in front of exon 1 gives rise to TA-p63 transcripts, a second promoter in intron 3 initiates ΔN-p63 transcription. Transcripts of exon 1 are only found in TA*-p63, where as exon 2 and 3 are common in all TA*/TA-p63 transcripts, but absent in ΔN-p63. While TA- and ΔN-p63 are detectable at protein level, TA*-p63 is only found as mRNA and likely to be untranslated.
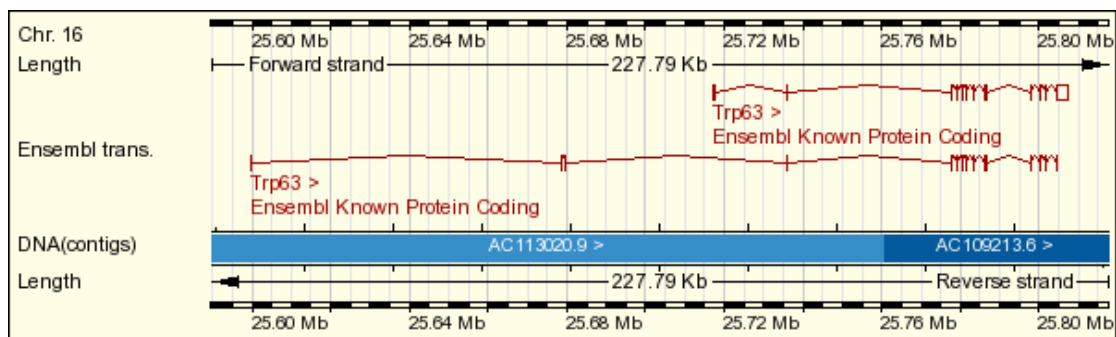
Figure 7   **Genomic organization of murine TA- and ΔN-p63.** The transcriptional start of the TA-p63 isoforms is in front of exon 1. A second promoter in intron 3 gives rise to ΔN-p63 isoforms. Intron 1 (78.9kb), intron 3 (56kb), and intron 4 (41.6kb) are very large. (From http://www.ensembl.org/Mus_musculus/geneview?gene=ENSMUSG00000022510)

To generate a mouse specifically lacking TA-p63 transcripts, exon 2 and 3 of the p63 gene were replaced by a neomycin resistance gene using homologous recombination. Since the transcriptional start of ΔN-p63 is located 38kb downstream of exon 3, it is likely that deletion of exon 2 and 3 would not affect ΔN-p63 promotor activity and thereby ΔN-p63 transcription.

3.2   The TA-p63 targeting construct

To generate the targeting construct, a previously isolated ~15 kb phage clone containing exons 2 and 3 and flanking introns from a 129/SvJ genomic DNA library was subcloned in the pBluescript-SK(-) vector and used for subsequent manipulation. To disrupt transcription of TA-p63 isoforms, a ~2.4 kb Spe I-Spe I fragment, containing exons 2 and 3 and adjacent intronic sequences, was replaced with the neomycin resistant gene (Neo^r) driven by the mouse phosphoglycerol kinase (PGK1) promoter and linked to the PGK1 poly (A) sequences. Insertion of the neomycin resistant gene allows for positive selection of cells that have been transfected with the construct and will eliminate most non-transfected cells. To select against random non-homologous recombination events, the HSV thymidine kinase (HSV-TK) gene under the control of the MC1 promoter was inserted at the 5' end of the targeting construct.
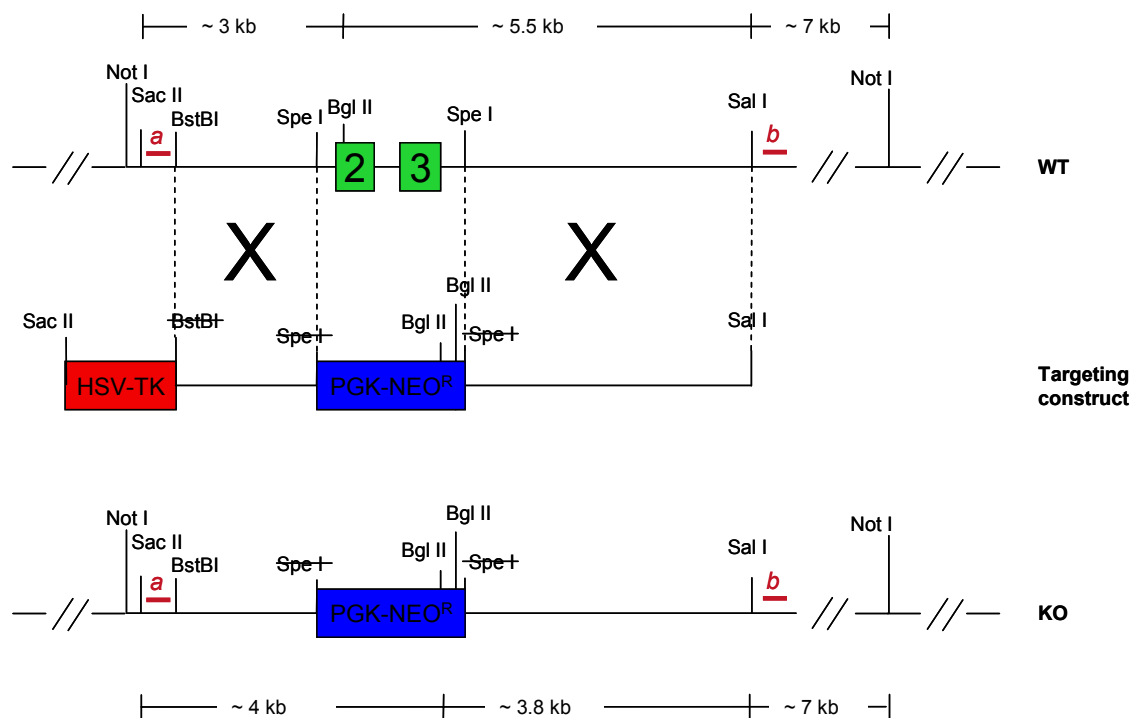
Figure 8   **Schematic of strategy for homologous recombination of TA-p63.** Genomic organization of TA-p63 gene before (WT) and after (KO) disruption by homologous recombination using the shown target construct. Exons 2 and 3 are replaced by neomycin resistance gene (PGK-NEO^R). Restriction sites, approximate size of DNA fragments, and positions of Southern blot probes (*a* and *b*) are indicated.

If the TK gene is randomly inserted into the genome and expressed in the presence of modified nucleosides or nucleoside analogues like gancyclovir or 1-[2-deoxy,2-fluoro-8-D-arabinofuranosyl]-5-iodouracil (FIAU), these compounds will be phosphorylated and act as competitive inhibitors of DNA polymerase or DNA chain terminators leading to cell death.

In addition to these positive and negative selection markers, the final construct contained 1.6kb and 3.7kb of flanking genomic sequences to the region to be deleted to allow for homologous recombination between the wild type allele and the targeting vector (Fig. 8).

3.3 Generation of TA-p63 (+/-) ES cells

The targeting construct was linearized by SacII restriction digest and electroporated into J1 ES cells. Electroporated ES cells were plated on a feeder layer of G418-resistant mitotically inactivated mouse embryonic fibroblasts. Positive selection with $300\mu g/ml$ G418 was started 24 hours after transfection and after another 24 hours $0.2\mu M$ FIAU was added in addition for negative selection. One week after electroporation, G418 and FIAU-resistant ES cell clones were picked, expanded and screened by Southern blot analysis for homologous recombination (Fig. 9). Out of a total of 475 screened clones, only two clones showed correct recombination at the TA-p63 locus (clones 224 and 378).
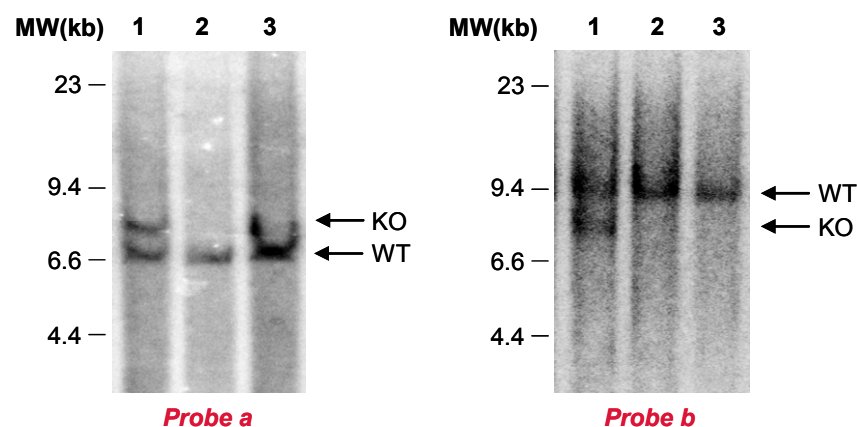
Figure 9 **Southern blot analysis of ES cell clones.** Genomic DNA was digested with BglII and hybridized with probes a and b depicted in Figure 7. Arrows indicate KO and WT alleles for both probes, and confirm successful homologous recombination of the TA-p63 locus. *Probe a* and *b*, lane 1 = heterozygous, lane 2,3 = wild type.

For Southern blot analysis genomic DNA was isolated from expanded clones and digested with restriction enzyme Bgl II. Hybridization of probe *a* to DNA fragments yields an approximately 6.2 kb and 7.5 kb for the wild type and targeted alleles, respectively. To confirm homologous recombination of the targeting construct, positive clones were further analyzed by Southern blot analysis with probe *b*, which hybridizes to DNA fragments of approximately 8.2 kb and 6.5 kb for the wild type and targeted alleles, respectively.

3.4   From ES cells to mice: Chimeras and TA-p63 deficient mice

Both independent ES cell lines were microinjected into blastocysts isolated from Balb/c mice and implanted into pseudo-pregnant foster mothers (performed by the Transgenic Core Facility of the Brigham and Women Hospital, Boston) to obtain chimeric mice. The degree of chimerism of the newborn mice was between 70-90% as judged by coat color. The chimeras were mated with wild type Balb/c mice to test if the injected ES cells contributed to the germline transmission of the TA-p63 mutant allele. Germline transmission was achieved with several animals and heterozygous TA-p63 mice were backcrossed into a Balb/c background and intercrossed to obtain TA-p63(-/-) animals. The genotype of mice was determined by PCR on genomic DNA from tail biopsies (Fig. 10).
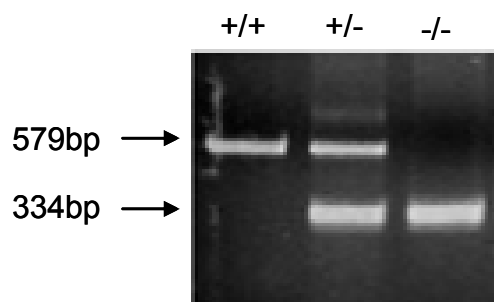
Figure 10 **PCR analysis of mouse genomic DNA.** Genomic DNA was isolated from mice tails and analyzed by PCR. Representative results for wild type (+/+), heterozygous (+/-), and knock out (-/-) alleles are shown.

3.5   Characterization of p63 expression in TA-p63(-/-) mice

Loss of TA-p63 expression at the protein level was confirmed by Western blot analysis of the thyroid gland from wild type and TA-p63(-/-) littermates. Using a TA-p63 specific mouse monoclonal antibody (4B2), no TA-p63 expression was detected in the thyroid gland of TA-p63(-/-) mice, while in the thyroid gland of wild type mice a strong signal was found. To investigate if the deletion of TA-p63 influenced ΔN-p63 expression, epidermal lysates from wild type and TA-p63(-/-) mice were analyzed with a pan-p63-antibody. By Western blotting, a slight decrease of ΔN-p63 expression in TA-p63(-/-) mice compared to wild type and heterozygous littermates was found (Fig. 11).
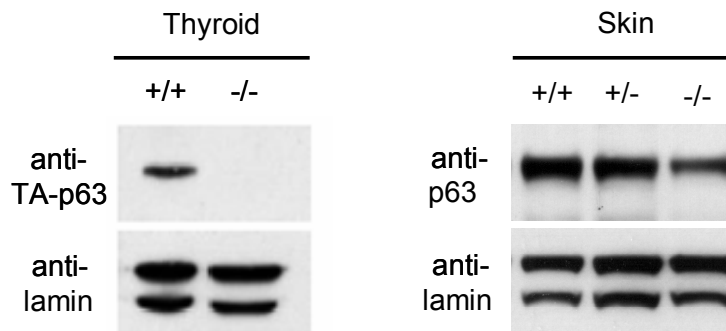
Figure 11 **Western blot analysis of TA- and ΔN-p63 expression in wild type and TA-p63 deficient mice.** Thyroid gland and skin were isolated from wild type and TA-p63(-/-) mice and analyzed for TA- and ΔN-p63 expression.

In addition to the thyroid gland, TA-p63 is highly expressed during early stages of oocyte development (primordial, primary, and early pre-antral stages), while it is undetectable at later stages (pre-antral and antral). Immunohistochemical detection of p63 in ovaries of wild type mice showed strong nuclear staining of early oocytes with TA-p63 specific antibodies as well as antibodies against all p63 isoforms. When ovaries of TA-p63(-/-) mice were stained with TA-p63 specific antibody no signal was detected. However, a pan-p63 antibody still stained the nucleus of primordial and primary oocytes, suggesting that in addition to TA-p63, ΔN-p63 is also expressed in oocytes (Fig. 12). Because pan-p63 antibody was shown to have cross-reactivity with a protein expressed in testis (M. Senoo, personal communication), the possibility existed that this protein is also expressed in oocytes. Investigation of pan-p63

staining in mice deficient for all p63 isoforms, however, revealed no detectable staining (E. Suh, personal communication).

Taken together, these results confirm that exon 2 and 3 of the p63 gene were successfully targeted for deletion from the mouse genome, and that the resulting TA-p63(-/-) mice still showed expression of ∆N-p63.
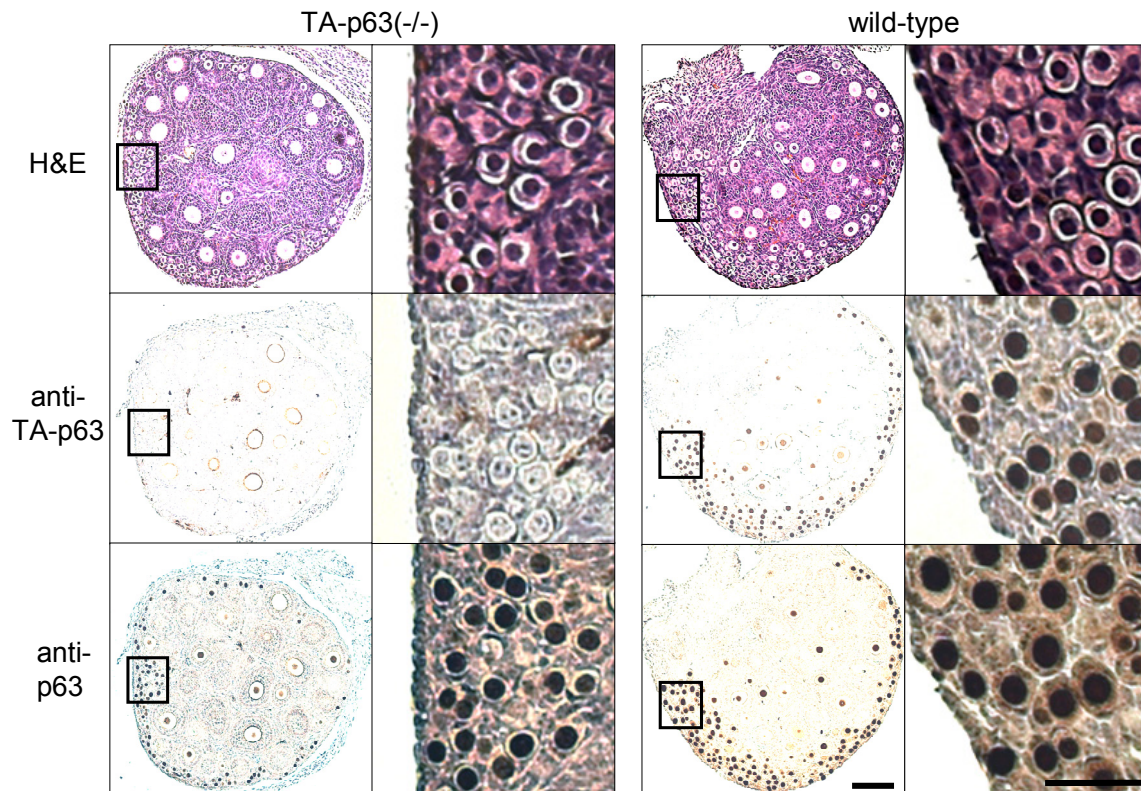
Figure 12 **Immuno-histochemistry of ovary sections of wild type and TA-p63(-/-) mice.**
Ovary sections were stained with antibodies against TA-p63 and all p63 isoforms. Scale bar is 150μm and 50μm, respectively.

3.6   TA-p63(-/-) mice are born at a non-mendelian frequency

In contrast to mice lacking both TA-p63 and ∆N-p63 (p63(-/-)) [9, 10], TA-p63(-/-) mice show normal limb and craniofacial development (Fig. 13). Unlike p63(-/-) mice, TA-p63(-/-) mice have normal fur and no obvious defects in epidermal development compared to wild type littermates (Fig. 14). About two thirds of all born TA-p63(-/-) embryos do not display gross phenotypical abnormalities. However, the total number of born TA-p63(-/-) mice was lower

than the expected mendelian frequency (7% of all mice in heterozygous-heterozygous and 18% in heterozygous-homozygous crosses, Table 1). On average in heterozygous-heterozygous crosses 1.86 TA-p63(+/+), 3.9 TA-p63 (+/-), but only 0.42 TA-p63(-/-) mice were born. Homozygous-heterozygous crosses showed a similar reduction in the number of expected TA-p63(-/-) progeny with an average of 3.5 TA-p63(+/-) and 1 TA-p63 (-/-) animal per litter.

In first 12 hours after birth approximately one third of all newborn TA-p63(-/-) pups developed extreme bloating of the intestines followed by swelling of the abdomen. Ultimately, the intestines collapsed and were pressed against the backside of the abdominal cavity which was extremely inflated. When the animals reached this stage, they suffered from breathing problems and died within hours. Investigation of the intestinal tract of these animals did not reveal any histological abnormalities. In humans, a developmental disease, named Hirschsprung disease, displays a phenotype of swollen abdomen, constipation, gas, and loss of appetite. The disease is caused by the absence of enteric ganglion cells in the distal bowel. However, patho-histological analysis of the intestine showed the presence of the ganglia.
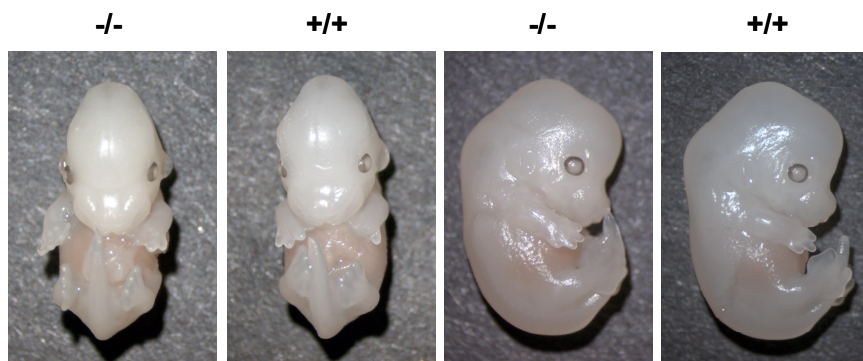
Figure 13 **Mice deficient for TA-p63.** Front and sagittal view of wild type and TA-p63 deficient embryos at day e16.5. Note wild type and TA-p63(-/-) mice are indistinguishable. TA-p63(-/-) display no craniofacial abnormalities and forelimbs and hindlimbs are normally developed.
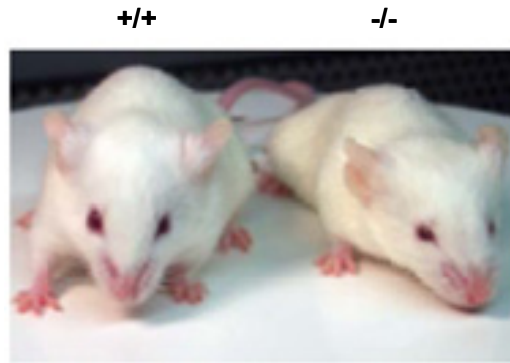
Figure 14 **Adult mice deficient for TA-p63.** Adult mice have a normal coat, nails and whiskers. Unlike mice deficient for all p63 isoforms, TA-p63 (-/-) mice display no abnormalities in epidermal development.

Other TA-p63(-/-) mice often displayed growth retardation starting a few days after birth that was probably due to insufficient feeding. While wild type pups had bulging abdomens after nursing that appeared white (milk belly), TA-p63(-/-) pups often lacked this sign of well nourishment. Pathological analysis of the oral cavity and the intestinal tract did not reveal any abnormalities. However, no detailed analysis of the esophagus has yet been conducted leaving swallowing problems as a possible explanation for the undernourishment. Because the TA-p63(-/-) pups were not found separated from their littermates in the cage, it is unlikely that they were recognized and singled out by the mother. In general, TA-p63(-/-) pups survived this stage and grew normally. At the time of weaning, TA-p63(-/-) mice had reached the same size and approximately the same body weight as wild type littermates.

The cause for the reduced frequency of TA-p63(-/-) at birth is still unknown. Limited investigation of litters at day e13.5 and e16.5 did not reveal any abnormalities, but the limited number of animals investigated did not allow any definitive conclusions. It is possible that the animals die *in utero* because of defects in early embryonic development. Furthermore, while male TA-p63(-/-) mice in the Balb/c background were fertile, female TA-p63(-/-) in the Balb/c background never showed signs of pregnancy or carried a pregnancy to term. Histological analysis of ovaries of adult mice revealed that maturation of follicles form primordial follicle to corpus luteum occurred normally.

Mating	TA-p63(+/+)	TA-p63(+/-)	TA-p63(-/-)
female (+/-) x male (+/-) (n=299)	30% [25%]	63% [50%]	7% [25%]
female (+/-) x male (-/-) (n=39)	0% [0%]	82% [50%]	18% [50%]
female (-/-) x male (+/-) (n=0)	0% [0%]	0% [50%]	0% [50%]

Table 1 **Mendelian frequency of hetero- and homozygous TA-p63-deficient mice matings.** Homozygous TA-p63(-/-) are born at a reduced mendelian frequency. Brackets indicate expected percentage.

3.7   TA-p63(-/-) mice display normal epidermal development

In contrast to p63(-/-) mice, TA-p63(-/-) mice undergo normal epidermal development and stratification and have a fur indistinguishable from wild type littermates. To analyze and compare the development of skin and its appendages in wild type and TA-p63(-/-) mice, embryos were isolated, and fixed at embryonic day e13.5, e16.5, as well as newborns. Furthermore, skin from adult mice was isolated and analyzed. Animals were embedded, sectioned, and stained with haematoxylin and eosin by the Rodent Histopathology Core facility. Whole embryo sections of wild type and TA-p63(-/-) were further compared with p63(-/-) at day e16.5.

Around embryonic day e13.5 stratification of the mouse epidermis begins, and cells from the basal layer differentiate and move upwards to form suprabasal layers. Early in development the single layered epithelium only expresses keratin 8 and 18. However, upon commitment to the epidermal cell fate, the early differentiation markers keratin 5 and 14 are induced. As stratification continues and the epidermis acquires additional layers (spinous and granular layer, stratum corneum) late markers of terminal differentiation such as loricrin, filaggrin, and involucrin are expressed.

Because the function of TA-p63 in commitment of the embryonic ectoderm to epidermal lineages and in initiation of epidermal stratification is very controversial, the skin of TA-p63(-/-) mice at different developmental stages was

wild-type   **TA-p63(-/-)**
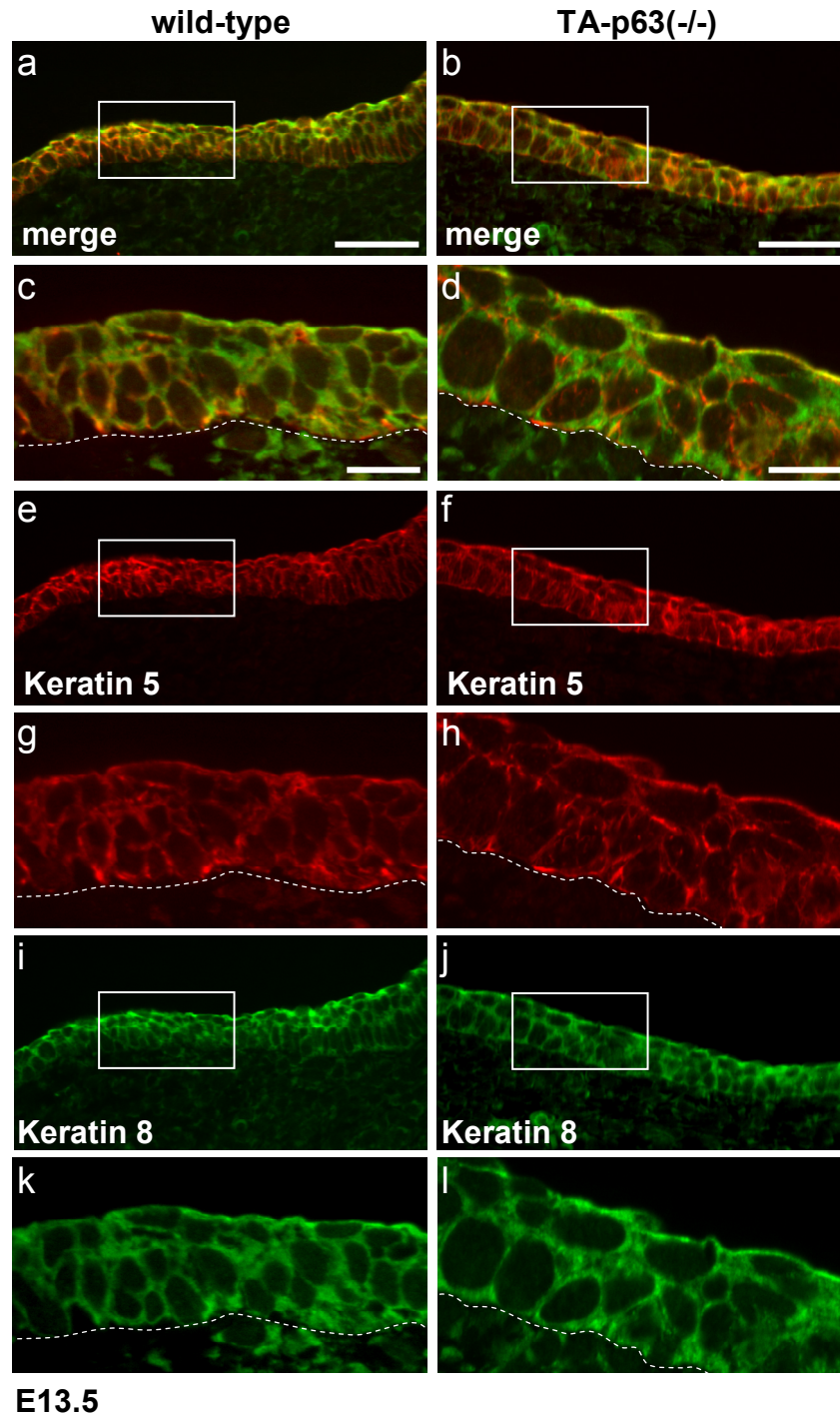
E13.5

Figure 15   **Keratin 5 and 8 expression in the epidermis of wild type and TAp63-deficient mice.** Immunofluorescence micrographs of keratin 5 (red) and keratin 8 (green) in wild type (left panel) and TA-p63(-/-) (right panel) epidermis on day e13.5. Magnification of area corresponding to insets in **a**, **b**, **e**, **f**, **i**, and **j** is shown underneath the respective micrograph (**c**, **d**, **g**, **h**, **k**, and **l**). Dotted lines indicate the border between the epidermis and the dermis. Images are single spinning disc confocal optical sections at 20X (**a**, **b**, **e**, **f**, **i**, and **j**) and 60X (**c**, **d**, **g**, **h**, **k**, and **l**) magnification. Scale bar is 50µm and 15µm, respectively.

E13.5

Figure 16 **ΔN-p63 and cytokeratin expression in the epidermis of wild type and TAp63-deficient mice.** Immunofluorescence micrographs of p63 (red) and cytokeratin (green) in wild type (left panel) and TA-p63(-/-) (right panel) epidermis on day e13.5. Magnification of area corresponding to insets in **a**, **b**, **e**, **f**, **i**, and **j** is shown underneath the respective micrograph (**c**, **d**, **g**, **h**, **k**, and **l**). Dotted lines indicate the border between the epidermis and the dermis. Images are single spinning disc confocal optical sections at 20X (**a**, **b**, **e**, **f**, **i**, and **j**) and 60X (**c**, **d**, **g**, **h**, **k**, and **l**) magnification. Scale bar is 50µm and 15µm, respectively.

investigated in more detail by immunostaining and compared to skin of wild type littermates to determine if the onset of stratification is delayed and if stratification on a molecular level occurs correctly.

Although the intact epidermis of newborn mice and the coat of adults suggest that commitment and differentiation occurs normally, it is still possible that loss of TA-p63 expression alters these processes at the molecular level.

Sections from wild type and TA-p63(-/-) mice at e13.5 were stained with antibodies against keratin 5, 8, and pan-cytokeratin to compare the timing of initiation of stratification as well as the structure of the interfollicular epidermis (Fig 15 and 16). Furthermore, sections were stained with a pan-p63 antibody to determine if ∆N-p63 is undisturbed in expression and localization after deletion of exon 2 and 3 of the p63 gene. Both TA-p63(-/-) and wild type mice show keratin 5 and 8 staining of the basal and spinous layer. P63 staining, as detected with a pan-p63 antibody, was present in wild type as well as TA-p63 (-/-) mice, confirming that ∆N-p63 expression in the epidermis was not affected by disruption of TA-p63 (Fig. 16). However, quantification of immunofluorescence intensity of pan-63 staining revealed a 22% decrease in TA-p63 (-/-) mice compared to wild type littermates. As expected, no TA-p63 staining was seen in the epidermis of TA-p63(-/-) mice. However, staining with the TA-p63 specific antibody also did not reveal expression of TA-p63 in the epidermis of wild type mice, suggesting that this isoform is not present on protein levels in this tissue.

The organization of the epidermis is also not altered in TA-p63(-/-) mice. As expected for e13.5 embryos the epidermis consists of a single layer of palisade-like arranged basal cells that are covered by a single or double layer of suprabasal cells whose nuclei are turned perpendicular in relation to basal layer cells. Pan-cytokeratin, keratin 5 and 8 stain consistently revealed this organization and showed that the thickness of the epidermis is comparable between wild type and TA-p63(-/-) mice at this stage.

Next, epidermal development was compared between wild type, TA-p63(-/-), and p63(-/-) mice. At day e16.5 the epidermis has further stratified into spinous and granular layers which express keratin 1, 10, loricrin and fillagrin. Sections of embryos isolated at this stage were stained with early and late differentiation markers as well as with an antibody against all-p63 isoforms.
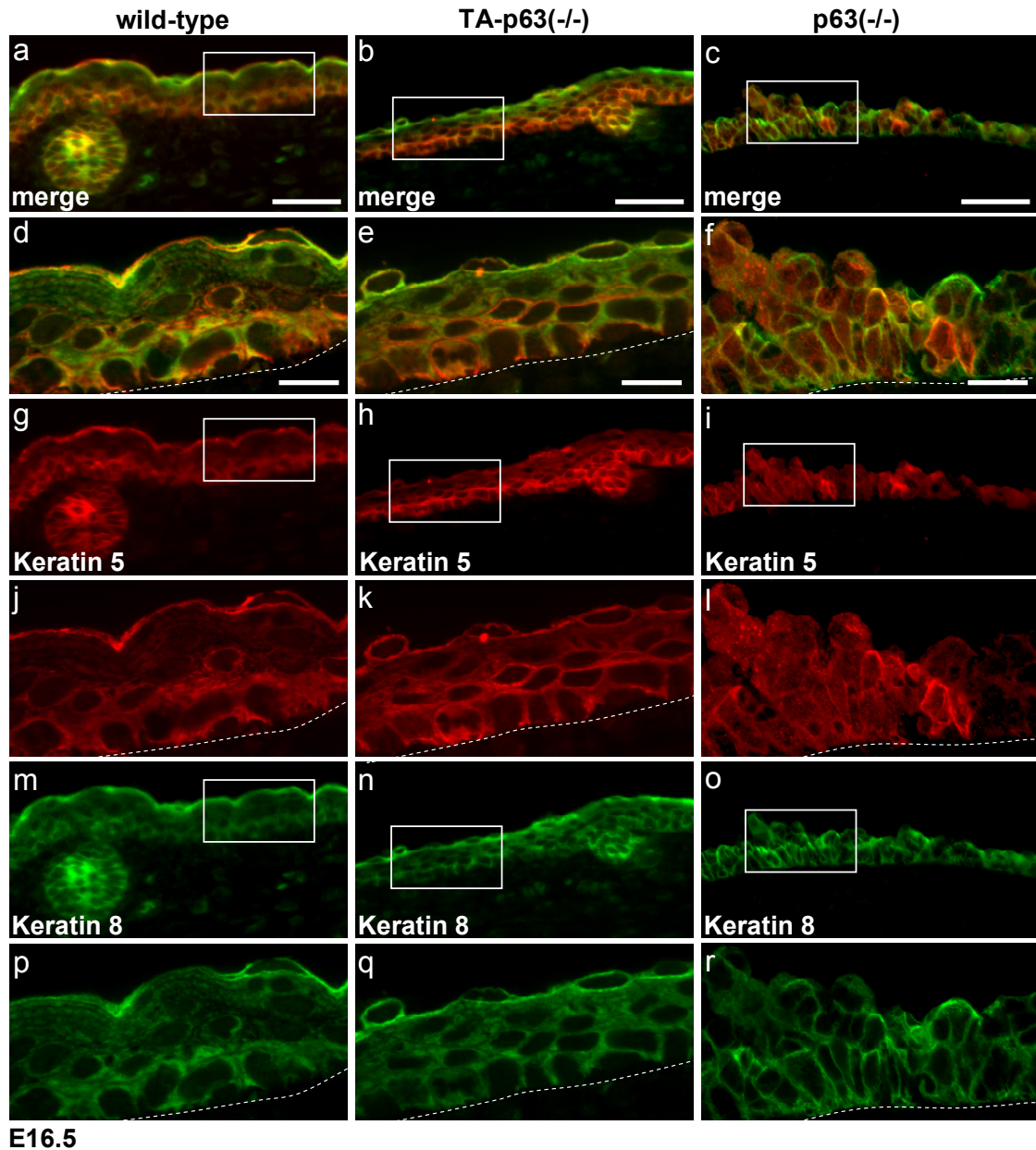
Figure 17 **Keratin 5 and 8 expression in the epidermis of wild type, TAp63-, and p63-deficient mice.** Immunofluorescence micrographs of keratin 5 (red) and keratin 8 (green) in wild type (left panel), TA-p63(-/-) (middle panel), and p63(-/-) epidermis on day e16.5. Magnification of area corresponding to insets in **a**, **b**, **c**, **g**, **h**, **i**, **m**, **n**, and **o** is shown underneath the respective micrograph (**d**, **e**, **f**, **j**, **k**, **l**, **p**, **q**, and **r**). Dotted lines indicate the border between the epidermis and the dermis. Images are single spinning disc confocal optical sections at 20X (**a**, **b**, **c**, **g**, **h**, **i**, **m**, **n**, and **o**) and 60X (**d**, **e**, **f**, **j**, **k**, **l**, **p**, **q**, and **r**) magnification. Scale bar is 50µm and 15µm, respectively.

E16.5

Figure 18 **p63 and loricirn expression in the epidermis of wild type, TAp63-, and p63-deficient mice.** Immunofluorescence micrographs of p63 (red) and loricrin (green) in wild type (left panel), TA-p63(-/-) (middle panel), and p63(-/-) epidermis on day e16.5. Magnification of area corresponding to insets in **a**, **b**, **c**, **g**, **h**, **i**, **m**, **n**, and **o** is shown underneath the respective micrograph (**d**, **e**, **f**, **j**, **k**, **l**, **p**, **q**, and **r**). Dotted lines indicate the border between the epidermis and the dermis. Images are single spinning disc confocal optical sections at 20X (**a**, **b**, **c**, **g**, **h**, **i**, **m**, **n**, and **o**) and 60X (**d**, **e**, **f**, **j**, **k**, **l**, **p**, **q**, and **r**) magnification. Scale bar is 50µm and 15µm, respectively.

wild-type **TA-p63(-/-)** **p63(-/-)**

a merge   b merge   c merge

d   e   f

g p63   h p63   i p63

j   k   l

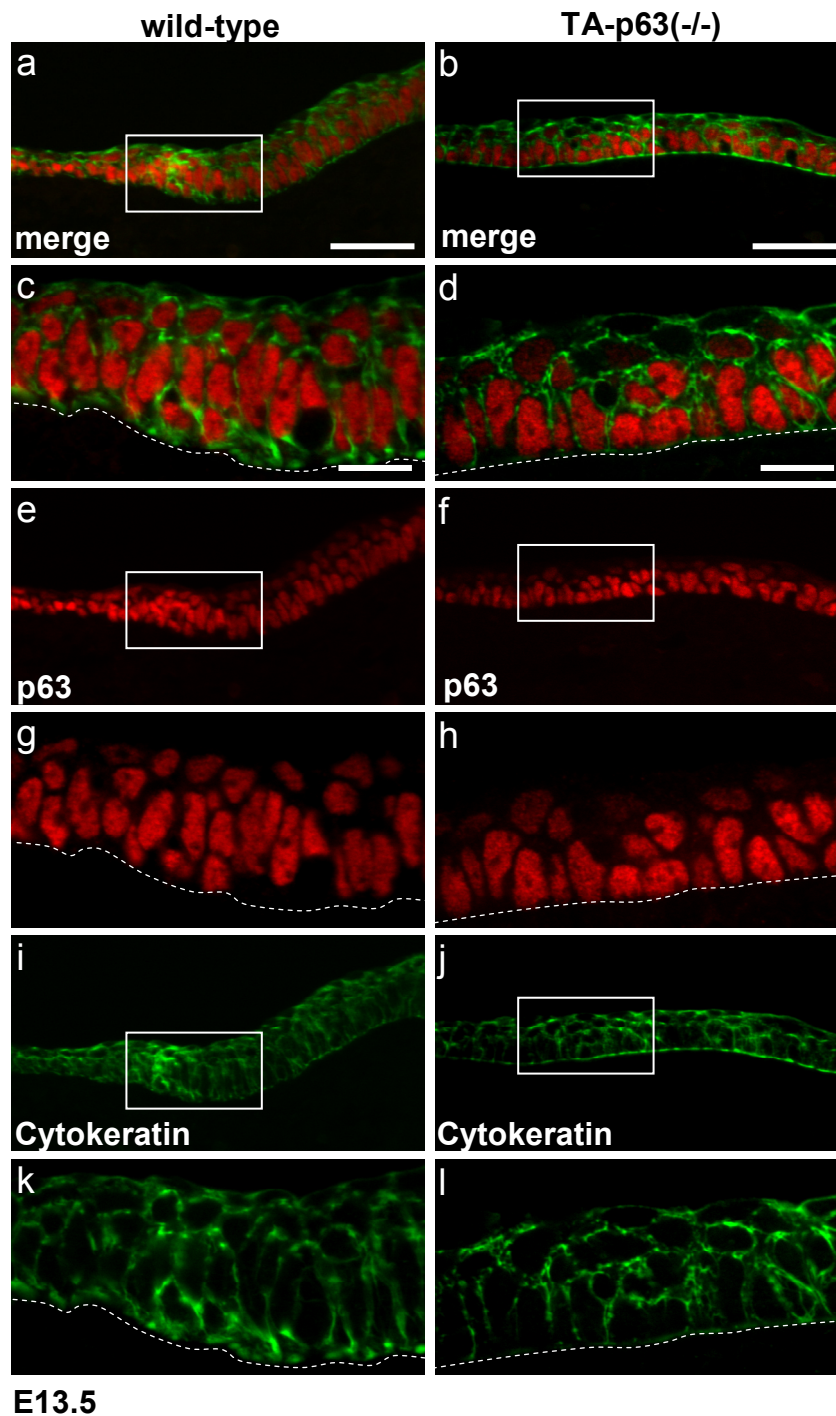m Cytokeratin   n Cytokeratin   o Cytokeratin

p   q   r

E16.5

Figure 19 **p63 and cytokeratin expression in the epidermis of wild type, TAp63-, and p63-deficient mice.** Immunofluorescence micrographs of p63 (red) and loricrin (green) in wild type (left panel), TA-p63(-/-) (middle panel), and p63(-/-) epidermis on day e16.5. Magnification of area corresponding to insets in **a**, **b**, **c**, **g**, **h**, **i**, **m**, **n**, and **o** is shown underneath the respective micrograph (**d**, **e**, **f**, **j**, **k**, **l**, **p**, **q**, and **r**). Dotted lines indicate the border between the epidermis and the dermis. Images are single spinning disc confocal optical sections at 20X (**a**, **b**, **c**, **g**, **h**, **i**, **m**, **n**, and **o**) and 60X (**d**, **e**, **f**, **j**, **k**, **l**, **p**, **q**, and **r**) magnification. Scale bar is 50μm and 15μm, respectively.

Pan-cytokeratin, keratin 5, and keratin 8 were detectable in wild type, TA-p63(-/-), and p63(-/-) mice (Fig. 17). Furthermore, in mice of all three genotypes, the late differentiation marker loricrin was seen (Fig. 18). While a pan-p63 antibody strongly stained the nucleus of cells in the basal and suprabasal layer of the epidermis of wild type and TA-p63(-/-) mice, p63 expression was completely absent in the original p63(-/-) and extensive exposure only revealed background staining (Fig. 18 and 19). Consistent with the observation at day e.13.5, quantification of immunofluorescence intensity of pan-p63 staining revealed a 20% decrease in TA-p63 (-/-) epidermis compared to that of wild type littermates. With ongoing stratification, the cells in the upper layers of the skin flatten, while basal layer cells keep their palisade-like arrangement.

In both wild type and TA-p63(-/-) epidermis, this layered structure is intact; however, no such organization is obvious in the epidermis of p63(-/-) mice. Consistent with previously published data of the McKeon laboratory, the sections of p63(-/-) mice showed patches of skin that were multi-layered and stratified. However, large areas of the surface of p63(-/-) embryos were covered with a single-layered epithelium, which expressed keratin 5 and 8, and in some areas with patches, which showed loricrin staining.

Immunohistochemical analysis of skin sections of newborn and adult wild type and TA-p63(-/-) mice with antibodies against keratin 5, keratin 10, cytokeratin, and loricrin did not reveal differences (data not shown). As revealed by H&E staining, epidermal appendages like hair follicles, vibrissae, mammary, sebaceous, lacrymal and salivary glands as well as teeth primordia developed normally in the TA-p63(-/-) (Fig. 20).

Taken together, the absence of defects in development and stratification of the epidermis and its appendages indicates that TA-p63 is not required for these processes. The p63 staining in wild type and TA-p63(-/-) skin with the pan-p63 antibody confirms that ΔN-p63 is the predominant isoform and mediates p63 functions in epithelial morphogenesis that were uncovered in the original p63 knockout mouse, independent of TA-p63 [9, 10].
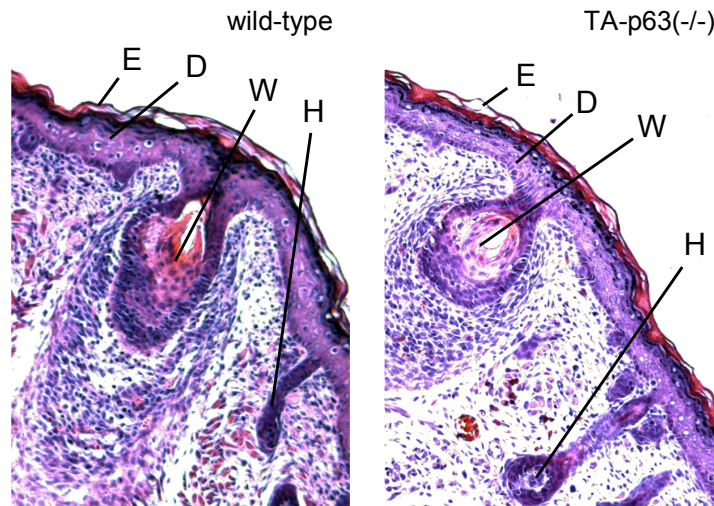
Figure 20 **H&E stain of the epidermis of wild type and TAp63-deficient mice.** Micrographs of H&E stained sections of wild type and TA-p63-deficient mice at day one after birth. E-epidermis, D- dermis, W- whisker follicle, H- hair follicle.

4. Discussion

The function of the p63 gene in epithelial, craniofacial, and limb development in mice was revealed by mice deficient for all p63 isoforms [9, 10]. Now, seven years after the initial description of the p63(-/-) mice, the interpretation of their phenotype and the function of p63 in epidermal development is still controversial. The situation is further complicated by the different opinions on the specific function of p63 isoforms, ΔN- and TA-p63, in these processes. The experiments described in the previous section were conducted to directly test the involvement of TA-p63 in epidermal development and elucidate its specific function in mice.

4.1   Mice deficient for TA-p63

TA-p63(-/-) mice were generated by homologous recombination in mouse ES cells (Fig. 8) and successful abrogation of TA-p63 protein expression was confirmed by Western blotting (Fig. 11) and immuno-histochemistry (Fig. 12).

In the absence of TA-p63, pan-p63 staining of ovaries of TA-p63(-/-) mice revealed expression of ΔN-p63 (Fig. 12). Because in previous analysis expression of ΔN-p63 in ovaries was undetectable by Western blotting (E. Suh, personal communication), it is therefore possible that upon disruption of TA-p63 expression, ΔN-p63 is up-regulated in oocytes. Further investigations are necessary to better understand this phenomenon. Moreover, analysis of p63 expression in skin of TA-p63(-/-) mice using the pan-p63 antibody showed that, in this tissue, the expression level of ΔN-p63 is reduced (Fig. 11, 16, 18, and 19).

The modulation of ΔN-p63 expression in the epidermis and likely in oocytes could be due to interference of the inserted neomycin resistance gene with ΔN-p63 transcription. However, the neomycin resistance gene was inserted 38kb upstream of the transcriptional start of ΔN-p63 and the effect on ΔN-p63 expression in skin is relatively minor (approximately 20%). Therefore, it is more likely that the reduction of ΔN-p63 protein in the epidermis and possibly the increase in oocytes is due to cross-regulation between TA- and ΔN-p63. Recently, a report showed that TA-p63 binds to a p53-binding site in the promoter of ΔN-p63 and is capable of activating its transcription [62]. The two-

genes-in-one structure of the p63 gene results in the translation of two different kinds of protein variants with the same DNA-binding domain. Because the different variants are expressed at different levels in distinct tissues [14] (Suh et al, submitted), changes of their abundance due to loss of cross-regulation in TA-p63(-/-) mice, could have implications for the respective functions in target gene regulation, development and post-natal processes.

Other explanations for the observed modulation of ∆N-p63 are that loss of TA-p63 expression has a more global effect on gene expression in a specific tissue and thereby indirectly affects ∆N-p63 expression. Furthermore, it has not been investigated whether the loss of TA-p63 in the thyroid gland leads to increase or decrease of thyroid hormone levels, possibly resulting in more systemic defects that could influence protein expression.

Because p63(-/-) mice die within hours of birth, an investigation of a function in tumor suppression by itself and in combination with p53 was limited. In a p53-null background, heterozygosity for all p63 isoforms showed an alteration of the tumor spectrum observed in p53-null only mice. Because two thirds of TA-p63(-/-) mice survive and develop normally, these analyses are possible and crosses to achieve TA-p63(-/-);p53(-/-) mice are underway.

4.2   Normal skin development in TA-p63(-/-) mice

One of the main incentives for making a TA-p63(-/-) mouse was to definitively answer the question about the relative significance and contribution of the two different classes of p63 isoforms, TA- and ∆N-p63, to the phenotypes observed in p63-deficient mice, especially in epidermal differentiation and stratification.

In contrast to p63(-/-) mice, TA-p63(-/-) mice display no defect in epidermal development, expression of early and late differentiation markers, or skin morphology (Fig. 14-19).

These observations suggest that lack of epidermal expansion and stratification seen in mice lacking all p63-isoforms is not attributable to TA-p63. Instead, these epithelial defects are likely due to absence of ∆N-p63. Previous studies [10] (Pinto et al., submitted), as well as analysis presented in this work

(Fig. 16-18), indicate a role of ΔN-p63 in the maintenance of the proliferative potential and self-renewal capacity of epithelial progenitor cells. Although the epidermis of p63(-/-) is only capable of limited expansion, it does undergo differentiation and stratification as shown by the expression of differentiation markers (Fig. 16-18). The limited expansion of the epidermis followed by its disintegration in p63(-/-) mice can be explained with the loss of proliferative potential and self-renewal capacity of the epidermal stem cells. While in the wild type situation, epidermal stem cells are capable of undergoing nearly unlimited rounds of cell division (human skin is completely renewed in 21 days), epidermal stem cells in p63(-/-) mice lack this ability leading to terminal differentiation after a limited number of cell divisions. This notion is further supported by the observation that depletion of p63 by shRNA in immature keratinocytes reduced their proliferative potential (Pinto et al, submitted) and that conditional ablation of p63 in adult mice leads to cellular senescence and aging [47].

Moreover, the normal epidermal development of TA-p63(-/-) mice demonstrates that TA-p63 is not, as suggested [12], involved in commitment of the embryonic ectoderm to an epidermal lineage, or at least not essential in this process. The lack of detectable TA-p63 protein expression in the epidermis, at any developmental stage, further obviates a fundamental role of TA-p63 in skin morphogenesis. Moreover, the development of a normal coat and skin morphology in adult mice demonstrates that stratification and terminal differentiation occur normally in the absence of TA-p63 after embryogenesis. If ΔN-p63 function would be to offset TA-p63 to enable stratification and terminal differentiation [12, 49], one would expect that in the absence of TA-p63, stratification and terminal differentiation would occur prematurely.

Although the epidermis of TA-p63(-/-) appears normal, it is possible that that under stress conditions, such as injury, the lack of TA-p63 and/or the reduction in ΔN-p63 expression could influence wound healing capability of the epidermis [63]. Because the analysis of TA-p63(-/-) mice has only recently begun and the number of animals is limited, the long-term effects of disruption of TA-p63 are not yet understood.

4.3   Non-mendelian frequency, newborn death, and lack of pregnancies of TA-p63(-/-) mice

Despite the lack of defects in epidermal development, the total number of newborn mice in heterozygous-heterozygous and heterozygous-homozygous crosses is reduced. While matings of wild type mice result on average in a litter size of eight animals, the litter size of heterozygous-heterozygous and heterozygous-homozygous crosses is reduced to an average of six and four pups, respectively. Furthermore, the number of TA-p63(-/-) pups in these matings is less than expected for a gene inherited by mendelian laws.

The general reduction in litter size in both types of crosses and the specific absence of TA-p63(-/-) homozygous mutants, suggests that embryos are lost during pregnancy and that these embryos are likely homozygous for the disrupted TA-p63 allele. The loss of TA-p63(-/-) mice could be the result of defects during early mouse development that do not show 100% penetrance and is still under investigation.

Moreover, one third of all TA-p63(-/-) homozygous mutants that are born subsequently die because of severe bloating of intestines and the abdomen. Other TA-p63(-/-) homozygous mutant often display growth retardation in the first weeks after birth. It is possible that both undernourishment as well as bloating are the result of different degrees of infections of the newborn after birth. While patho-histological analysis ruled out Hirschsprung disease as cause for the observed defects, another possibility is that the defects are due to necrotizing enterocolitis. In humans, necrotizing enterocolitis is observed in premature newborns and results from a weakening of the intestinal tissue by too little blood and oxygen flow. Upon feeding, bacteria that populate the intestinal tract damage this tissue. If the tissues become necrotic, bacteria can migrate into the abdomen and cause severe and deadly infections. To further investigate the possibility of necrotizing enterocolitis followed by bacterial invasion of the abdome in newborn TA-p63(-/-) mice, pregnant females will be treated with antibiotics during pregnancy. In case the suspicion can be confirmed, it is expected that more newborn TA-p63(-/-) survive after birth.

The observed lack of pregnancy in TA-p63(-/-) mice (Table 1) is probably not due to defects before ovulation, because follicle development occurs normally in TA-p63(-/-) ovaries. P63 protein is expressed in the basal layer of the

cervical and vaginal epithelium, but only in individual cells and cell groups in the uterus [64]. Detailed pathological analysis of the urogenital tract of p63(-/-) showed that the uterus developed normally, while cervical and vaginal epithelium displayed a transfiguration from squamous to cuboidal cells [10]. Although a defect in implantation cannot be excluded, the integrity of the uterus in both p63(-/-) and TA-p63(-/-) mice suggest that implantation should occur correctly.

A more intriguing explanation for the observed lack of pregnancy in TA-p63(-/-) mice, is the recent discovery of TA-p63 implication in the protection of the female germline (Suh et al., submitted). Primordial and primary oocytes undergo TA-p63-dependent cell death upon failure to repair DNA double-stranded breaks (DSB) induced by γ-irradiation or chemotherapeutics treatment. Even without external stimuli, DNA DSB occur during recombination of homologous chromosomes in meiosis I and must be repaired. Errors in this process are thought to be the cause for the high rate of oocyte death just before birth [30]. If TA-p63 also plays a role in this type of oocyte death, it is reasonable to speculate that in TA-p63(-/-) mice oocytes may survive abortive homologous recombination. Zygotes emerging from these oocytes are likely to have mutations from unrepaired DSB, and thus be miscarried.

In addition, more detailed analysis of the consequence of loss of protection of the female germline can now be conducted and the possible function of ΔN-p63 in oocytes revealed. Finally, the possible consequence of TA-p63 disruption of the thyroid gland, its metabolism, and the overall hormonal balance will be investigated.

The results presented in this work not only vitiate a function of TA-p63 in epidermal commitment during embryogenesis, and conclusively demonstrate the significance of ΔN-p63 in epidermal development and regeneration, it also revealed more about the function of TA-p63 in oocyte death and protection of the female germline.

PART II – Checkpoint Signaling

5. Summary

A high fidelity of chromosome segregation is crucial to ensure correct transmission of genetic material to daughter cells. Errors in this process result in aberrant chromosome numbers and can cause severe developmental defects, miscarriages, and cancer. The spindle assembly checkpoint is a surveillance mechanism that monitors chromosome segregation, detects attachment defects, and delays anaphase onset until errors are corrected. Moreover, passive mechanisms such as kinetochore geometry, architecture, and back-to-back orientation of sister kinetochores further reduce the risk of mis-attachment. Upon satisfaction of the spindle assembly checkpoint, inactivation of Cdk1/cyclin B and cleavage of cohesin leads to chromosome separation and cell cycle progression into anaphase.

Since the identification of the first molecular components of the spindle assembly checkpoint over 15 years ago [3-5], many proteins were found to be involved in checkpoint signaling. A highly complex protein interaction network is emerging that connects sister chromatid cohesion, kinetochore biology, and microtubule cytoskeleton with the spindle assembly checkpoint. The conserved family of shugoshin proteins are one of the latest additions to this network and present a link between sister chromatid cohesion, checkpoint signaling, and microtubule dynamics. While initial investigations in yeast and *drosophilia* have been conducted, little is known about shugoshin functions in mammalian cells.

The work presented here provides a detailed characterization of one of the key players in checkpoint signaling, BubR1, including its post-translation modifications and its interactions during the cell cycle. Furthermore, the work provides insight into the regulation and evolution of BubR1's localization and function. Finally, the interaction of BubR1 and Sgo2 is shown to link checkpoint signaling and kinetochore geometry.

6. Introduction

6.1   Chromosome segregation

Mitosis is an essential step of the cell cycle. When cells divide and segregate their genomes to daughter cells, it has to be ensured that each daughter cell receives an identical set of chromosomes. Chromosome mis-segregation during development leads to birth defects and in most cases to spontaneous abortions. Certain mis-segregations of sex chromosomes and trisomies of chromosomes 13, 18, and 21 are viable, but display severe developmental and fertility defects. In somatic cells, aneuploidy is often found in solid tumors and cancer cell lines [65].

How cells segregate their chromosomes is a research interest for more than 150 years. Pioneering work in this field has been done by Walter Flemming and Theodor Boveri in the late nineteenth century when they first described the separation of chromosomes during animal mitosis (Fig.21) [66-69].
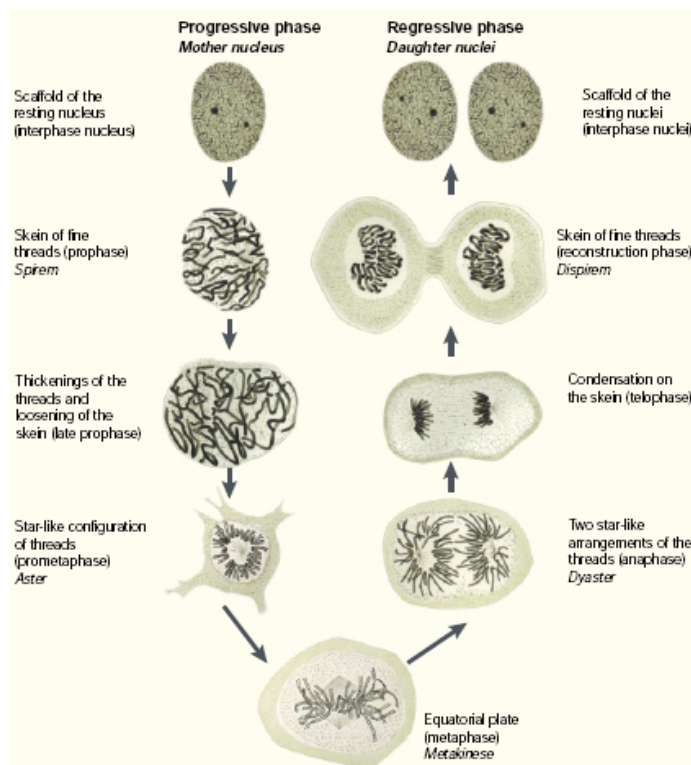
Figure 21   **Phases of mitosis.** Mitosis as observed by Walther Flemming in 1882. Mitosis begins with the condensation of chromosomes into skein-like threads (prophase), which thicken and form a star-like configuration of an aster (prometaphase). Chromosomes align at the equatorial plate (metaphase) followed by formation of a dyaster which moved apart and decondense into skein-like threads before the cell divides (telophase). Adapted from [69]

Boveri and van Hanseman found that cells from carcinomas showed abnormal mitotic figures and Boveri postulated that chromosomal mis-segregation might be the cause for cancer development [70, 71]. Although these initial findings date back more than a century, it is still unclear today if aneuploidy is cause or consequence of cell transformation, making chromosome segregation in meiosis and mitosis the focus of many research studies.

6.2   The different phases of mitosis

Mitosis is divided into five stages that are often followed by cytokinesis (Fig. 22). Cytokinesis is the physical division of the cytoplasm and even distribution of organelles, plasma membrane and other cellular components between the daughter cells [72, 73].
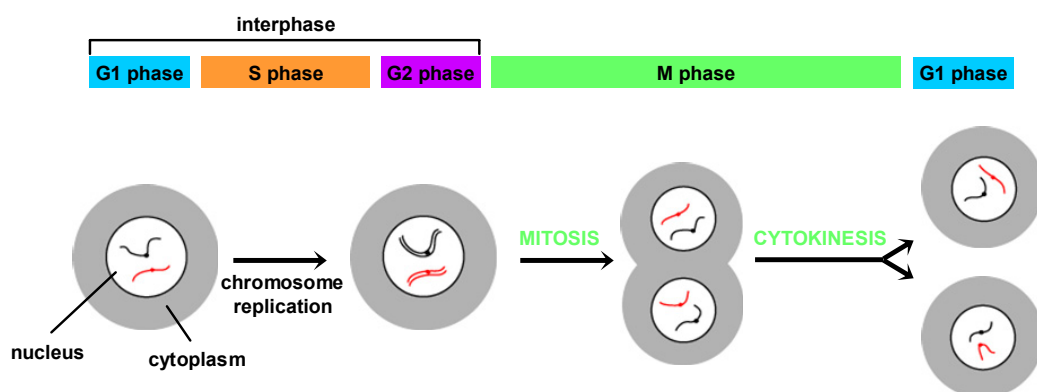
Figure 22   **Cell Cycle.** Interphase is divided in G1-, S-, and G2 phase. Chromosomes are replicated in S-phase and separated and segregated in mitosis. Mitosis is divided into five phases followed by cytokinesis. Adapted from [72]

At prophase, the first phase of mitosis, chromatin starts to condense and chromosomes become visible. Each chromosome consists of a pair of previously replicated sister chromatids that are bound together at the centromere. Outside the nucleus the duplicated centrosomes separate and begin to move to the position of the future spindle poles. Microtubules grow out from the centrosomes and form the mitotic spindle. Early in mitosis, proteins are recruited to the centromere to assemble the kinetochore, a proteinaceous structure that functions as microtubule attachment center. Most cells undergo a

so called open mitosis in which the nuclear envelope breaks down in the beginning of prometaphase. In this open configuration, microtubules start to search and capture kinetochores. When both sister kinetochores are attached to microtubules that emanate from opposite poles, chromosomes congress at the metaphase plate (metaphase). At the beginning of anaphase, sister chromatids separate at the centromere and move apart to the spindle poles. Late in anaphase the plasma membrane constricts, in the process of cytokinesis, and the spindle midzone becomes visible. In telophase, the chromatids reach the spindle poles and begin to decondense and the nuclear envelope reassembles around then. At the end of mitosis, the midzone develops into a cleavage furrow and cytokinesis occurs (Fig. 23) [72, 73].

Prophase

Prometaphase

Metaphase

Anaphase

Telophase
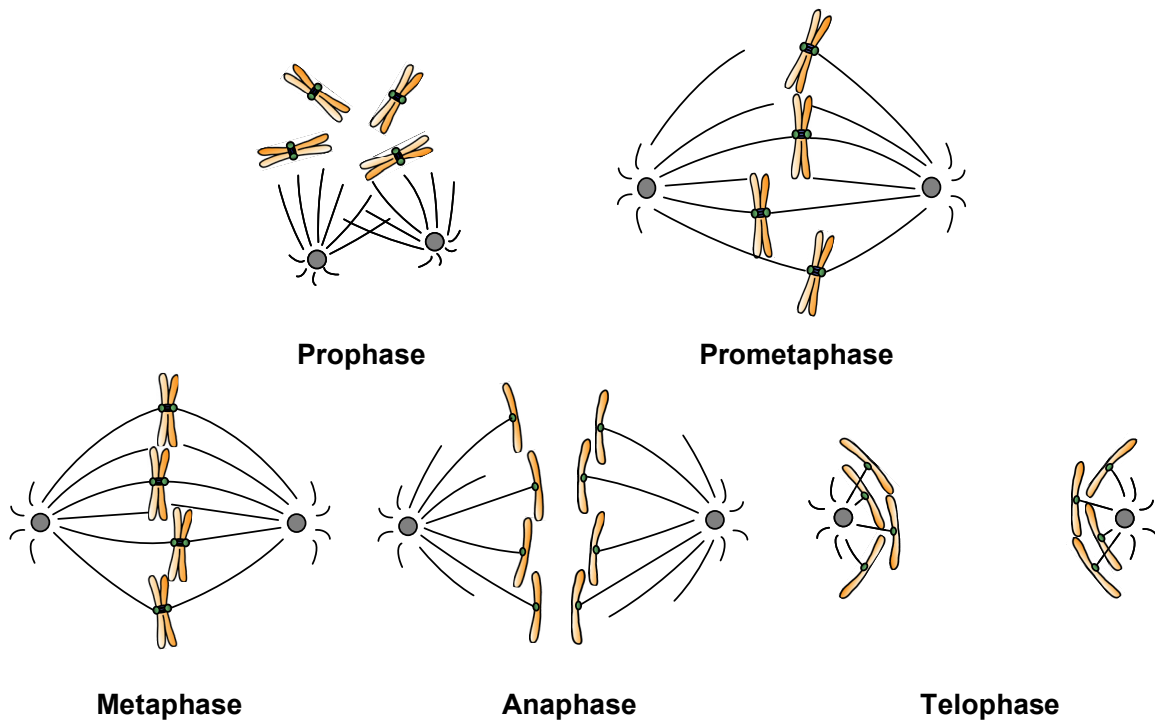
Figure 23 **Phases of mitosis.** Scheme of chromosome alignment and segregation during mitosis. In early prophase chromosomes start to condense. Duplicated centrosomes separate and start to emanate microtubules. In prometaphase the nuclear envelop breaks down and microtubules attach to kinetochores. A bipolar spindle is formed and chromosome align at is equator in metaphase. By early anaphase, sister chromatids have separated and move towards the poles, which they reach in telophase.

6.3 Mitotic progression

Progression from one cell cycle phase to the next is driven by cyclin/cyclin-dependent kinase (CDK) complexes [74]. Precise activation and inactivation of these complexes is essential to ensure accurate advance though the cell cycle. Entry into mitosis is controlled by the MPF (maturation or M-phase promoting factor), which consist of cyclin-dependent kinase CDK1 and cyclinB1 [75, 76]. The activity of cyclinB1/CDK1 is controlled by post-translational modifications and subcellular localization [77-79]. Inhibitory phosphorylation of cyclinB1/CDK1 by Wee1 and Myt1 keeps it in an inactive state until it is dephosphorylated by cdc25 phosphatase [80]. Furthermore, cyclinB1 is localized to the cytoplasm in interphase where it is kept in an inactive state [81]. Shortly before onset of mitosis, cyclinB1/CDK1 is phosphorylated within the cytoplasmic retention signal (CRS) and accumulates in the nucleus [82]. When cyclinB1/CDK1 is fully activated in the nucleus, cells enter prophase. In the early stages of mitosis high cyclinB1/CDK1 activity is necessary for phosphorylation of lamins to promote nuclear envelope breakdown, centrosome separation, spindle assembly, and chromosome condensation [74]. Furthermore, cyclinB1/CDK1 phosphorylation is essential for the regulation of the activity of the anaphase-promoting complex/cyclosome (APC/C). APC/C is an E3-ubiquitin ligase that controls the transition from metaphase to anaphase and mitotic exit. APC/C activity is regulated by phosphorylation and binding of an activator protein Cdc20 [83, 84]. Although several kinases are implicated in APC/C phosphorylation [85-88], cyclinB1/CDK1 seems to the major APC/C activator. In a feed-back loop, activated APC/C-Cdc20 ubiquitinates and thereby targets cyclinB1 for degradation leading to mitotic exit. Another target of APC/C is securin, a protein that binds and inhibits the cysteine protease separase. Degradation of securin activates separase which in turn cleaves cohesin between sister chromatids leading to sister chromatid separation [89, 90] (Fig. 24). To avoid precocious sister chromatid separation, APC/C activity is inhibited by binding of its activator Cdc20 to proteins of the spindle assembly complex. The spindle assembly complex is a surveillance mechanism that monitors microtubule-kinetochore attachment and chromosome congression [91, 92]. If both criteria are fulfilled, Cdc20 is released, activates APC/C and drives mitotic exit.
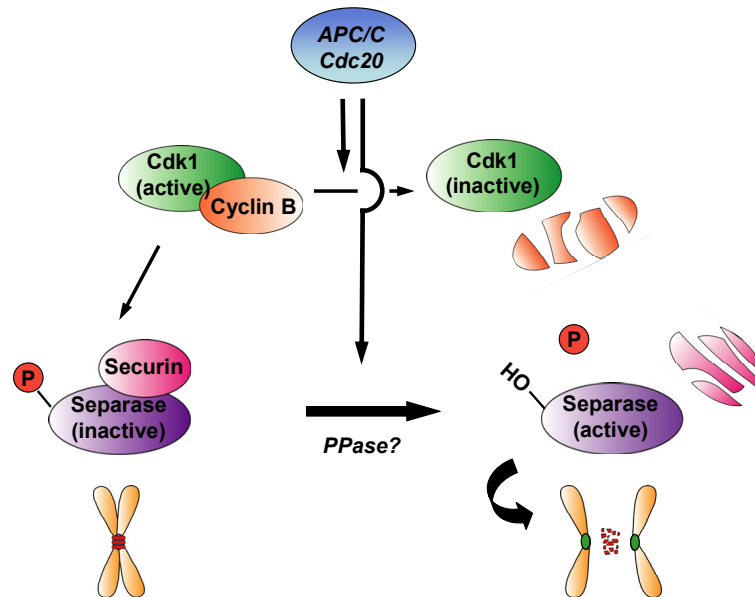
Figure 24 **Metaphase to anaphase transition.** Diagram depicting the metaphase to anaphase transition in mammalian cells. Separase is kept in an inactive state by phosphorylation by Cdk1/cyclin B and binding to securin. Upon ubiquitination and degradation of securin by APC/C-Cdc20 and the proteasome, respectively, as well as dephosphorylation, separase is activated and cleaves cohesin between sister chromatids. At the same time, APC/C-Cdc20 targets cyclin B for degradation leading to Cdk1 inactivation and exit from mitosis.

6.4   Meiosis

In meiosis a diploid germ cell undergoes two rounds of cell division which ultimately yielding four haploid daughter cells. After a single round of DNA replication, cells enter into meiosis I in which chromatin condenses (prophase I), homologous chromosomes align at the metaphase plate (metaphase I), and are separated (anaphase I) and segregated to two daughter cells (telophase I). During prophase I, non-sister chromatids of homologous chromosomes pair and undergo crossing-over leading to genetic recombination. Aside from recombination of the genetic material, crossing-overs are essential for physical linkage of homologous chromosomes to ensure accurate segregation in anaphase I. While arm cohesion is removed from chromosomes in prophase I, centromeric cohesins have to be conserved until anaphase I to guarantee faithful segregation of sister chromatids to opposite poles in meiosis II. In meiosis II, sister chromatid segregation proceeds as in mitosis [72, 73].

6.5   Mechanism of error prevention and correction

The initial capture of kinetochores by microtubules is a stochastic process and therefore prone to error. After nuclear envelope breakdown, microtubules invade the previously nuclear space in their search for kinetochores. Depending on the spatial orientation of chromosomes and kinetochore, sister kinetochores might be captured by microtubules emanating from the same pole or from opposite poles. To ensure proper chromosome segregation, sister kinetochores have to be attached to the mitotic spindle in a bipolar (also termed amphitelic) fashion with one sister kinetochore being attached to one pole, while the other one is attached to the other pole [93]. Early in prophase, only one kinetochore is attached to microtubules (monopolar attachment). If the second kinetochore is captured by microtubules emanating from the opposite pole, chromosome segregation will occur correctly. However, if the second kinetochore is captured by microtubules from the same pole (syntelic attachment), both chromatids will segregate to the same daughter cell resulting in aneuploidy. In another configuration, both sister kinetochores are attached to opposite poles, but one of them is also attached to the second pole (merotelic attachment). In this case, one chromatid segregates at the onset of anaphase, while the other left behind at the metaphase plate unable to move because of pulling forces from both poles (Fig. 25) [93].
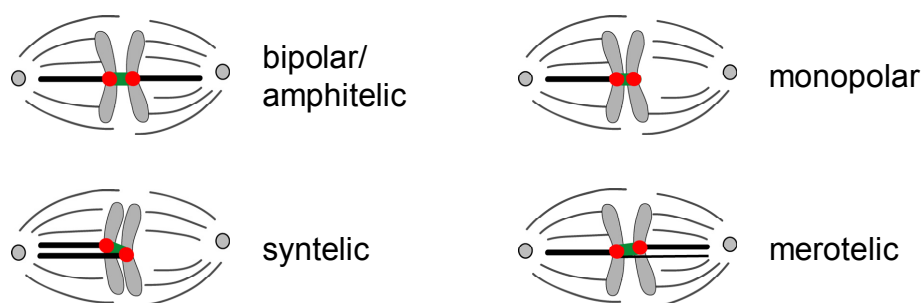
Figure 25 **Types of attachment.** For accurate chromosome segregation sister kinetochores have to attach to microtubules emanating from opposite spindle pole (bipolar/amphitelic). In the case of monopolar attachment, only one kinetochore is linked by microtubules to the spindle pole. Attachment of both sister kinetochores to the same pole leads to syntelic attachment. Merotelic attachment results from attachment of one sister kinetochore to both poles.

Cells have developed different mechanisms to ensure accurate kinetochore–microtubule attachment and subsequent chromatid segregation. One way in which bipolar attachment is favored is by the back-to-back arrangement of kinetochores [94-96]. The rigid arrangement of kinetochores is part of a passive mechanism that, after initial attachment of a kinetochore, orients the other one to the opposite pole. The mitotic kinetochore lies in a pit of the chromosome which further helps to avoid incorrect attachment [97]. Because of this hidden construction only microtubules that enter the pit have a chance to capture the kinetochore and the probability of this event is strongly increased if the kinetochore faces the pole. Furthermore, if the first kinetochore is attached to a pole, its sister is not only oriented away from the pole but also shielded from microtubules. This mechanism reduces the amount of syntelic attachment early in prometaphase after nuclear envelope breakdown when chromosomes are randomly distributed in the cell and are likely to be attached with both kinetochores to the same pole.

Besides preventive mechanisms to avoid mis-attachment, cells also possess active mechanisms to detect and correct mis-attached chromosomes. Faulty attachments are unstable and do not prevail. Since microtubules undergo constant growth and shrinkage, a feature called dynamic instability [98], they will shrink and disappear if the attachment is incorrect and removed. New microtubules will emanate from the poles and search for and capture kinetochores. If a correct attachment is made, it is stable and will persist [99]. The sensor for incorrect attachment is a protein complex located at the kinetochore. This protein complex, called the "mitotic checkpoint" or "spindle assembly checkpoint" senses lack of attachment and absence or reduction of tension across sister kinetochores.

6.6   The Spindle Assembly Checkpoint

The metaphase to anaphase transition is the most crucial moment in mitosis. At this transition the duplicated sister chromatids are separated and segregated to the daughter cells. To ensure that all chromatids are distributed correctly, a surveillance mechanism has developed that delays anaphase onset

until all sister chromatids are aligned at the metaphase plate and attached to microtubules from opposite poles [93].

The first molecular components of the spindle assembly checkpoint were discovered in genetic screens in yeast for mutants that failed to arrest in mitosis upon spindle damage [100-102]. These screens identified seven genes Bub1-3 (budding uninhibited by benzimidazole), Mad 1-3 (mitotic arrest deficient), and Mps1 (monopolar spindle 1). Vertebrate orthologues of Bub1 and 3 [103, 104], Mad1-3 [104-106], and Mps1 [107] have been found and were shown to be implicated in spindle assembly checkpoint control.

Upon the onset of mitosis, Bub and Mad proteins localize to kinetochores and monitor microtubule attachment and tension between sister kinetochores [103, 104, 106]. Precocious progression into anaphase is inhibited by direct binding of the APC/C activator Cdc20 to Mad2 and Mad3 (mammalian homologue is named BubR1) [91, 92]. This inhibitory system is so sensitive that a single unattached kinetochore is sufficient to delay mitotic progression for at least three hours [108]. Although the defects that lead to checkpoint activation are well known, it is difficult to decipher the specific function of each checkpoint protein because of the intimate connection of tension between sister kinetochores and microtubule attachment. However, it seems that each checkpoint protein has a distinct function in checkpoint signaling. Best understood is the role of Mad2, which specifically localizes to unattached kinetochores and leaves as soon as microtubules bind [109]. Mammalian kinetochores bind on average 25 microtubules and the amount of Mad2 at the kinetochore is inversely proportional to the number of attached microtubules. Localization of Mad2 to kinetochores is highly dynamic and removal of microtubule attachment leads to re-localization of Mad2. Bub1 is a serine/threonine protein kinase that is implicated in the regulation of chromosome congression and cohesion [110-112]. Bub1 is required for the kinetochore localization of other checkpoint proteins like Mad1, Mad2, and BubR1 [113, 114]. Bub1 participates in checkpoint mediated APC/C inhibition by phosphorylating Cdc20 [115]. Mad1 and Bub3 appears to act as scaffolding proteins that are required for the localization of Mad2, Bub1 and BubR1 to the kinetochore [116, 117].

6.7 Function and structure of BubR1

BubR1 is shown to have checkpoint-dependent and -independent roles. Depletion of BubR1 by siRNA leads to override of the spindle assembly checkpoint. Upon checkpoint activation, BubR1 binds Cdc20 and thereby inhibits APC/C [91, 92]. BubR1 is further implicated in the regulation of kinetochore-microtubule attachment possibly by influencing Aurora B kinase activity [118]. Depletion of BubR1 results in defects in the regulation of microtubule attachment by increased Aurora B kinase activity [118].

Both in mammals and yeast, BubR1/Mad3 has an N-terminal Bub3-binding domain that is conserved in Bub1 (61% homology on amino acid level) and required for kinetochore localization (Fig. 26) [103]. However, in contrast to yeast Mad3, mammalian BubR1 possess a C-terminal Bub1-like kinase domain (homology with Bub1 is 47% on amino acid level) which has been implicated in BubR1's checkpoint function and is stimulated by binding of the kinesin-related motor protein Cenp-E [104, 119]. While BubR1 has an N-terminal KEN box, it is not known if the KEN box targets BubR1 for degradation by APC/C [120].
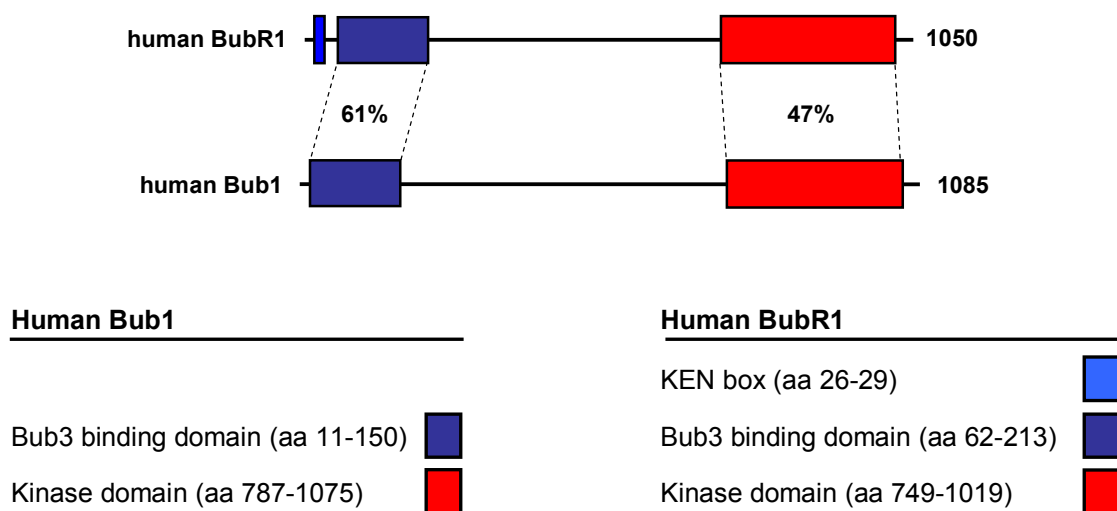
Figure 26 **Scheme of BubR1 and Bub1 protein structure and homology.** BubR1 and Bub1 both possess an N-terminal Bub3-binding domain and C-terminal kinase domain. Furthermore, BubR1 has a KEN box at the N-terminus.

6.8   Sister chromatid cohesion

From the end of DNA replication to the onset of anaphase, sister chromatids are linked by cohesion which is essential for accurate sister chromatid segregation. Cohesion between sister chromatids is essential for generating tension, which is an indication of the attachment status and is monitored by the spindle assembly checkpoint [121]. In budding yeast, each kinetochore binds to a single microtubule and tension alone is sufficient for error detection and correction, and to achieve correct bipolar attachment [122]. Kinetochores of mammalian cells, however, attach approximately 25 microtubules to each kinetochore and therefore need additional, geometric mechanisms such as rigid back-to-back orientation to minimize mis-attachment [94-96].

Chromosome cohesion is established by the cohesin protein complex consisting of members of the SMC (structural maintenance of chromosome) protein family, Smc1 and Smc3, as well as Scc1 and 3 [123, 124]. Smc1 and 3 are thought to form heterodimers that topologically enclose the DNA in a V-shaped structure whose ends are linked by Scc1 [125].

In vertebrate mitosis, cohesins are released in a two-step process. In prophase and prometaphase cohesins are removed from chromosome arms in an Aurora B kinase and Polo-like kinase 1 dependent manner [126, 127]. Centromeric cohesion is maintained until anaphase onset and its removal is APC/C-dependent. Upon satisfaction of the spindle assembly checkpoint, APC/C is activated leading to the degradation of securin and activation of the cysteine protease separase [89, 90]. Separase cleaves Scc1 and thereby opens the cohesin ring which releases sister chromatids [128].

Besides the cohesin complex, other proteins have been identified that are involved in protection of centromeric cohesion. Genetic screens in *Drosophila* found the Ord and Mei-S332 genes [129, 130]. While no homologs have been identified for Ord, Mei-S332 was recently shown to be related to gene family in yeast, called shugoshins (Sgo's) [112, 131, 132]. As with Mei-S332, the lack of shugoshins leads to precocious separation of sister chromatids and mis-segregation in meiosis I and mitosis [112, 131, 132].

6.9   The Shugoshin protein family

The first member of the shugoshin family, Mei-S332, was discovered in 1976 [133] and further characterized in 1992 as a gene involved in sister-chromatid cohesion [129]. However, since the homology of shugoshins (Sgo's) is low and restricted to a coil-coil region at the N-terminus and a basic region at the C-terminus, no homologs in other organisms were found until 2004 [112]. While *Saccharomyces cerevisiae*, *Drosophila melanogaster*, *Caenorhabditis elegans*, and *Xenopus laevis* only possess one Sgo gene, *Schizosaccharomyces pombe*, mammals and plants possess two Sgo genes [112, 129, 134]. Sgo1 and 2 localize to the inner kinetochore/centromere from prophase until metaphase and are undetectable by anaphase onset [112, 134]. Mei-S332 is removed from kinetochores at the metaphase to anaphase transition by phosphorylation by Polo-like kinase 1 [135]. Furthermore, yeast and mammalian Sgo1 are shown to be degraded by APC/C [112, 134]. Deletion of Sgo1 in yeast leads to loss of centromeric cohesion in anaphase I and subsequently non-disjunction of sister chromatids in meiosis II. During meiosis I, Sgo1 localizes to centromeric chromatin and protects the meiosis-specific cohesin subunit Rec8 (Scc1 in mitosis) from cleavage by separase. *S. cerevisiae* possess only one Sgo, which is expressed and functions in mitosis and meiosis [131]. In *S.pombe*, however, Sgo1 seems to function specifically in meiosis, while Sgo2 has been implicated in both mitosis and meiosis. Deletion of Sgo2 results in a low degree of non-disjunction of homologous chromosomes in meiosis I and mis-segregation of sister chromatids in mitosis [112]. In mammals, both Sgo1 and 2 are expressed in mitosis and their depletion by siRNA leads to loss of cohesion, sister chromatid mis-segregation, and mitotic arrest [134, 136]. The loss of centromeric cohesion in mitosis after depletion of Sgo1 depends on the prophase cohesin removal pathway which acts on chromosome arms and can be suppressed by expression of non-phosphorylatable Scc3 [137]. Taken together, the observations from Sgo1 deletion in yeast and Sgo1 depletion in mammalian cells suggest that Sgo1 protects centromeric cohesion by different mechanisms: in meiosis by preventing separase cleavage of Scc1 and in mitosis by circumventing phosphorylation-induced dissociation of Scc3 [137].

Interestingly, in yeast as well as in mammals shugoshin localization to centromeric regions depends on Bub1, suggesting a possible connection

between protection of centromeric cohesion and the spindle assembly checkpoint [112, 138, 139]. Furthermore, a screen in *S.cerevisiae* for genes involved in sensing tension across sister kinetochores in mitosis identified Sgo1 [140]. Sgo1 mutants are unable to detect lack of tension and complete mitosis instead of arresting in metaphase upon spindle assembly checkpoint activation. However, Sgo1 mutants undergo a checkpoint-dependent mitotic arrest upon loss of microtubule-kinetochore attachment. In addition, Sgo1 mutants showed a defect in chromosome segregation that could be rescued by delaying anaphase onset. A role for Sgo1 in tension sensing is further supported by the observation that mammalian Sgo1 bundles microtubules and is involved in microtubule dynamics [134]. It is possible that Sgo1 only interacts with microtubules in the absence of tension, while with bi-orientation and tension, kinetochores are pulled apart and the physical interaction of microtubules with Sgo1 is abolished at the inner kinetochore/ centromere [140]. Another link to the tension-sensing branch of the spindle assembly checkpoint comes from the observation that Aurora B kinase phosphorylates the *Drosophila* homolog of Sgo1, Mei-S332 [141]. Phosphorylation of Mei-S332 seems to be required for stable binding of Mei-S332 to centromeres. Aurora B kinase is a member of a conserved family of kinases that is involved in sensing lack of tension between sister kinetochore and removing microtubules from kinetochores that are not under tension [142-145]. Loss of Aurora B kinase activity leads to defects that appear to be caused by altered tension [146]. Because the loss-of-function phenotypes of Mei-S332/Sgo1 and Aurora B kinase are similar, and Aurora B kinase is required for stable association of Mei-S332/Sgo1 with the kinetochore, it is likely that both proteins function in the same pathway.

Recent reports found that yeast and mammals shugoshins interact with protein phosphatase 2A (PP2A) at the centromere [136, 147, 148]. In yeast, centromere localization of PP2A in meiosis depends on Sgo1 [136, 147], while in mitotic mammalian cells Sgo2 is required for centromere localization of PP2A, which in turn targets Sgo1 to centromeres [136]. PP2A seems to protect cohesion by preventing phosphorylation of Rec8 in meiosis and Scc3 in mitosis.

7.   Results

7.1   Characterization of BubR1 protein

To investigate BubR1's function, a monoclonal antibody against BubR1 was developed and used for characterization of BubR1 by Western blotting and immunofluorescence. Protein expression and modifications of BubR1 in interphase and under mitotic arrest was analyzed. HeLa cells were synchronized in interphase by double thymidine block and placed under checkpoint arrest with the spindle-damaging agents nocodazole or Taxol. Nocodazole depolymerizes microtubules leading to loss of attachment and tension. Taxol stabilizes microtubules and abolishes microtubule dynamics leaving microtubule-kinetochore attachment intact, but abolishes tension across sister kinetochores. Cells from these two conditions as well as after nocodazole wash-out were lysed and samples were analyzed by SDS-PAGE electrophoresis and Western blotting using anti-BubR1 antibody (Fig. 27).
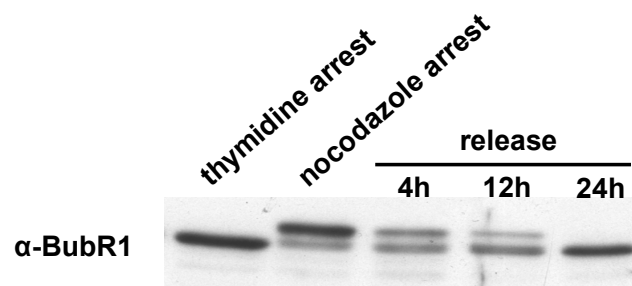
Figure 27 **BubR1 Western blot.**   Under thymidine arrest in interphase, BubR1 appears as a single band of approximately 120kDa. Upon nocodazole-induced mitotic arrest, BubR1 exhibits a gel-mobility shift and a second slower migrating band appears.
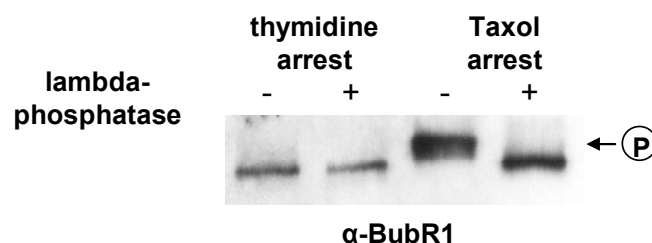
Figure 28 **BubR1 Western blot of lambda phosphatase treated lysates.**   HeLa cells were arrested in interphase with thymidine and in mitosis with Taxol. Treatment with lambda-phosphatase abolished the observed mobility shift of BubR1.

In interphase (thymidine arrest), BubR1 migrates as a single band of approximately 120kDa. Upon checkpoint activation, a slower migrating band appears which disappears as cells progress in cell cycle after nocodazole is washed out. To determine if the mobility shift of BubR1 in extracts from HeLa cells under mitotic arrest was due to phosphorylation, lysates were treated with lambda phosphatase to dephosphorylate all proteins. The dephosphorylated lysates were analyzed by SDS-PAGE electrophoresis and Western blotting using anti-BubR1 antibody. Treatment with lambda phosphatase abolished the mobility shift of BubR1, suggesting that the mobility shift in BubR1 is due to phosphorylation (Fig. 28).
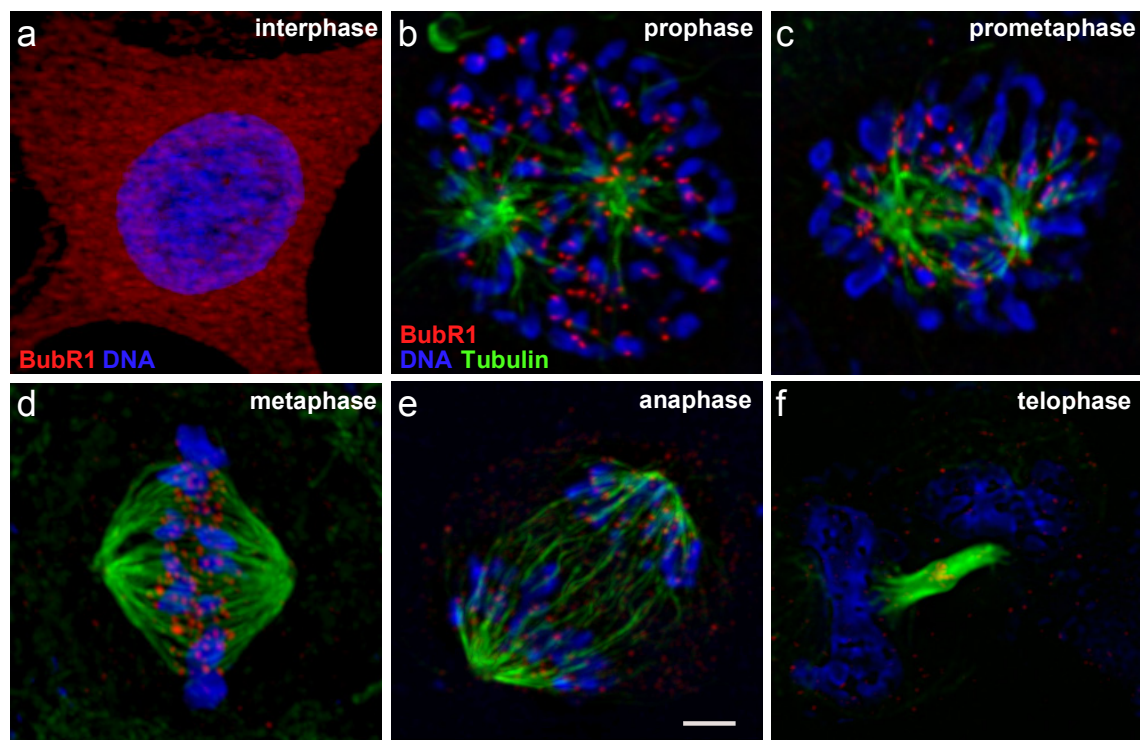
Figure 29 **BubR1 localization throughout the cell cycle.** Micrographs of anti-BubR1 (red) immunofluorescence at different cell cycle stages. **a.** In interphase BubR1 localizes to the cytoplasm. **b-e.** Upon onset of mitosis, BubR1 binds to kinetochores and persists beyond the induction of anaphase. **f.** In telophase BubR1 is found at the midbody. Microtubules are green, DNA is blue. Images are maximum projection of z-stacks of deconvolved spinning disc confocal optical sections every 0.267µm through the entire spindle. Scale bar is 3µm.

The subcellular localization of BubR1 at different cell cycle stages in HeLa cells was investigated by immunofluorescence. During interphase BubR1 localizes to the cytoplasm. In early prophase BubR1 binds to kinetochores and

stays on throughout mitosis. At the metaphase-to-anaphase transition, BubR1 intensity at kinetochores is reduced but remains detectable. Late in telophase BubR1 is found at the midbody (Fig. 29)

7.2   Immunoprecipitation of BubR1 from mitotically-arrested HeLa cells

In order to better understand the function of BubR1 in spindle assembly checkpoint signaling, BubR1 was immunoprecipitated and precipitates were analyzed for post-translational modifications and associated proteins. For immunoprecipitation (IP), HeLa cells were synchronized in mitosis by addition of Taxol and collected by mitotic shake-off.

protein	protein coverage	# of unique peptides	total peptides
BubR1	32.2%	37	124
Bub3	36.9%	12	27
Bub1	22.9%	18	29
Sgo2	17.5%	17	17
Cdc20	20.4%	9	14
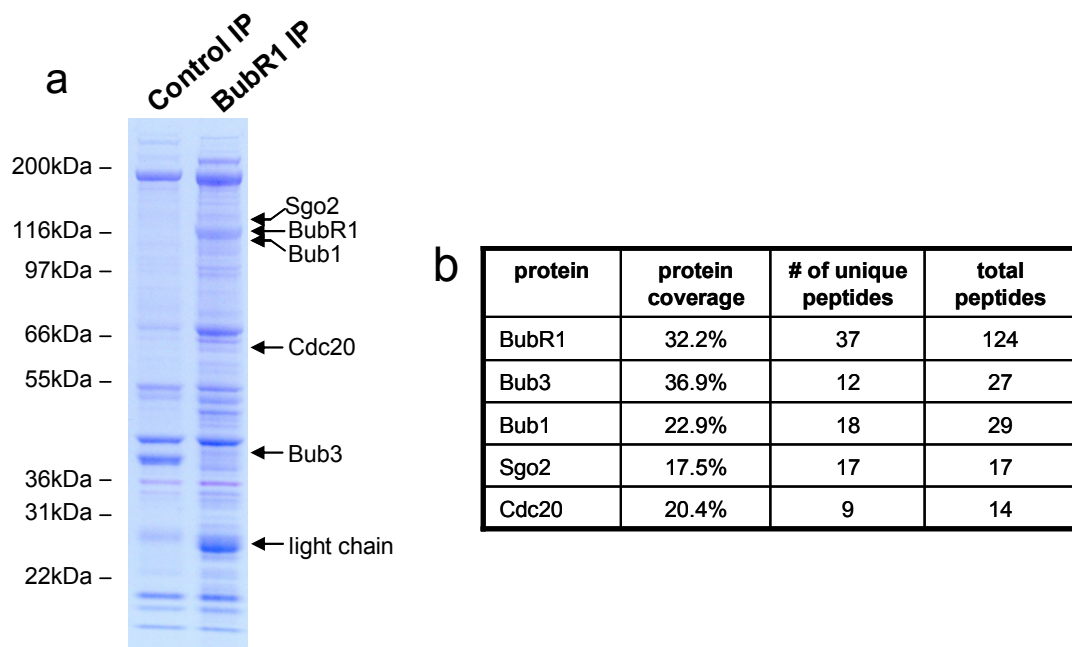
Figure 30 **BubR1 immunoprecipitation.** **a.** Coomassie blue-stained SDS-PAGE gel of BubR1 and control IP. Arrows indicate the regions of the gel from which Sgo2, BubR1, Bub1, Cdc20, Bub3 were identified by mass spectrometry, as well as the non-cross-linked light chain of the antibody. **b.** Table denoting protein coverage as a percentage of amino acid content of BubR1 and selected BubR1 interacting proteins, as well as the number of unique and total tryptic peptide matches as determined by mass spectrometry.

After lysis, anti-BubR1 antibody cross-linked to protein G Sepharose for BubR1 precipitation or protein G Sepharose alone as a control were added to the lysate. Precipitates were separated by SDS-PAGE electrophoresis and analyzed by Western blotting as well as Coomassie stain (Fig. 30a).

Mass spectrometric (µLC-FTICR MS/MS) analysis of the Coomassie gel was carried out by Dr. Scott Gerber in Dr. Steven Gygi's laboratory. In the mass spectrometric analysis of the BubR1 IP, only proteins specifically identified in the BubR1 IP lane and not in the control IP lane were further investigated. BubR1 was identified with a total number of peptides of 124 of which 37 peptides were unique (Fig. 30b). Furthermore, known BubR1 interacting proteins like Bub1, Cdc20, Bub1, and Bub3 were found [92], confirming the approach as suitable for investigation of BubR1 interacting partners. In addition, novel BubR1 interacting proteins such as Sgo2 were identified.

Besides the identification of interacting proteins, BubR1 itself was investigated for post-translational modifications especially phosphorylation. For phosphorylation analysis, immunoprecipitated BubR1 was independently digested with three different proteases (trypsin, chymotrypsin, and glu-C) to achieve maximum protein coverage. In this analysis 13 individual phosphorylation sites on BubR1 were identified (Table 1). The amino acid sequence of human BubR1 (accession number AAC06260) was submitted to online phosphorylation predictions programs (NetPhos 2.0 [149] Scan site [150]) for *in silico* identification of phosphorylation sites and prediction of upstream kinases.

The NetPhos 2.0 program predicts the likelihood for any serine (S), threonine (T), or tyrosine (Y) in a given amino acid sequence to be a true phosphorylation site [149]. Each S/T/Y amino acid residue in the sequences is scored with a value from 0 to 1, with 0.5 being the threshold. If a site has a score just above the threshold, it is unlikely that the site is phosphorylated *in vitro*. The phosphorylation sites identified in BubR1 by mass spectrometry in general received a high score. Although S435, S1043, and S720 were identified with high confidence as phosphorylated *in vivo* by mass spectrometry, S435 and S1043 scored just below the threshold (0.494 and 0.477, respectively) and S720 received a score of only 0.249, indicating that these sites are unlikely to be phosphorylated.

peptide	XCorr / MMA (ppm)
Trypsin digest	
TSESITSNEDVS*PDVCDEFTGIEPLSEDAIITGFR – S574	6.5 (+3) / 0.05
LELTNETSENPTQSP*WCSQYR – S720	4.1 (+3) / 0.52
EATHSSGFSGSSASVASTSSIK (1*, 2*, 3*) S676-S689	3.1 (+3) / 0.57
	2.3 (+3) /-1.79
LS*PIIEDSR – S670	2.4 (+2) /-0.89
LTS*PGALLFQ – S1043	2.4 (+2) / 0.42
NKS*PPADPPR – S543	2.2 (+2) /-0.02
EAELLTS*AEK – S435	1.7 (+2) / 2.02
Chymotrypsin digest	
KVGKLTS*PGALLFQ – S1043	4.1 (+2) /-0.55
SEKKNKS*PPADPPRVL – S543	3.1 (+3) /-0.67
SIKKLS*PIIEDSREATHSSGF – S670	2.4 (+3) /-0.24
Glu-C digest	
SITSNEDVS*PDVCDE – S574	3.0 (+3) /-0.40
AELLTS*AEKRAE – S435	1.6 (+2) /-1.11

Table 1 **Phosphorylation sites identified in BubR1.** Peptide sequence, cross-correlation scores, and mass measurement accuracy (MMA) in parts per million (ppm) of identified phosphorylated peptides. The phosphorylated amino acid residue is indicated with an asterisk.

Scan Site searches protein sequences for amino acid motifs that are phosphorylated by specific protein kinases (Fig. 31) [150]. The amino acid motif is a sequence of amino acids surrounding the phosphorylated residue that is recognized by a specific kinase. The probability that an amino acid is found in the motif at a certain position was determined by oriented peptide library technique and expressed as a selectivity value. Using Scan Site with medium stringency, only one of the identified phosphorylation sites of BubR1 was found and predicted to be phosphorylated by basophilic serine/threonine kinases.

The comparison between *in silico* prediction and *in vivo* detection of phosphorylation sites emphasizes the difficulties of *in silico* prediction of protein phosphorylation sites and their corresponding kinases. Although many serine, threonine and tyrosine residues in the BubR1 sequence yield high scores for potential phosphorylation sites using NetPhos 2.0 and ScanSite, only a few of them were found phosphorylated *in vivo* and not every one of them received a high score.
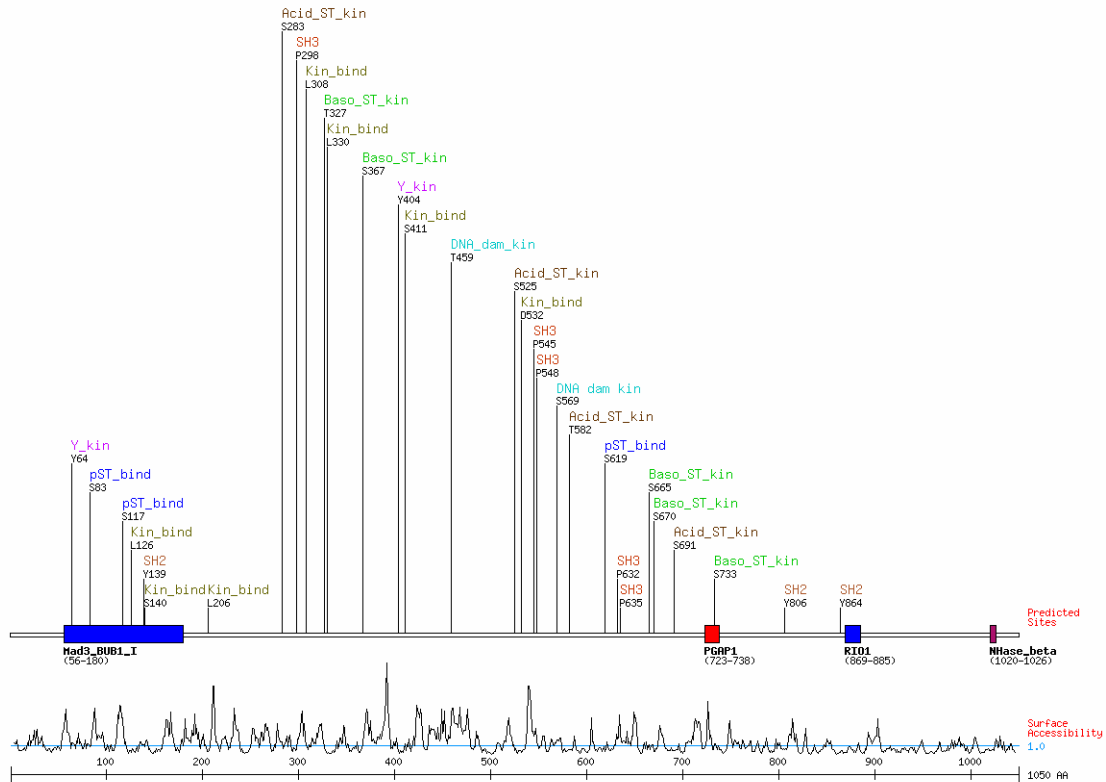
Figure 31 **Phosphorylation sites in BubR1 as predicted by Scan Site.** The amino acid sequence of BubR1 was entered into the Scan Site server and analyzed with medium stringency for kinase-specific phosphorylation sites.

7.3   Differential quantification of BubR1 phosphorylation sites and interacting proteins by SILAC

To assess the functional significance of BubR1 modifications and interactions in interphase and mitosis, a differential labeling strategy termed SILAC ("**s**table **i**sotope **l**abeling with **a**mino acids in **c**ell culture") was employed [151, 152]. SILAC is based on the metabolic incorporation of "heavy" amino acids into cells to substitute the natural distribution of isotopes of carbon and/or nitrogen with heavier stable isotopes (^{13}C, ^{15}N). In an experiment, two different cell populations to be compared are grown in media containing either "light" or "heavy" versions of L-arginine and L-lysine for at least six doublings to achieve complete incorporation of these essential amino acids. Heavy and light amino acids exhibit virtually identical chemical, metabolic, and analytical properties, but are readily distinguished during analysis by mass spectrometry. The labeled and

unlabeled cell populations can be differentially treated or otherwise manipulated for comparative purposes, then mixed, lysed and analyzed. Quantification of protein abundance in both states is performed by comparing the peak heights in mass spectra of the light and heavy peptide.

For assessing cell cycle dependent changes in BubR1 phosphorylation and protein-protein interactions, HeLa cells were grown in media containing "heavy" (U-$^{13}C_6$ -arginine and U-$^{13}C_6$$^{15}N_2$ -lysine) and "light" (normal isotopic distribution) amino acids. The "light" population was arrested in mitosis with Taxol, while the "heavy" population was arrested with thymidine in interphase (Fig. 32). Equal numbers of cells from both populations were mixed, lysed, and BubR1 was immunoprecipitated using anti-BubR1 antibody. Precipitates were analyzed by SDS-PAGE electrophoresis and Coomassie stain and submitted for mass spectrometric analysis.
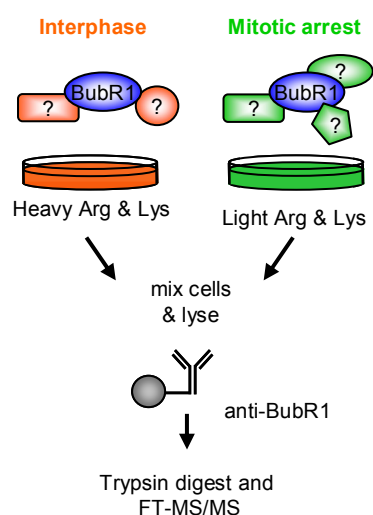
Figure 32 **Scheme of SILAC strategy to identify mitosis-specific interactors and phosphorylation sites of BubR1.** HeLa cells were labeled with "light" and "heavy" amino acids and arrested in mitosis or interphase, respectively. Equal numbers of cells from both conditions were mixed, lysed, and BubR1 was immunoprecipitated. BubR1 immunoprecipitates were analyzed by SDS-PAGE gel electrophoresis, trypsin digested, and analyzed by μLC-FTICR MS/MS.

Quantification of the relative intensities of BubR1 peptides showed that the total cellular amount of BubR1 found in interphase and during mitotic arrest was comparable (Fig. 33a).   However, the amount of BubR1-bound Sgo2 was

strongly reduced in interphase compared to mitosis (ration of 1: 30.36) (Fig. 33b). Quantification of known BubR1-interacting proteins revealed that Bub1 also specifically interacts with BubR1 in mitosis, while Cdc20 and Bub3 are associated with BubR1 in interphase as well as in mitosis (Fig. 33c).
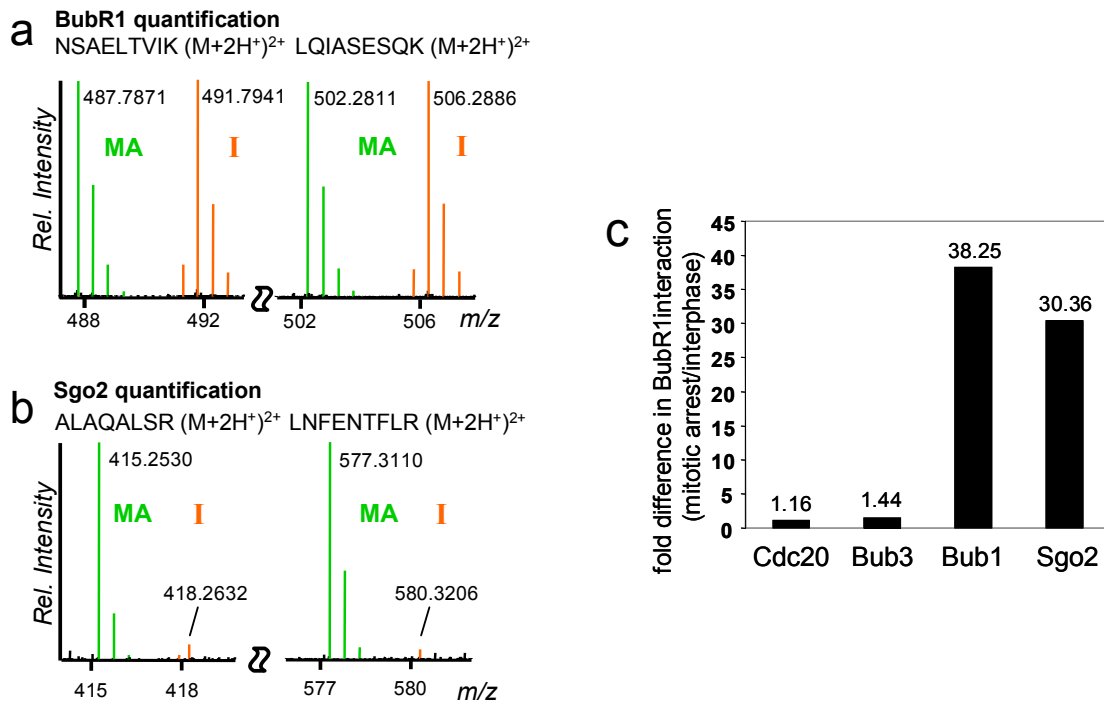
Figure 33 **Quantification of BubR1 and interacting proteins.** FTMS[1]-spectra of two peptides of immunoprecipitated BubR1 (**a**) and co-precipitated Sgo2 (**b**). The relative intensities of the "heavy" (interphase = I, orange) and "light" (mitotic arrest = MA, green) versions of both BubR1 peptides are comparable, while co-precipitated Sgo2 peptides show a decrease in the relative intensity of the "heavy" versus the "light" peak. **c.** Fold-changes in BubR1 interaction of co-precipitated Cdc20, Bub3, Bub1 and Sgo2 SILAC peptide pairs in mitotic-arrest versus interphase.

The SILAC analysis of the phosphorylation status of BubR1 in interphase and mitosis yielded quantitative data for the non-phosphorylated species of all previously identified phosphorylated peptides. Furthermore, for many peptides, the corresponding phosphorylated species was also identified and quantified. The results are summarized in Table 2. Although the phosphorylated form of the peptide containing S435 and S574 was not detected, the peak intensity of the non-phosphorylated form did not change between interphase and mitosis, suggesting that only a small portion of the protein is phosphorylated at those

residues in mitosis or that the ratio of phosphorylated to non-phosphorylated peptide does not change between interphase and mitotic arrest. The ratio of phosphorylated and non-phosphorylated peptide under mitotic arrest and in interphase showed large, reciprocal differences for S670 and S1043. These sites seem to be specifically phosphorylated in mitosis and are therefore potentially important for BubR1's function in mitosis. The non-phosphorylated form of a peptide containing a cluster of phosphorylation sites (amino acid 672-693) that was previously identified as singly-, doubly-, and even triply-phosphorylated, also exhibited a significant difference in abundance in mitosis versus interphase (22:1). Although several of these phosphorylated forms were identified in the SILAC experiment, their heterogeneity and multiplicity of forms resulted in dilution to below an acceptable signal-to-noise threshold for quantification. Other sites, such as S543 and S720, were also more abundant in their phosphorylated form in mitosis and in their non-phosphorylated in interphase, although these ratios were lower. Although this analysis yielded information about the relative abundance of the phosphorylated and non-phosphorylated form of these peptides in interphase and under mitotic arrest, their absolute abundance can not be determined using the SILAC approach.

amino acid locus	phosphorylated peptide mitotic arrest/interphase	unphosphorylated peptide mitotic arrest/interphase
S435	N/A	1/1.2
S543	7/1	1/5.2
S574	N/A	1/1.1
S670	134/1	1/114
S676-S689	N/A	1/22
S720	12/1	1/17
S1043	98/1	1/105

Table 2 **Quantification of BubR1 phosphorylation sites during mitotic arrest and interphase.** Ratios of peak intensities of phosphorylated and unphosphorylated peptides of BubR1 in mitosis and interphase.

Taken together, these results indicate that certain sites in BubR1 are phosphorylated in mitosis as well as interphase, while other ones seem to be specifically phosphorylated in mitosis. It is likely that mitosis-specific interactions

of BubR1 depend on post-translational modifications. Furthermore, mitosis-specific modifications and interactions might influence BubR1's behavior during the cell cycle, affecting nuclear import, kinetochore localization, and checkpoint signaling.

7.4   Investigation of BubR1 phosphorylation by mutagenesis

The function of BubR1 phosphorylation sites was investigated using a site-directed mutagenesis approach. The cDNA of BubR1 was cloned into a retroviral expression vector (pMX) and the codons corresponding to the identified phosphorylation sites were mutated to code for alanine instead of serine or threonine (Fig. 34). Furthermore, codon 670 to 689 were deleted from the cDNA to completely remove the cluster of phosphorylation sites. In order to distinguish between endogenous and heterologous expressed BubR1, a six-myc-tag was added to the N-terminus of the BubR1 coding sequence. The cell pools were synchronized in interphase with thymidine and with Taxol in mitosis and analyzed by Western blotting and immunofluorescence.
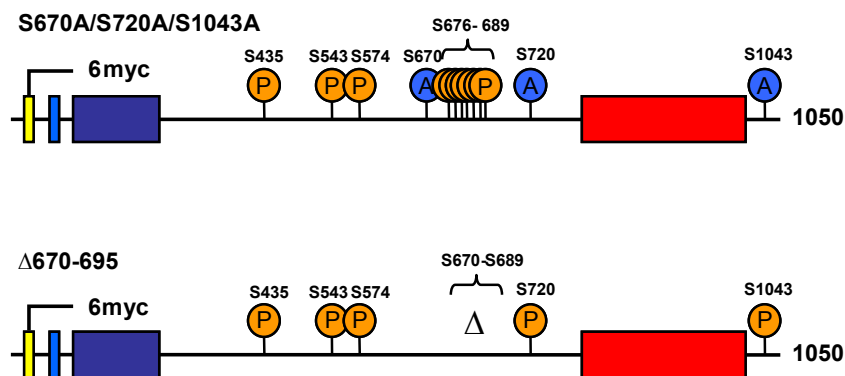
Figure 34   **Schema of BubR1 mutants.**   Scheme of BubR1 protein structure with phosphorylation sites. Upper drawing shows BubR1 triple point mutant with S670A, S720A, and S1043A. Lower drawing describes the deletion amino acid 670 to 689 of BubR1.

The phosphorylation-dependent mobility shift of endogenous BubR1 observed upon mitotic arrest was recaptured in heterologously expressed 6myc-BubR1. Western blot analysis of different single, double and triple point mutants also exhibited a mobility shift. However, deletion of codon 670 to 689 abolished

the mobility shift leading to the same migration behavior of BubR1 in mitosis as in interphase (Fig. 35). This observation suggests that one or more sites in this cluster of serine or threonine residues are responsible for the observed mobility shift. The deletion included S670 which is one of the sites found to be specifically phosphorylated in mitosis. Neither the S670A single point mutation, the double point mutation S670A/S1043A, nor the triple point mutations S670A/S720A/S1043A influenced 6myc-BubR1 migration behavior. Therefore, it is likely that sites found in S676-S689 by themselves or in combination with S670 are responsible for the mobility shift.
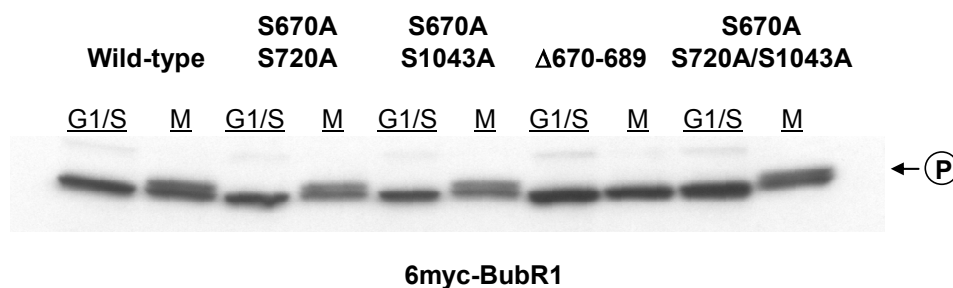
6myc-BubR1

Figure 35 **Western blot of 6myc-BubR1.** Cell populations of wild type and mutant 6myc-BubR1 were synchronized in interphase and mitosis and analyzed by SDS-PAGE electrophoresis and Western blotting. Single, double and triple point mutants of BubR1 showed migration behavior like wild type BubR1. Deletion of amino acids 670 to 689 abolished the phosphorylation-dependant mobility shift.

To investigate the influence of BubR1 phosphorylation on sub-cellular localization, cells were transduced with wild type and mutant BubR1 and analyzed by immunofluorescence. 6myc-tagged wild type and point-mutated BubR1 behaved like endogenous BubR1 in that it localized in interphase to the cytoplasm and to kinetochores from early prophase on. The 670-689 deletion mutant was also cytoplasmic in interphase and localized in prophase to the kinetochore. However, upon congression of chromosomes in metaphase, the deletion mutant departed from kinetochores and did not bind again to kinetochores during later stages of mitosis (Fig. 35). While phosphorylation of amino acid residues in the cluster is not required for initial binding of BubR1 to the kinetochore, it seems to be necessary for the continuation of kinetochore localization upon congression. Localization of wild type, point mutants and the deletion mutant to the midbody in telophase was not observed.
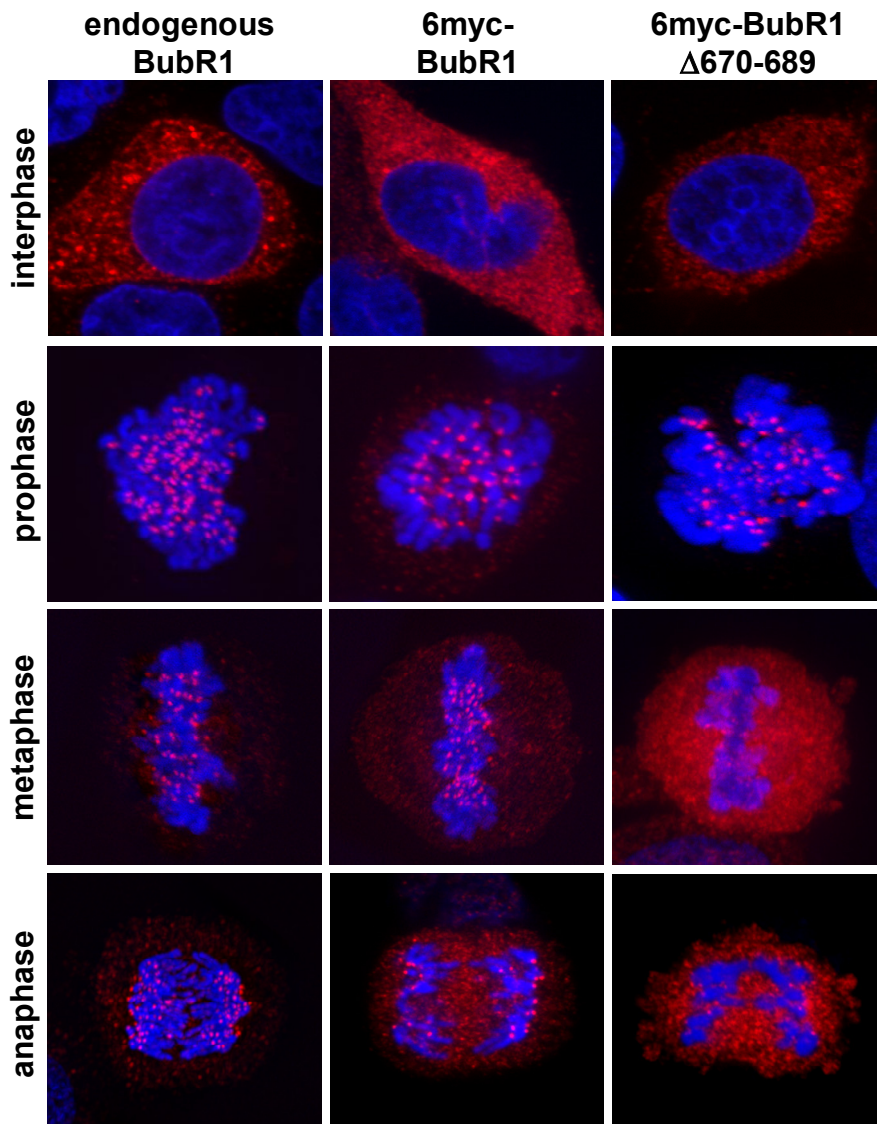
Figure 35 **Immunofluorescence micrographs of endogenous and heterologous BubR1.**
First panel down shows endogenous BubR1 localization at different mitotic phases.
Heterologous expressed BubR1 as well as BubR1 point mutants localize to the cytoplasm in
interphase and to kinetochores in mitosis (second panel down). Deletion of amino acids 670 to
689 abolishes kinetochore localization of BubR1 upon congression (last panel down).

Interestingly, this localization pattern was reminiscent of that of another
checkpoint protein, Bub1 [103]. In interphase, Bub1 is found in the nucleus and
binds early in prophase to kinetochores where it stays on until congression. As
chromosomes attach to the spindle and align under tension on the metaphase
plate, Bub1 leaves the kinetochore (Fig. 36). Bub1 and BubR1 exhibit significant
sequence homology in the N-terminal Bub3 binding domain and in the C-terminal
Bub1-like kinase domain. Kinetochore localization of both proteins depends on
their interaction with Bub3 via an N-terminal interaction domain.
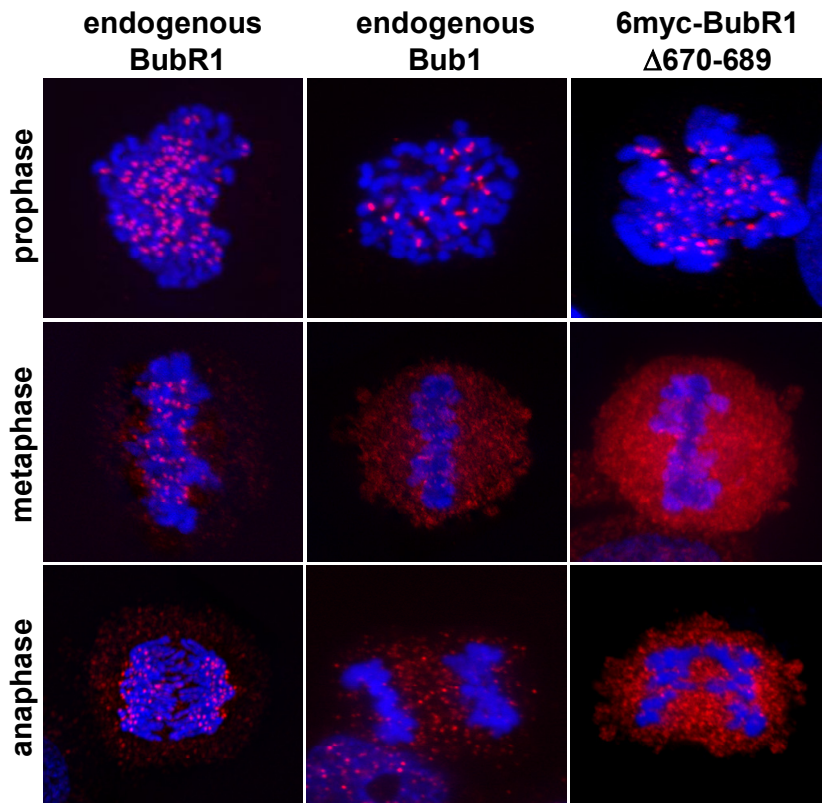
Figure 36 **Immunofluorescence micrographs of endogenous Bub1 and BubR1 and heterologous BubR1 deletion mutant.**   Localization of endogenous BubR1 (first panel down), Bub1 (second panel down), and heterologous 6myc-BubR1Δ670-689 (third panel down) at different mitotic phases. Note Bub1 is of the kinetochore upon congression.

It is possible that the specific localization pattern of BubR1 and Bub1 is determined by post-translational modifications. Sequence comparison of BubR1 and Bub1 revealed that many serines of the cluster region found in BubR1 are conserved in Bub1 (Fig. 37). However, the surrounding residues are not conserved. Therefore it is possible that amino acid substitutions of the residues surrounding serines created or destroyed kinase motifs leading to specific phosphorylation patterns.

BubR1:   670 – SPI I EDS–REATHSSGFSGS – 689
SPI E S ++A   S   +S S
Bub1:   655 – SPIQEKSPKQALSSHMYSAS – 689

Figure 37 **Sequence alignment of the cluster regions in BubR1 and Bub1.**   Mostly serines, but not neighboring amino acids in the cluster region of BubR1 are conserved in Bub1, making it unlikely that the same kinases will phosphorylate both proteins in this region.

Furthermore, heterologous expression of BubR1 mutants in HeLa cells did not influence cell cycle progression or mitotic arrest upon treatment with spindle poisons. Because BubR1 mutants were introduced into HeLa cells by retroviral transduction, it is likely that the low levels of heterologous expressed mutant protein did not efficiently compete with the approximately ten-fold higher endogenously expressed BubR1 (data not shown).

7.5   BubR1 and Bub1 domain swap

Bub1 localizes to kinetochores from prophase until congression in metaphase. It has been shown that the N-terminus of Bub1 (N-Bub1) by itself binds to kinetochores and stays there as long as full-length Bub1 [103]. To test if the duration of N-Bub1 localization to the kinetochore can be altered by addition of the C-terminus of BubR1, which includes the cluster of phosphorylation sites (amino acid 670-689), both were fused. Moreover, to determine if a change in duration in kinetochore binding is due to phosphorylation in the cluster region, the N-terminus of Bub1 was also fused to the C-terminus of BubR1 lacking amino acids 670 to 689 (Fig. 38).
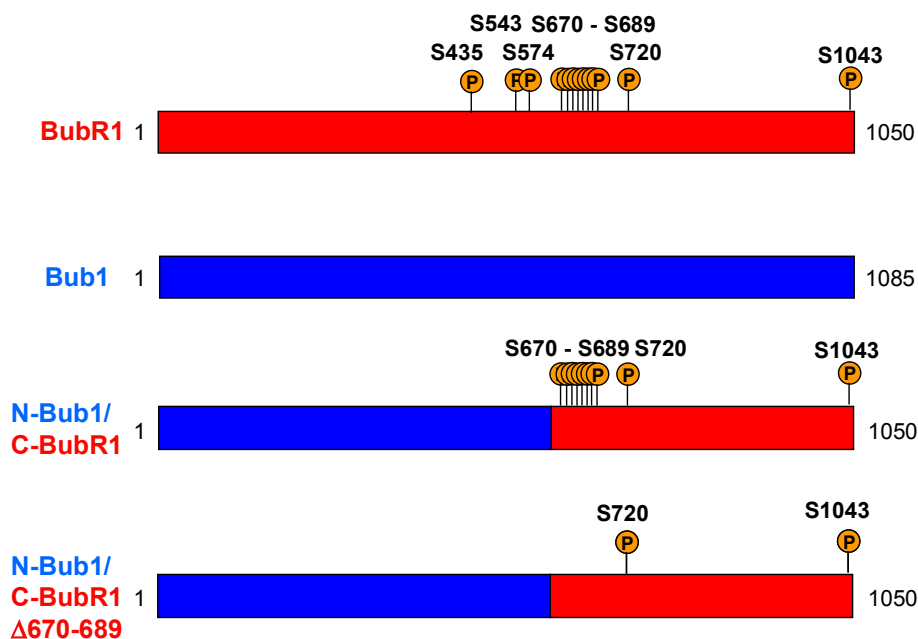
Figure 38   **Scheme of swapping constructs.** Depicted are schemes of BubR1, Bub1, as well as fusion constructs. The relative location of BubR1 phosphorylation sites is indicated.

While endogenous Bub1 was easily detected by anti-Bub1 antibodies at the kinetochore, heterologously expressed Bub1 was found in the nucleus but no kinetochore staining was observed in mitosis. However, heterologously expressed N-Bub1 localized correctly in interphase to the nucleus and in mitosis to the kinetochore until congression.   Upon onset of mitosis the fusion constructs bound to the kinetochore and stayed at the kinetochore beyond congression and was easily detected on anaphase kinetochores. N-Bub1/C-BubR1Δ670-689 localized to the cytoplasm in interphase and initially to kinetochores in prophase, however, it was absent from kinetochores upon congression (Fig. 39).
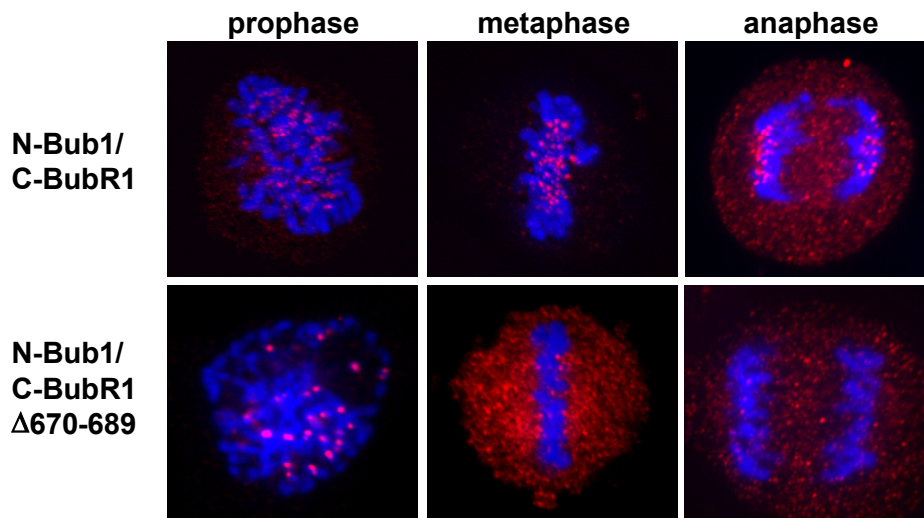
Figure 39 **Immunofluorescence micrographs of swapping constructs.** N-Bub1/C-BubR1 like BubR1 localizes to kinetochores beyond the onset of anaphase. N-Bub1/C-BubR1Δ670-689, however, initially binds to kinetochores in prophase but leaves upon congression.

7.6   Kinases involved in BubR1 phosphorylation

Several kinases including Cdk1, Polo-like kinase 1, and Aurora B kinase are involved in regulating mitotic processes and progression [74, 143, 153]. Different strategies were applied to investigate if one of these kinases is involved in BubR1 phosphorylation.
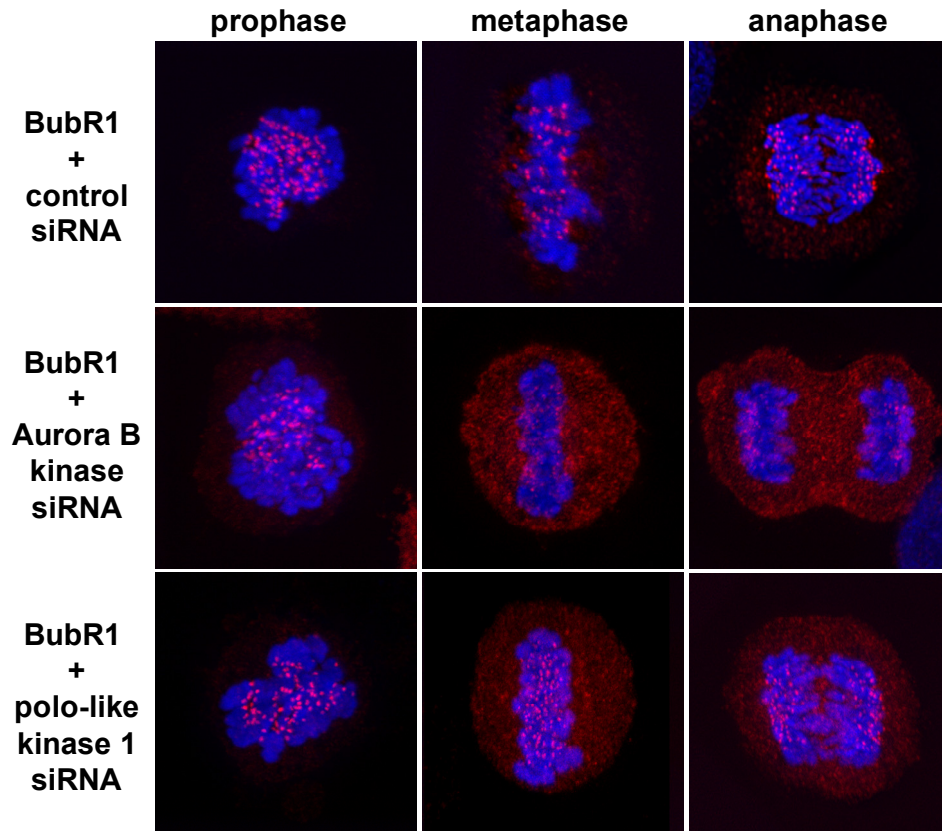
Figure 40 **Immunofluorescence micrographs of endogenous BubR1.** Treatment of HeLa cells with control or polo-like kinase 1 siRNA did not influence BubR1 localization. However, depletion of Aurora B kinase abolished kinetochore localization of BubR1 upon congression.

In a first attempt, HeLa cells were treated with Aurora kinase [146] and Cdk1 inhibitor [154] followed by investigation of BubR1's subcellular localization by immunofluorescence. While treatment with Cdk1 inhibitor had no effect on BubR1 localization, the Aurora kinase inhibitor abolished binding of BubR1 upon congression. Although the Aurora kinase inhibitor targets both Aurora kinase A and B, the observed phenotypes are thought to be dependant on Aurora B rather than Aurora A kinase [146]. However, to demonstrate that BubR1 localization depends on Aurora B and not Aurora A kinase, Aurora kinase B was specifically depleted from HeLa cells by siRNA. As with inhibition of Aurora kinases, depletion of Aurora B kinase abolished BubR1 localization at kinetochores upon congression (Fig. 40). Depletion of polo-like kinase 1 from HeLa cells had no influence on BubR1 localization.

The effect of kinase inhibition on BubR1's phosphorylation-dependant mobility shift upon mitotic arrest was investigated by Western blotting. HeLa cells transduced with wild type 6myc-BubR1 and 6myc-BubR1Δ670-689 were arrested in mitosis with Taxol and treated with Aurora kinase and Cdk1 inhibitor. 6myc-BubR1Δ670-689 did not exhibit a phosphorylation-dependent mobility shift upon mitotic arrest and treatment with either inhibitor did not influence 6myc-BubR1Δ670-689 migration behavior. Wild type 6myc-BubR1 did show a mobility shift upon mitotic arrest, which was reversed by treatment with Aurora kinase inhibitor but not with Cdk1 inhibitor (Fig. 41).
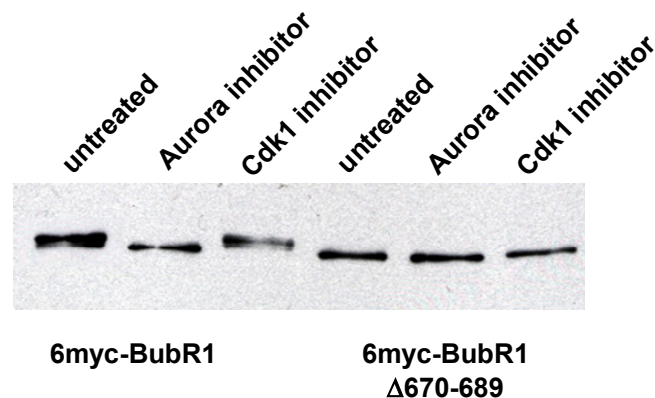
Figure 41 **Western blot analysis of 6myc-BubR1 and 6myc-BubR1Δ670-689 treated with kinase inhibitors.** HeLa cells transduced with 6myc-BubR1 or 6myc-BubR1Δ670-689 were arrested in mitosis with Taxol and treated with Aurora kinase and Cdk1 kinase inhibitor.

To prove that BubR1 is a direct target of Aurora B kinase, BubR1 was immunoprecipitated from interphase HeLa extracts and used as a substrate in *in vitro* kinase assay with purified human Aurora B kinase and γ-^{32}P-ATP. Because BubR1 is a kinase itself and tightly associated with Bub1, a control reaction without addition of Aurora B kinase was done. To ensure that Aurora B kinase was active under the experimental conditions, purified histones were used as substrates in a positive control. Both histones and BubR1 were phosphorylated by Aurora B kinase as judged by labeling with γ-^{32}P, but no auto-phosphorylation or phosphorylation of co-precipitating kinases was detected under the conditions used (Fig. 42).
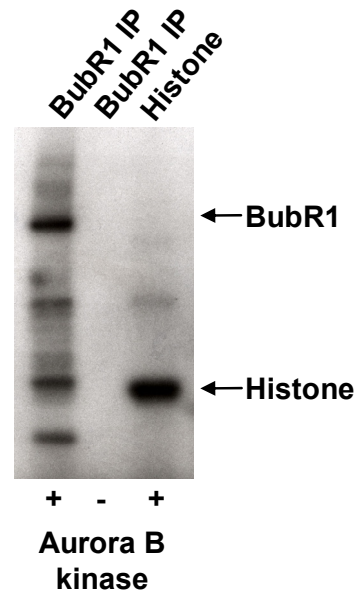
Figure 42 *In vitro* **kinase assay with Aurora B kinase.** Immunoprecipitated BubR1 was phosphorylated with or without Aurora B kinase in the presence of α-^{32}P-ATP.

Taken together, these observations from kinase inhibitor studies, siRNA, and *in vitro* kinase assays, it is likely that Aurora B kinase phosphorylates BubR1 *in vivo*. As observed with Aurora kinase inhibitor and Aurora B kinase siRNA, deletion of the amino acids 670- 689 abolished BubR1's mobility shift and induced early departure of BubR1 from kinetochores upon congression. This suggests that Aurora B kinase phosphorylates BubR1 in the cluster region and is responsible for BubR1's extended kinetochore localization.

7.7   Confirmation of BubR1-Sgo2 interaction

Sgo2 is one of the newly identified BubR1-interacting proteins that specifically binds to BubR1 in mitosis. Sgo2 is a member of the conserved family of shugoshin proteins. Sgo2 is implicated in sister chromatid cohesion and chromosome congression in yeast, flies, and mammals [112, 134, 155]. To further analyze the interaction between BubR1 and Sgo2, the Sgo2 coding sequence was cloned into the pMX vector for retrovirus production and HeLa cell populations expressing 6myc-Sgo2 were established.

To demonstrate that the interaction of BubR1 and Sgo2 is specific and direct, 6myc-Sgo2 was immunoprecipitated from Taxol arrested lysates and

precipitates were analyzed by mass spectrometry. One concern with regards to the BubR1-Sgo2 interaction was that BubR1 tightly binds Bub1 and Bub1 is required for the inner kinetochore localization of Sgo1 and Sgo2 in yeast [112]. Therefore it could be possible that the interaction between BubR1 and Sgo2 is mediated by Bub1. In the mass spectrometric analysis of the Sgo2 precipitate, the only checkpoint protein associated with Sgo2 was BubR1, confirming that the interaction with BubR1 is specific and direct and not mediated by Bub1. Furthermore, peptides corresponding to different subunits of protein phosphatase 2A and tubulin were detected in Sgo2 immunoprecipitates (Table 3).

protein	protein coverage	# of unique peptides	total peptides
Sgo2	49.1%	62	96
BubR1	23.6%	27	68
PP2a r65alpha	20.9%	12	12
PP2a r55alpha	26%	8	8
PP2a r56alpha	8.4%	3	3
PP2a r56epsilon	5.8%	2	2
SET protein	18.3%	4	4
Tubulin	57%	21	21

Table 3 **Sgo2-interacting proteins.** Protein coverage as a percentage of amino acid content of Sgo2 and selected Sgo2-interacting proteins, as well as the number of unique and total tryptic peptide matches as determined by mass spectrometry.

PP2A is a recently described shugoshin interactor which is involved in protection of centromeric cohesion [136, 147, 148]. The observed interaction with tubulin is intriguing, because mammalian Sgo1 was reported to bind and induce microtubule polymerization [134].

7.8   Characterization of Sgo2 protein
In yeast, Sgo2 is expressed in meiosis and mitosis and localizes to pericentromeric regions from prophase until the onset of anaphase [112]. To examine Sgo2 localization and expression during mammalian mitosis, a polyclonal antibody against human Sgo2 was made.

For Western blot analysis, HeLa cells were synchronized in interphase by double thymidine block and in mitosis with Taxol. Cells were collected, lysed and proteins separated by SDS-PAGE electrophoresis and detected by Western blot.
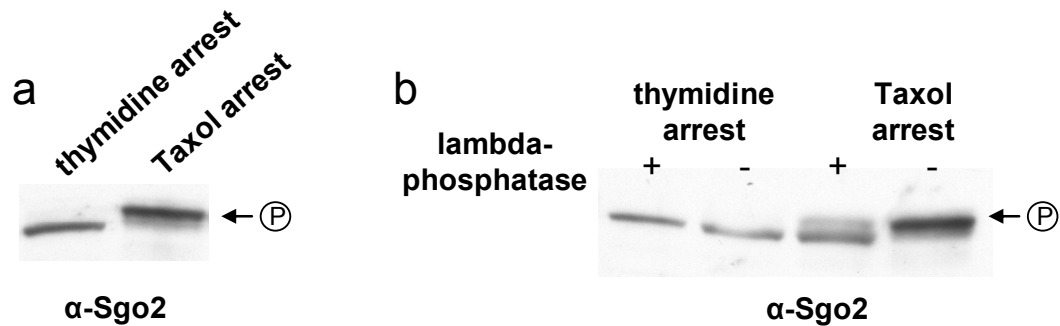
Figure 43 **Sgo2 Western blot. a.** In interphase Sgo2 migrates as a single band of approximately 135kDa. During mitotic arrest, Sgo2 is shifted to a slower migrating form. **b.** Lambda-phosphatase treatment reverses the gel-mobility shift of Sgo2 upon mitotic arrest.

Interphase extracts show Sgo2 as a single band of approximately 135kDa. Upon mitotic arrest, Sgo2 exhibits a gel-mobility shift and migrates slower (Fig. 43a). Lambda phosphatase treatment of mitotic extracts reverses Sgo2's mobility shift, indicating that Sgo2 is phosphorylated during mitotic arrest and therefore migrates more slowly (Fig. 43b).

Sgo2's subcellular localization during mitosis in HeLa cells was analyzed by immunofluorescence. Although endogenous Sgo2 was detectable in interphase by Western blotting, no Sgo2 signal was seen by immunofluorescence in interphase. Upon onset of mitosis, Sgo2 localizes to kinetochores where it stays until the onset of anaphase and then disappears (Fig. 44). To more specifically define where Sgo2's resides at the kinetochore, cells expressing 6myc-Sgo2 were co-stained for Sgo2 and different kinetochore markers. Sgo2 co-localizes with the inner centromere protein Aurora B kinase and human auto-antibodies from CREST patients, it partially overlaps with BubR1 and Bub1, and is found inside of the outer kinetochore proteins Hec-1 and Cenp-F (Fig. 45) [156]. This staining pattern is consistent with Sgo2 localization to pericentromeric chromatin in yeast.
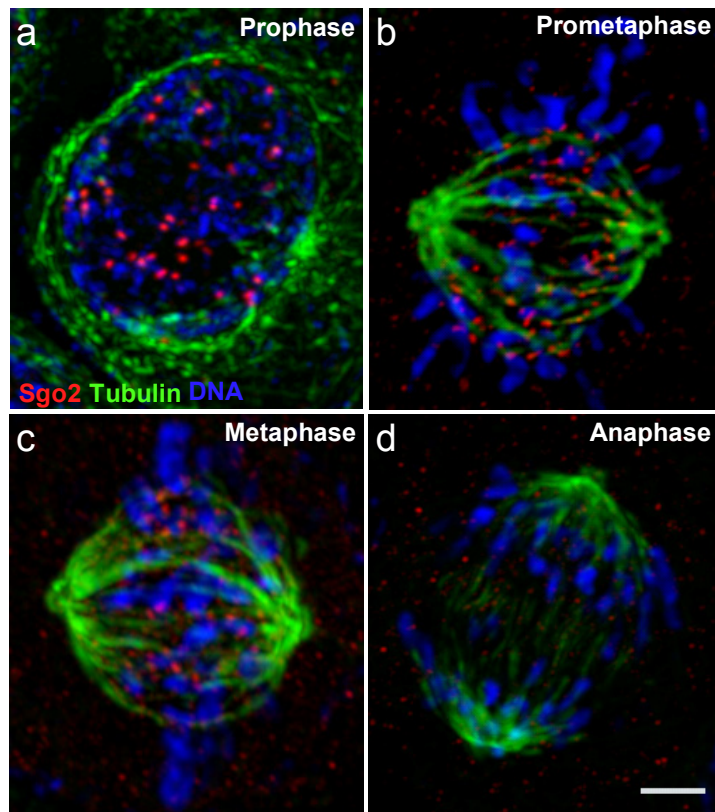
Figure 43 **Sgo2 localization through-out the cell cycle.** Micrographs of anti-Sgo2 (red) localization during pro- (**a**), prometa- (**b**), meta- (**c**), and anaphase (**d**) in HeLa cells. Upon onset of mitosis, Sgo2 binds to kinetochores until the onset of anaphase. Microtubules are green, DNA is blue. Images are maximum projection of z-stacks of deconvolved spinning disc confocal optical sections every 0.267µm through the entire spindle. Scale bar is 3µm.
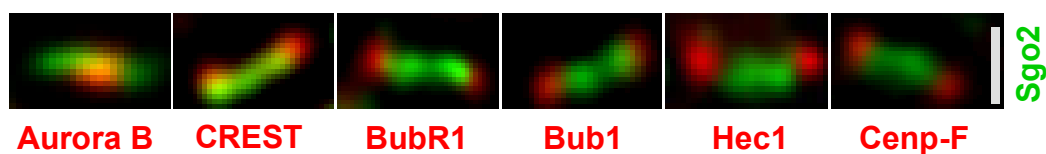
Figure 45 **Sgo2 kinetochore localization.** Micrographs of 6myc-Sgo2 (green) and Aurora B, CREST, BubR1, Bub1, Hec1, and Cenp-F (all in red) at kinetochores. Images are single deconvolved spinning disc confocal optical sections. Scale bar is 1µm.

7.9 Depletion of Sgo2 by siRNA

To examine Sgo2 function *in vivo*, Sgo2 was depleted from HeLa cells by siRNA transfection. SMARTpool™ Sgo2 siRNA was obtained from Dharmacom, which is guaranteed to be Sgo2-specific and to reduce expression by at least

75%. To test the efficiency of Sgo2 depletion, HeLa cells were transfected with Sgo2 siRNA and Sgo2 expression was analyzed 30 hours after transfection by Western blotting. As a control for experimental conditions and effects of siRNA transfection, control cells were transfected with a point-mutated Sgo2 siRNA that should not show any effect on expression of Sgo2. To be able to compare protein expression in control and Sgo2-depleted samples, lysates from equal number of cells were loaded onto the gel and blotted for Sgo2 expression. Afterwards, the blot was stripped and re-probed with an antibody against actin to confirm equal loading.

While Sgo2 protein was detectable in lysates from control siRNA transfected cells, it was absent in lysates of cells transfected with Sgo2 siRNA indicating that the Sgo2 siRNA very efficiently reduces Sgo2 expression to undetectable levels (Fig. 46). Sgo2 protein was also undetectable by immunofluorescence in Sgo2-depleted cells, while control transfected cells showed kinetochore staining. Because the polyclonal Sgo2 antibody detects Sgo2 protein with higher affinity by Western blotting than by immunofluorescence, analysis of Sgo2 expression after siRNA transfection by Western blotting is more reliable.
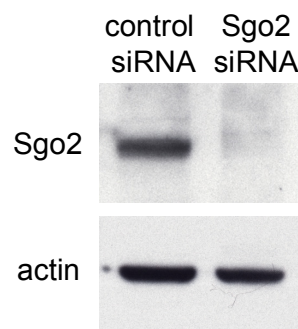
Figure 46 **Efficiency of Sgo2 depletion by siRNA.** Lysates of HeLa cells transfected with control and Sgo2 siRNA were blotted for Sgo2 and actin expression.

7.10 Sgo2 depletion induced mitotic arrest in HeLa cells

To investigate the effects of Sgo2 depletion by live-imaging *in vivo*, HeLa cells stably expressing GFP-histone 2B (HeLa^{GfpH2B} cells) were transfected with Sgo2 siRNA. 24 hours after siRNA transfection, live-imaging of the cells was started and cells were imaged for the next 36 hours (Fig. 47).

HeLa GFP-Histone 2B
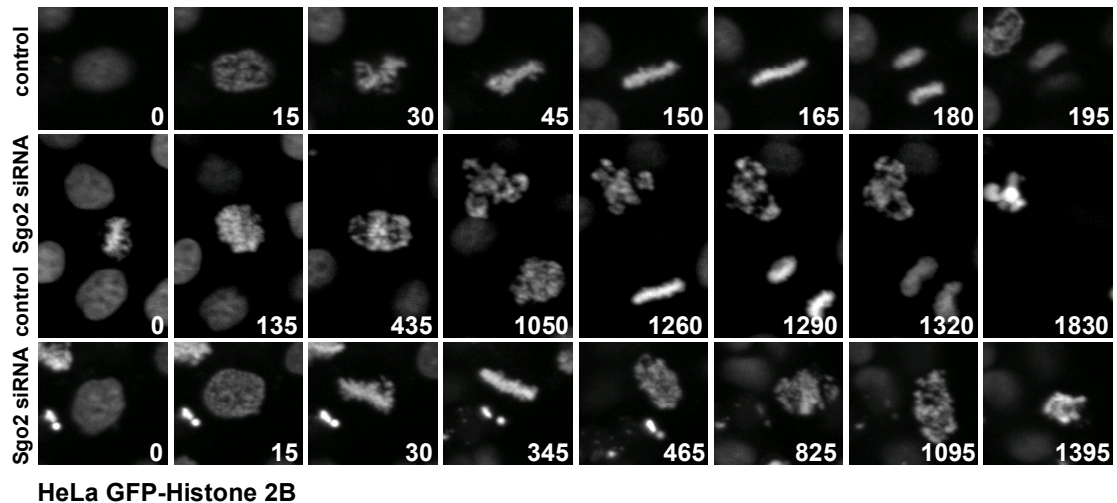
Figure 47 **Live-imaging of Sgo2 siRNA transfected HeLa^{GfpH2B} cells.** Non-transfected HeLa^{GfpH2B} cells or HeLa^{GfpH2B} transfected with control siRNA rapidly advance though mitosis, while those transfected with Sgo2 siRNA arrest in mitosis and die. Live-imaging was performed by time-lapsed spinning-disk confocal fluorescence microscopy. Time is indicated in each frame in minutes. Z-series were collected every 15 min. For each time point, 12 focal planes were collected using a 1 μm step size. Maximum z-projections of all focal planes are shown.

Unlike untransfected HeLa^{GfpH2B} cells or HeLa^{GfpH2B} cells transfected with control siRNA, which rapidly advance through mitosis, Sgo2 siRNA-transfected HeLa^{GfpH2B} cells underwent aborted chromosome congression followed by a long phase of mitotic arrest in which their chromosomes were dispersed. Finally, the cells died as judged by hypercondensed chromatin aggregates.

To further analyze the effect of Sgo2 depletion on cell cycle progression, HeLa cells were transfected with Sgo2 siRNA. 30 hours after transfection, these cells were analyzed by propidium iodide staining and FACS for cell cycle progression (Fig. 48a). The FACS profile of Sgo2-depleted cells was compared to profiles of cells transfected with control siRNA and Sgo1 siRNA [134]. While control siRNA transfected cells showed a normal cell cycle distribution with 62.7% in G1/S, 18% in G2/M, and only 2.3% in the sub-G1 population, Sgo1-depleted cells display a strong increase in the G2/M (31.9%) and sub-G1 (10.1%) population (Fig. 48b). This phenotype correlates with published observations that cells transfected with Sgo1 siRNA arrest in mitosis with defects in chromosome alignment and sister chromatid cohesion and eventually exit mitosis and die [134]. Sgo2-depleted cells also showed an increase in the G2/M fraction to

27.3% and in the sub-G1 to 7.9%, which corresponds to the mitotic arrest followed by cell death observed by live-imaging (Fig. 48b).

	sub-G1	G1/S	G2/M
Control	2.3%	62.7%	18%
Sgo1 siRNA	10.1%	38.8%	31.9%
Sgo2 siRNA	7.9%	46.6%	27.3%
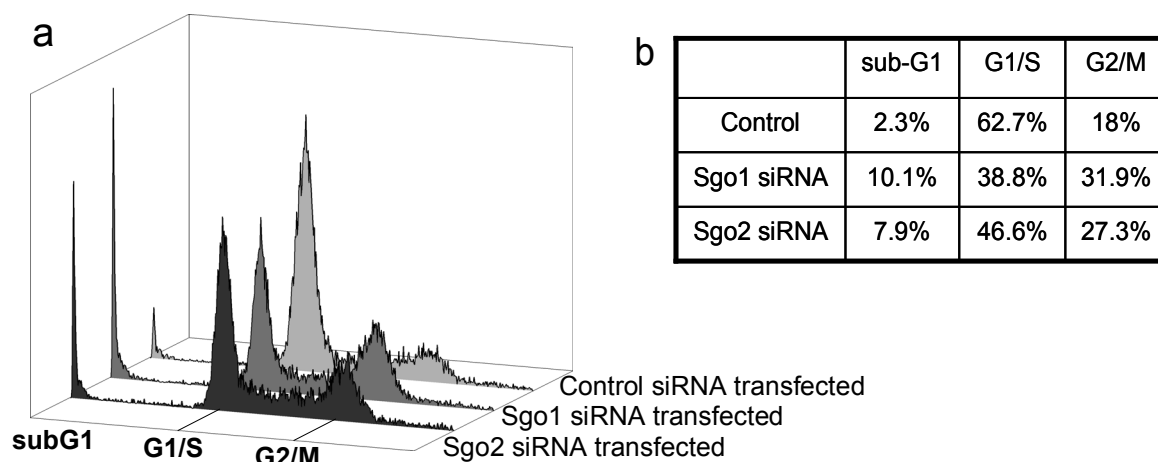
Figure 48 **FACS analysis of control, Sgo1, and Sgo2 siRNA transfected HeLa cells. a.** FACS profile of DNA content of Sgo1 and Sgo2 siRNA transfected HeLa cells indicate mitotic arrest and increase cell death. **b.** Table denoting percentage of cells with sub-G1, G1/S, and G2/M DNA content.

7.11   Chromosome mis-alignment and tension defects in Sgo2 siRNA cells

The mitotic arrest phenotype in HeLa cells upon depletion of Sgo2 was examined in greater detail by high-resolution imaging. HeLa cells were transfected with control and Sgo2 siRNA and 30 hours later stained with anti-tubulin and CREST antibodies. While in control siRNA-transfected cells chromosomes aligned at the metaphase plate with bipolar attached sister kinetochore (standard deviation of the angles of the axis through kinetochore pairs to the spindle axis was 8.7 degrees, n=153 pairs), chromosomes in Sgo2-depleted cells did not align but showed a scattered distribution (standard deviation of 56.7 degrees, n=194 pairs) (Fig. 49).

Furthermore, the mitotic spindle was elongated in Sgo2-depleted cells and the spindle pole-to-pole distance was increased to 16.2μm (min 13.04 μm, max 22.1 μm, n=29 cells) compared to 11.4μm in control cells (min 9.47 μm, max 13.16 μm, n=13 cells) (Fig. 50a). Normally, upon congression of chromosomes at the
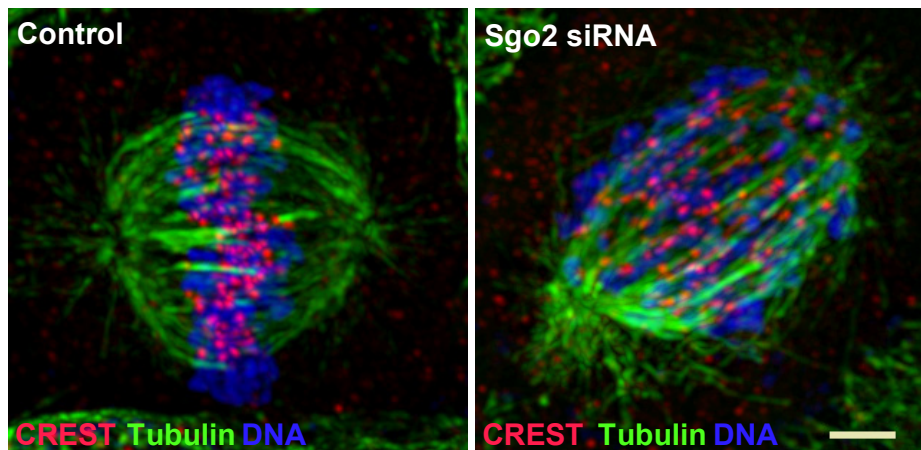
Figure 49 **Depletion of Sgo2 causes chromosome mis-alignment and loss of tension.**
Immunofluorescence micrographs of mitotic HeLa cells transfected with control (**a**) and Sgo2 siRNAs (**b**) for 30 hours. Chromosomes are stained with TO-PRO-3 iodide (blue), tubulin with anti-tubulin antibodies (green), and kinetochores with CREST antibodies (red). In control cells, chromosomes align at the metaphase plate, while Sgo2-depleted cells arrest in mitosis with unaligned chromosomes. The images shown are maximum z projections of deconvolved spinning disc confocal optical sections every 0.267µM through the entire spindle. Scale bar is 3µm.

metaphase plate, the mitotic spindle adopts a spherical shape because of various forces that are applied on the chromosomes. On the one hand, poleward flux of the microtubules lattice [157] and kinetochore poleward motion [158] pull chromosomes poleward, while on the other hand kinetochore movement away from the pole [158] and astral microtubule ejection forces [159] push chromosomes towards the metaphase plate. Because sister kinetochores are connected by centromeric chromatin, the results of these opposing forces is net tension between sister kinetochores upon bipolar attachment and congression. In a metaphase cell, all forces are balanced, resulting in a compression of the mitotic spindle to a spherical shape, minimization of the spindle pole distance, and stretching of the centromeric chromatin between sister kinetochores. Therefore an elongated spindle is commonly regarded as a sign of loss of tension between sister kinetochores.

To confirm that the increase in spindle length in Sgo2-depleted cells is a result of loss of tension, the distance between CREST foci in Sgo2-depleted and control HeLa cells was measured. While in control cells the distance between paired kinetochores was on average of 1.59µm (min 1.12µm, max 2.12µm,

n=153 pairs), in Sgo2-depleted cells this distance was markedly reduced (average 0.97µm (min 0.598µm, max 1.65µm, n=194 pairs)) (Fig. 50b). Together with the increased spindle length, the reduction in inter-kinetochore distances in Sgo2-depleted cells was consistent with a loss of tension across the kinetochore typically due to defects in microtubule attachment or kinetochore structure [157-159].
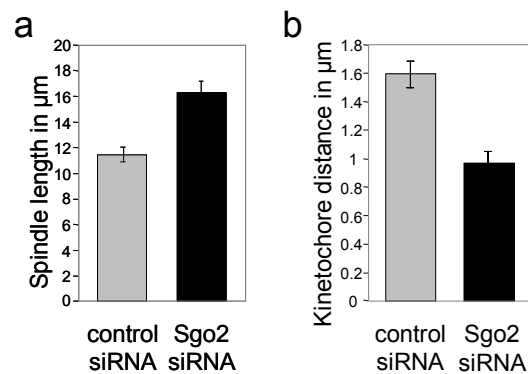
Figure 50 **Spindle length and kinetochore distance in Sgo2-depleted cells.** Histograms of spindle length (**a**) measured in 13 control and 29 Sgo2-depleted cells and distance between sister kinetochores (**b**) measured in 153 kinetochore pairs in control cells and 194 pairs in Sgo2-depleted cells. Error bars in d and e show standard deviation.

7.12   Microtubule attachment defects in Sgo2 siRNA cells

To assess whether the loss of tension in Sgo2-depleted cells was due to lack of or unstable microtubule attachment, HeLa cells were transfected with control and Sgo2 siRNA and extracted with high calcium to remove all non-kinetochore microtubules. Calcium treatment depolymerizes all non-kinetochore microtubules as well as non-attached kinetochore-microtubules, leaving only correct and stably attached kinetochore-microtubules behind. Calcium extracted cells were fixed and stained with anti-tubulin and CREST antibodies. In both control and Sgo2 siRNA transfected cells, the mitotic spindle was intact after calcium treatment suggesting that microtubules stably attach to kinetochores in Sgo2-depleted cells (Fig. 51). However, Sgo2-depleted cells displayed a large number of syntelically-attached chromosomes (5.3 per cell) and an increase in monotelically-attached chromosomes (1.1 per cell). As expected, control siRNA treated cells showed predominantly bipolar microtubule attachments and no detectable syntelic attachments. While monotelic attachment occurs in early

mitotic cells, syntelic attachment is extremely rare in mitotic cells and is generally a property of meiosis [160, 161]. If syntelic attachment occurs, it is immediately detected by the spindle assembly checkpoint and removed by Aurora B kinase. To further investigate the increase in syntelic attachment and because BubR1 is implicated in the regulation of Aurora B kinase activity, Aurora B kinase activity at kinetochore in control and Sgo2 siRNA cells was determined. Therefore control and Sgo2-depleted cells were stained with an antibody against phosphorylated Serine 7 of Cenp-A, an Aurora B kinase target. Comparison of the averaged fluorescence intensity, however, did not reveal a significant difference between control and Sgo2 siRNA, suggesting that Aurora B kinase activity is not altered in Sgo2-depleted cells.
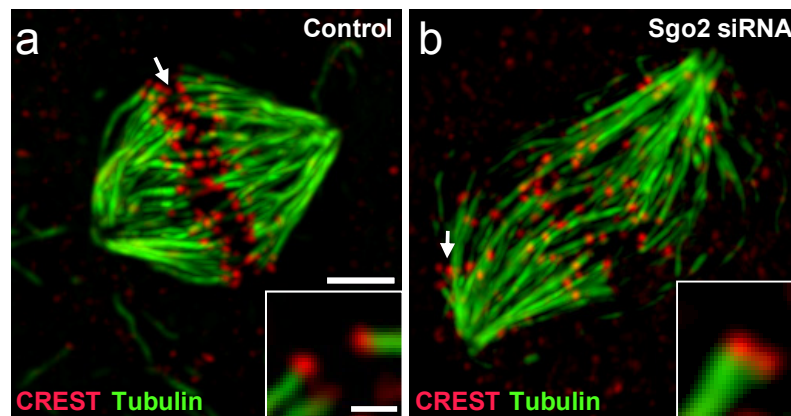
Figure 51 **Mis-attachment in Sgo2-depleted cells.**   Immunofluorescence micrographs of control (**a**) and Sgo2-depleted (**b**) mitotic HeLa cells 30 hours after siRNA transfection. Before fixation, non-kinetochore microtubules were depolymerized by calcium treatment. Tubulin is stained with anti-tubulin antibodies (green) and kinetochores are revealed with CREST auto-antibodies (red). Inset in (**a**) shows bipolar kinetochore-microtubule attachment and syntelic attachment in (**b**). Locations of the insets are indicated by arrows. All images are maximum z-projections of deconvolved spinning disc confocal optical sections every 0.267μm through the entire spindle. Scale bar is 3μm.

Since kinetochore-microtubules appear intact in Sgo2-depleted cells, the observed reduction in tension could be a consequence of mis-attachment rather than a lack of attachment.

To directly test if kinetochores are attached to microtubules after Sgo2 siRNA transfection, cells were stained with an anti-Mad2 antibody. Mad2 is a marker for microtubule attachment and its localization to kinetochores is reduced

or lost upon microtubule attachment to the kinetochore. Upon microtubule attachment, Mad2 leaves the kinetochore. While Mad2 staining was readily detectable in control transfected prometaphase cells in which chromosomes were not fully attached and or aligned (Fig. 52a), Mad2 was absent from kinetochores in control metaphase cells that had reached congression (Fig. 52b). Although chromosomes are not aligned in Sgo2 siRNA cells, no Mad2 stain was detectable, confirming that kinetochores are attached to microtubules and that a lack of attachment is not the cause of the loss of tension in Sgo2-depleted cells (Fig. 52c and d).
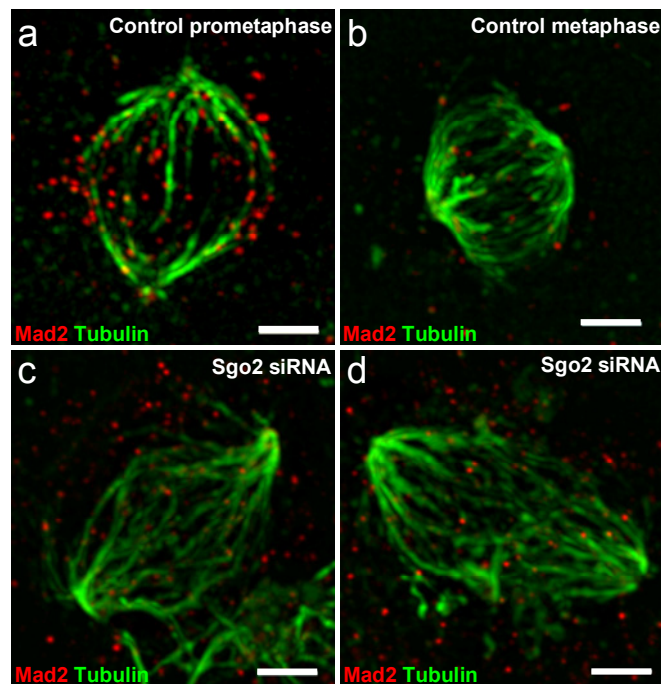
Figure 52 **Mad2 staining in Sgo2-depleted cells.** Micrographs of anti-Mad2 (red) and anti-tubulin (green) immunofluorescence in control (**a,b**) and Sgo2-depleted (**c,d**) cells. All images are maximum z-projections of deconvolved spinning disc confocal optical sections every 0.267µm through the entire spindle. Scale bar is 3µm.

7.13 Sister chromatid cohesion in Sgo2 siRNA cells

Because Sgo2's paralog Sgo1 is required for maintenance of centromeric cohesion in yeast and mammals, it is possible that Sgo2 is also involved in this process and that loss or weakening of centromeric cohesion is the underlying cause for the loss of tension. Therefore, Sgo2- and control depleted cells were

stained with CREST antiserum and an antibody to the outer kinetochore protein, Hec1. In the case of intact centromeric cohesion, Hec1 stain would be on either side of CREST stain, while upon loss of cohesion only one Hec1 focus would be next to CREST.

When control and Sgo2-depleted cells were analyzed at 30 hours for the status of centromeric cohesion, all kinetochores in control cells (Fig. 53a) and 98.8% of all kinetochores in Sgo2-depleted cells (Fig. 53b) were paired, indicating that centromeric cohesion is intact in the absence of Sgo2. However, 48 hours after transfection, sister kinetochores are largely separated in Sgo2-depleted cells as indicated by an unpaired distribution of Hec1/CREST focus (Fig. 53c), while in control cells kinetochores were still paired (data not shown).
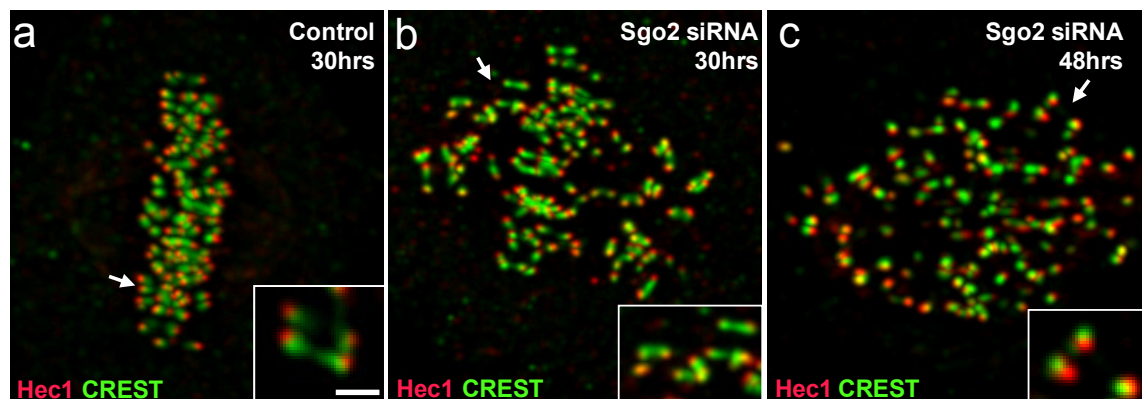
Figure 53 **Centromeric cohesion in Sgo2-depleted cells.** Immunofluorescence micrographs of control and Sgo2-depleted mitotic HeLa cells stained with antibodies to Hec1 (red) and CREST (green) to assess the status of cohesion between sister kinetochores after 30 hours (**a,b**) and 48 hours (**c**) after siRNA transfection. Insets shown cohesion between sister kinetochore in control and Sgo2 siRNA transfected cells 30 hours after transfection and loss of cohesion 48 hours after Sgo2 siRNA transfection. Images are maximum projection of z-stacks of deconvolved spinning disc confocal optical sections every 0.267μm through the entire spindle. Scale bar is 3μm. Insets are single spinning disc confocal optical sections. Scale bar is 1μm.

7.14   Distortions in the inter-kinetochore of Sgo2-depleted cells

Although centromeric cohesion is intact in Sgo2-depleted cells 30 hours after siRNA transfection, the inter-kinetochore axis between two sister kinetochores frequently displayed distortions (147 axial distortions in 43 Sgo2-deficient cells) (Fig. 54), a phenomenon that was not evident in control cells (2 in

28 control cells). These distortions often, but not exclusively, occurred in chromosomes that were positioned around the spindle poles where syntelically-attached chromosomes often cluster.
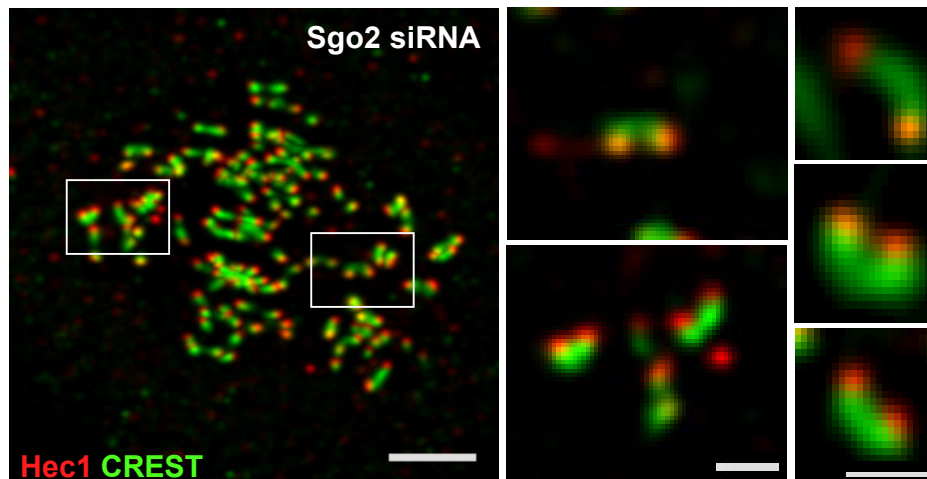
Figure 54 **Distortion in the inter-kinetochore axis of Sgo2-depleted cells.**
Immunofluorescence micrographs of Sgo2-depleted mitotic HeLa cells stained with antibodies to Hec1 (red) and CREST (green). Insets show high magnification of marked regions. Micrographs on the right display distortions of the inter-kinetochore axes of chromosomes from Sgo2-depleted cell. Image on the left is a maximum z projection of deconvolved spinning disc confocal optical sections every 0.267μM through the entire spindle. Scale bar is 3μM. Insets and micrographs on the right are single planes. Scale bar is 1μM.

To determine if the distortions are due to syntelic attachment and independent of Sgo2 depletion, syntelically-attached chromosomes were experimentally induced in wild type cells. To do this, HeLa cells were treated with monastrol, a drug that induces monopolar spindles by inhibiting the Eg5 kinesin and spindle pole separation, for 2 hours [162]. Afterwards, monastrol was washed out and the cells were treated with Aurora B kinase inhibitor to prevent correction of mis-attachment, and with the proteasome inhibitor MG132 to prevent cells from exiting mitosis [163]. In a monopolar spindle most chromosomes display monotelic attachment and removal of monastrol leads to spindle pole separation and formation of a bipolar spindle. If Aurora B kinase is inhibited, mis-attachment cannot be corrected and syntelic attachment occurs with increased frequency.
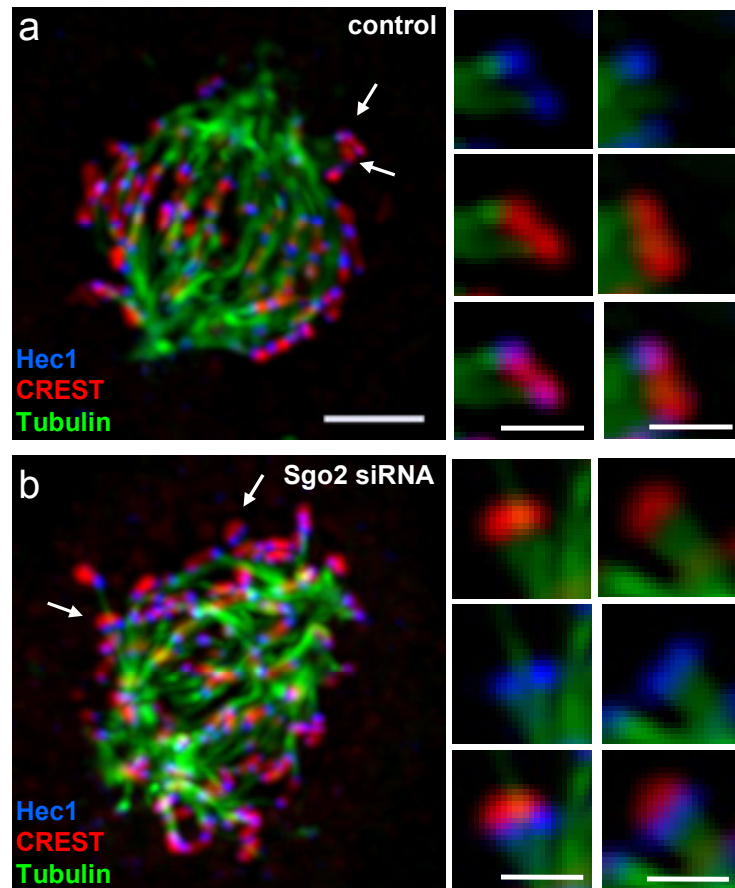
Figure 55 **Syntelic Chromosomes in Control and Sgo2-depleted Cells.** Immunofluorescence micrographs of control (**a**) and Sgo2-depleted (**b**) mitotic HeLa cells. Cells are stained with antibodies against Hec1 (blue), CREST (red), and tubulin (green). Panels on the left show magnification of syntelically-attached chromosomes in control and Sgo2-depleted cells. Images are maximum z-projections of deconvolved spinning disc confocal optical sections every 0.267µm through the entire spindle. Scale bar is 3µm. Magnifications of the right are deconvolved single spinning disc confocal optical sections. Scale bar is 1µm.

After monastrol wash-out, wild type cells rapidly formed a bipolar spindle with most chromosomes aligned at the metaphase plate and only a few remaining syntelically-attached at the spindle poles (Fig. 55a). The inter-kinetochore axis of the syntelically-attached chromosome appeared straight with Hec1 and CREST staining being aligned in the same plane. In Sgo2-depleted cells, however, many chromosomes did not congress at the metaphase plate (Fig. 55b). Analysis of syntelic chromosomes showed that the inter-kinetochore axis of many but not all syntelically-attached chromosomes was distorted with Hec1 and CREST staining not being aligned.

Although syntelic attachment *per se* is not responsible for inter-kinetochore distortions, it is possible that the loss of Sgo2 alone is not sufficient to induce inter-kinetochore axial distortions and that an additional stress like microtubule attachment is necessary. To determine the overall relationship between microtubule attachment and inter-kinetochore axial distortions, control and Sgo2-depleted cells were treated with nocodazole, a microtubule-depolymerizing drug. High amounts of nocodazole efficiently remove all microtubules including attached kinetochore-microtubules.
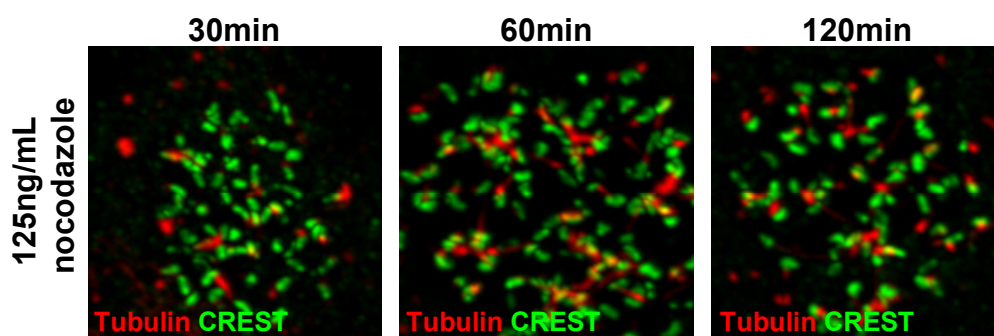
Figure 56   **Effects of nocodazole treatment on the mitotic spindle.** Immunofluorescence micrographs of mitotic HeLa cells treated with 125ng/mL of nocodazole for 30, 60 or 120 min and stained with antibodies against CREST (green) and tubulin (red). Images are maximum z-projections of deconvolved spinning disc confocal optical sections every 0.267µm through the entire spindle.

The concentration of nocodazole and time of treatment necessary to depolymerize all microtubules in HeLa cells was titrated and depolymerization was confirmed by staining with anti-tubulin antibodies. Exposure of HeLa cells to a nocodazole concentration of 125ng/mL for 30 min was determined to be sufficient to depolymerize all kinetochore- and non-kinetochore-microtubules (Fig. 56).

To determine if inter-kinetochore axial distortions are influenced by microtubules, HeLa cells were transfected with control and Sgo2 siRNA and after 30 hours treated with 125ng/mL nocodazole for 30 min. Depolymerization of all microtubules had a general effect on the inter-kinetochore structure in control siRNA transfected cells. In about 48.8% of all sister kinetochores were connected by a straight axis, 23.6% had a curved appearance, the remaining 27.6% were too compressed to be judged (Fig. 57a and b). In Sgo2-deficient

cells, the number of curved axes was increased to about a third of the total number (Fig 57c and d), but none of these curved axes approached the severe distortions seen in the Sgo2-deficient cells *in vivo*.

Kinetochore morphology	Compressed	Straight	Curved
Control siRNA (n=680)	27.6%	48.8%	23.6%
Sgo2 siRNA (n=525)	25.7%	40.6%	33.7%
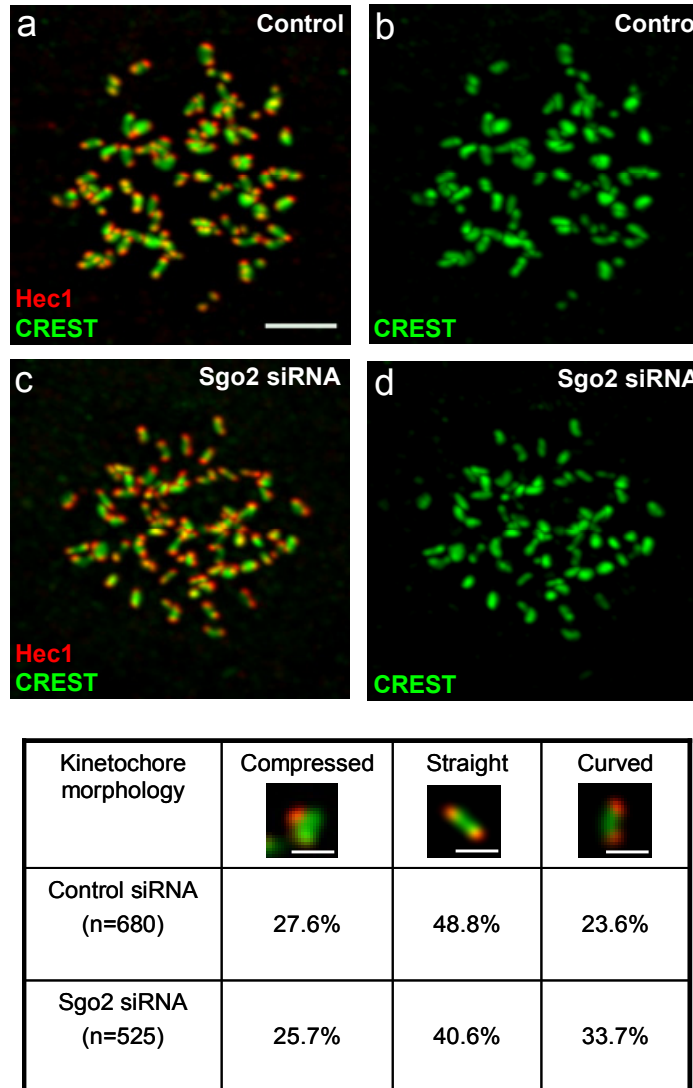
Figure 57 **Effects of nocodazole on kinetochore structure in control and Sgo2 siRNA transfected cells.** Immunofluorescence micrographs of mitotic HeLa cells transfected with control (**a,b**) and Sgo2 siRNA (**c,d**) 30 hours after transfection. Cells were treated with 125 ng/mL nocodazole for 30 min and stained with antibodies against CREST (green) and Hec1 (red). Kinetochores were visually scored for their appearance in three categories (compressed, straight, and curved). Images are maximum z projections of deconvolved spinning disc confocal optical sections every 0.267µm through the entire spindle. Scale bar is 3µm. Images in the table are deconvolved single spinning disc confocal optical sections. Scale bar is 1µm.

7.15 Kinetochore-microtubule interactions in a monopolar spindle

As an additional test of the effects of Sgo2 depletion on inter-kinetochore axial rigidity and thereby kinetochore-microtubule interactions, kinetochore-microtubule interaction in a monopolar spindle upon Sgo2 depletion were investigated by analyzing the Mad2 distribution.

Monopolar spindles were generated by exposing control and Sgo2 siRNA transfected HeLa cells to the Eg5 inhibitor monastrol. In accordance with published results [162, 164], treatment of control siRNA transfected HeLa cells with monastrol generated monopolar spindles with radial-arranged chromosomes that displayed little or no Mad2 staining of the kinetochore nearest the pole and strong Mad2 staining on the sister kinetochore facing away from the pole (Fig. 58a and b).
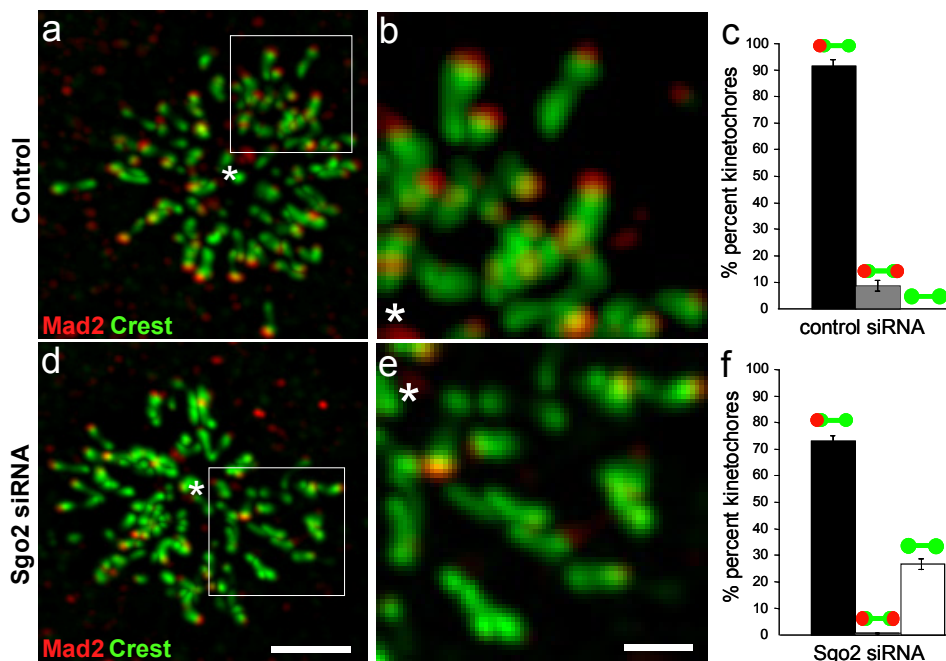
Figure 58 **Kinetochore-microtubule interactions in a monopolar spindle.** Micrographs of control (**a,b**) and Sgo2-depleted (**c,d**) cells treated with monastrol and stained with antibodies to Mad2 (red) and CREST antibodies (green). Origins of the resulting monopolar spindle are denoted with an asterisk. Images on the right are magnifications of the boxed regions. All images are maximum z projections of deconvolved spinning disc confocal optical sections every 0.267µm through the entire spindle. Scale bar in images on the left is 3µm and in magnifications 1µm. Histograms on the left displays quantification of Mad2 staining patterns among sister kinetochores in Eg5-inhibited mitotic HeLa cells transfected with control (**c**) or Sgo2 siRNAs (**f**). Error bars show standard deviation.

As Mad2 intensity at kinetochores is inversely proportional to the number of attached microtubules, this bimodal distribution of Mad2 staining of sister kinetochores suggests that chromosomes attach in a monopolar fashion to microtubules.

Monopolar spindles also formed in Sgo2-depleted cells after monastrol treatment. However, the majority of chromosomes showed little or no staining of Mad2 on either sister kinetochore (Fig. 58d and e). Visual scoring of Mad2 staining on kinetochores that were, in addition, labeled with CREST antibodies found that in control cells, 91% of all sister kinetochores (n=219) had one Mad2-positive kinetochore, while those in Sgo2-depleted cells (n=219) showed only 73% of sister kinetochores with a single Mad2 focus. The percentage of kinetochore pairs with two Mad2-positive foci was 8.7% in control cells and 0.41% in Sgo2-depleted cells. Strikingly, the percentage of Mad2-negative kinetochores was increased from 0% to 26.7% in Sgo2-depleted cells, suggesting an overall increase in microtubule attachment (Fig. 58c and f).
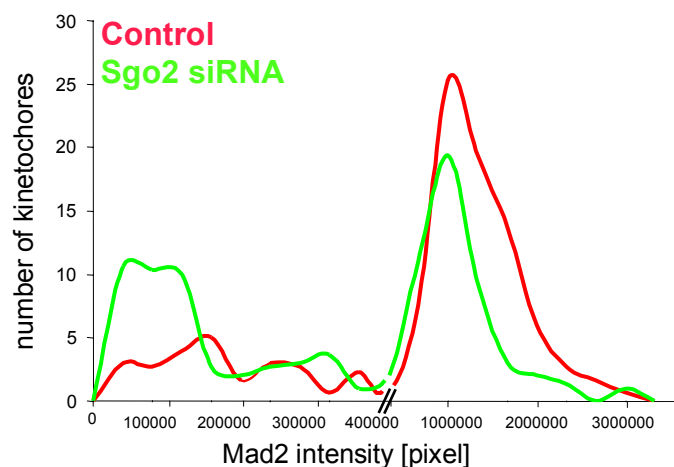
Figure 59 **Quantification of Mad2 staining intensity in a monopolar spindle.** Graphical presentation of distribution of Mad2 pixel intensity in control (red) and Sgo2-depleted (green) HeLa cells.

To quantitatively measure the decrease in Mad2 staining in Sgo2-depleted cells, the pixel intensity of the Mad2 staining at the kinetochores of control and Sgo2-depleted cells was determined and yielded an overall shift to lower intensity values (Fig. 59).

7.16 Microtubule dependent re-localization of Sgo2

To further investigate Sgo2's physical association with microtubules, a microtubule pelleting assay was performed. HeLa cells were arrested in mitosis with Taxol, lysed and cellular tubulin was polymerized with Taxol in the presence of ATP or AMP-PNP (a non-hydrolysable analogue of ATP). Polymerized tubulin was pelleted by high-speed centrifugation. Microtubule pelleting in the presence of ATP leads to co-sedimentation of conventional microtubule binding proteins, while the addition of AMP-PNP induced rigor binding of microtubule associates motor proteins and pelleting of both motor and conventional microtubule binding proteins. The initial lysate, pellet, as well as supernatant after pelleting, were analyzed by Western blot for Sgo2 binding. After pelleting of microtubules, Sgo2 was only found in the pellet and not in the supernatant, suggesting that most Sgo2 is in fact bound to tubulin (Fig. 56).
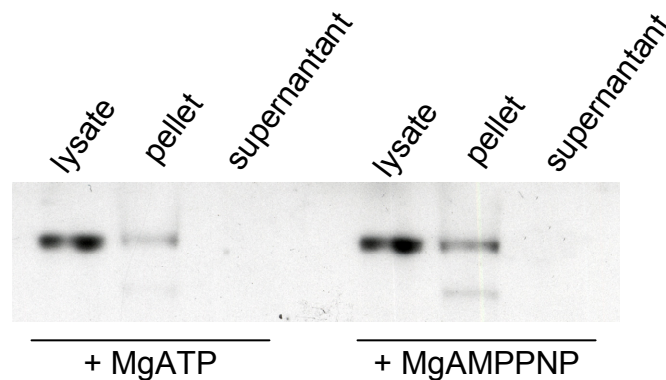
Figure 60 **Western blot of Sgo2 on sample from tubulin pelleting assay.** Western blot of endogenous Sgo2 protein before pelleting (lysate), and after in pellet and supernatant with ATP or AMPPNP. Same amount of lysate before and after pelleting are loaded (lane: lysate and supernatant).

After determining that Sgo2 interacts with microtubules by co-precipitation and in the microtubule pelleting assay, the localization of Sgo2 under different microtubule attachment conditions was analyzed. Upon depolymerization of tubulin by nocodazole, Sgo2's distribution along the inter-kinetochore axis appeared radically altered. Rather than having an axial distribution as seen in prometaphase and metaphase cells, Sgo2 localized as a single focus to the inner centromere (Fig. 61b). The same type of localization behavior of Sgo2 was found very early in prophase before nuclear envelope breakdown and

microtubule attachment (Fig. 61a). To assess if the axial distribution of Sgo2 in prometa- and metaphase was induced by microtubule attachment or tension across kinetochores, HeLa cells were treated with Taxol to specifically abrogate tension across the kinetochores without disturbing microtubule attachment. Under this condition, Sgo2 displayed the same axial distribution as in metaphase (Fig. 61c and d).
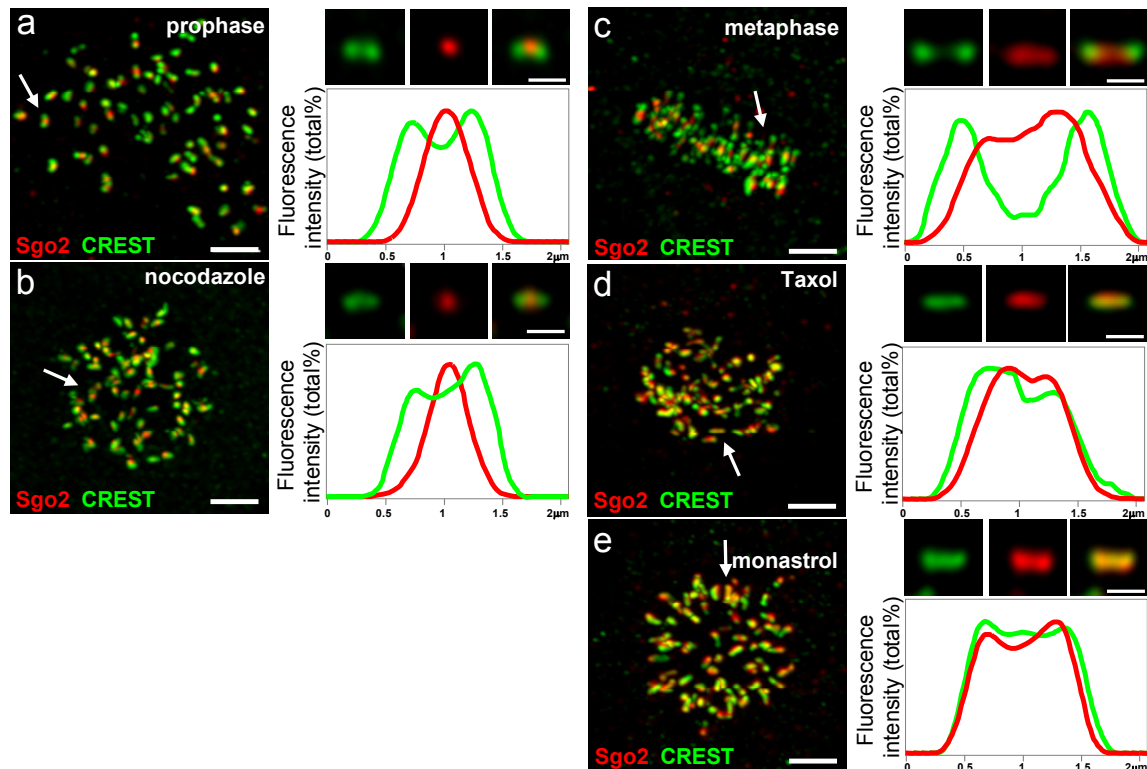
Figure 61 **Sgo2 Localization Under Different Attachment Conditions.** Immunofluorescense micrographs of cells stably transduced with a 6myc-Sgo2 retrovirus. Cells shown are treated with nocodazole (**b**), Taxol (**d**), monastrol (**e**) to create different kinetochore-microtubule attachment conditions or untreated in different cell cycle stages (prophase (**a**), metaphase(**c**)). Cells are stained with anti-myc antibody (red) and CREST auto-antibody (green). Next to each micrograph, one representative kinetochore is enlarged to show the relative position of Sgo2 and CREST. Line scans compare the distribution of the relative fluorescence intensity of Sgo2 (red) and CREST (green) across the sister kinetochores. Images are maximum z projections of deconvolved spinning disc confocal optical sections every 0.267μm through the entire spindle. Scale bar is 3μm. Images of single kinetochores are deconvolved single spinning disc confocal optical sections. Scale bar is 1μm.

The mechanism for kinetochore orientation based on a rigid inter-kinetochore axis by Oestergren hypothesizes that the attachment of the first kinetochore orients the second to the opposite pole [95]. To determine if Sgo2 responds to this initial attachment event, Sgo2 localization upon monopolar attachment was analyzed by treatment of HeLa cells with monastrol. Significantly microtubule attachment to one sister kinetochore induced the spreading of Sgo2 from the inner centromere to the inner kinetochore covering an area overlapping with CREST staining (Fig. 57e).

Taken together, these data indicate that in the absence of microtubule attachment, there is a general loss of the axial structure of the inner kinetochore, and this loss of structure correlates with the redistribution of Sgo2 from an axial pattern to the inner centromere. Furthermore, monopolar attachment of microtubules to one kinetochore was sufficient to redistribute Sgo2 along the inter-kinetochore axis, confirming that attachment and not tension induces Sgo2 relocalization.

7.17   Interaction of BubR1-Sgo2

To elucidate the significance of the BubR1-Sgo2 interaction, the inter-dependency of their kinetochore localization was investigated. Later, HeLa cells were transfected with targeting control, Sgo2, or BubR1 siRNA for 30 hours, fixed and stained with antibodies against BubR1 and Sgo2.

After 30 hours, Sgo2 expression in Sgo2 siRNA transfected cells was reduced to undetectable levels. However, BubR1 was still detectable at kinetochores, suggesting that Sgo2 is not required for kinetochore localization of BubR1 (Fig. 62a and b). In the reverse experiment, BubR1 was depleted from HeLa cells by siRNA, leading to a checkpoint override and early exit from mitosis even under conditions of checkpoint activation. To arrest BubR1 siRNA transfected cells in mitosis, cells were treated with MG132 proteasome inhibitor two hours before fixation and stained with an anti-Sgo2 antibody. After BubR1 depletion, Sgo2 fluorescence at kinetochores was strongly reduced but not abolished due to incomplete BubR1 depletion (Fig. 60c and d). Because BubR1 is highly expressed, it is difficult to completely deplete cells of BubR1 and quantification showed that after siRNA transfection, BubR1 expression is only

reduced to about 20%. Nevertheless, the results suggest that kinetochore binding of Sgo2 is dependent on BubR1.
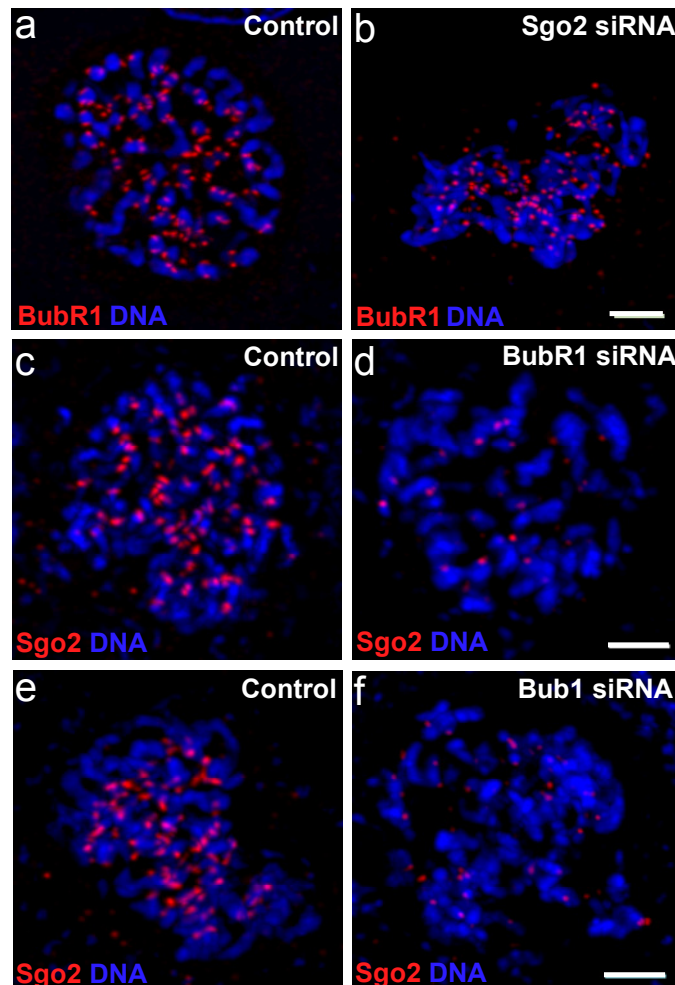
Figure 62 **Interdependency of BubR1, Bub1 and Sgo2 Localization.** Immunofluorescence micrographs of control (**a**) and Sgo2-depleted (**b**) mitotic HeLa cells stained with anti-BubR1 antibodies (red). Immunofluorescence micrographs of control (**c**,**e**) and BubR1- (**d**) or Bub1- (**f**) depleted mitotic HeLa cells stained with anti-Sgo2 antibodies (red). DNA is stained with TO-PRO-3 iodide (blue). Images are maximum z-projections of deconvolved spinning disc confocal optical sections every 0.267μm through the entire spindle. Scale bar is 3μm.

In yeast, Sgo2 localization to kinetochores requires the checkpoint protein Bub1. To determine if that is also the case in mammalian cells, Bub1 was depleted by siRNA and cells stained with anti-Sgo2 antibody (Fig. 60 e and f). Like yeast, mammalian Sgo2 depends on Bub1 for kinetochore localization.

8. Discussion

In meiosis and mitosis, the equal distribution of sister chromatids to daughter cells is crucial and therefore monitored by a sophisticated surveillance mechanism, termed the spindle assembly checkpoint. If errors occur during chromatid segregation, daughter cells with aberrant chromosome numbers will accrue, leading to chromosomal instability, developmental defects, and possibly cancer. Moreover, chromosome mis-segregation during meiosis and early stages of development often result in miscarriage or severe developmental defects [165]. To avoid these errors, the spindle assembly checkpoint has to function with extremely high fidelity in every cell division [93]. Since its initial description 15 years ago, the number of proteins involved in spindle assembly checkpoint signaling is constantly increasing and an even more complex protein interaction network has begun to emerge.

8.1 Expression and post-translation modifications of BubR1

BubR1 is constitutively expressed throughout the cell cycle. During mitosis and mitotic arrest, BubR1 becomes phosphorylated and localizes to kinetochores. To investigate the connection between posttranslational modifications and the subcellular localization of BubR1, the protein was subjected to mass spectrometry based phosphorylation profiling and validated by mutagenesis.

Quantification of BubR1's phosphorylation status in interphase and under mitotic arrest revealed that BubR1 is specifically phosphorylated on certain residues during mitosis. Moreover, a region (amino acid 670-689) in BubR1 was identified whose phosphorylation mediated the subcellular localization and possibly the function of BubR1 upon anaphase onset. Even though site-specific point mutations in BubR1 did not affect BubR1 localization and migration behavior in Western blots, deletion of this cluster region did. Furthermore, Aurora B kinase was determined to be the regulating kinase responsible for phosphorylation of the cluster region (amino acid 670-689) of BubR1. This observation correlates with findings in *Saccharomyces cerevisiae* that implicate homologs of Aurora B and Polo-like kinase in Mad3 phosphorylation [166]. Furthermore, Aurora B kinase activity has been previously shown to be at least

partially regulated by BubR1 [118], suggesting that functional or physical interaction between both protein is essential for their function in spindle assembly checkpoint signaling.

8.2   Evolution of protein function by post-translational modifications?

The early departure of BubR1-Δ670-689 upon congression is reminiscent of the localization behavior of another checkpoint protein, Bub1. In mammals, both proteins show extensive sequence homology, but they differ in the duration of their kinetochore localization. While deletion of the cluster region (amino acid 670-689) of BubR1 leads to its Bub1-like departure from the kinetochore upon congression, addition of this region to N-Bub1 permits it to remain bound beyond anaphase onset.

Comparison of the sequence homology of human Bub1 and BubR1 shows that both proteins are more similar to each other than to their yeast homologs. Yeast Bub1 and Mad3, the yeast homolog of BubR1, also display a high degree of homology to each other, although the kinase domain of Bub1 is absent in Mad3. It is likely that both genes evolved by gene duplication from a common ancestral gene and acquired independent functions in checkpoint signaling by changes in the primary amino acid sequence and the post-translational modification pattern. The loss of the Bub1-like kinase domain in yeast Mad3 over time could be due to the simpler structure of kinetochore and mitotic machinery in yeast that requires a less extensive checkpoint mechanism for error detection and correction. For instance, in budding yeast a single microtubule attaches to each kinetochore making biorientation largely, if not completely, dependent on tension and not kinetochore geometry [122]. With increasing complexity of the mitotic process during evolution, the kinase-dependent and – independent functions of the Mad3 C-terminus might have become essential for the integrity of the spindle assembly checkpoint leading to its conservation.

Importantly, no role for yeast Mad3 beyond the checkpoint has been established. However, BubR1 is localized to kinetochore after anaphase onset, a process that is dependent on BubR1's C-terminal domain that is lost in yeast Mad3. It is therefore possible that BubR1's post-checkpoint functions are

determined by this region. A role for yeast Mad3 beyond checkpoint signaling is unknown.

8.3   Sgo2 is a novel BubR1 interacting protein

One of the newly identified mitosis-specific, BubR1-interacting proteins is Sgo2. Because of its implication in yeast kinetochore biology and checkpoint signaling [112], Sgo2 was a desirable candidate for further investigation.

From early prophase until congression, Sgo2 localizes to the inner kinetochore. Depletion of Sgo2 by siRNA leads to a strong mitotic arrest followed by cell death (Fig. 46 and 47). The observed arrest is likely due to activation of the spindle assembly checkpoint by lack of tension between sister kinetochores (Fig. 49 and 49). This is supported by the observation that ablation of the spindle assembly checkpoint in Sgo2 siRNA cells by expression of N-Bub1 [103] or treatment with Aurora kinase inhibitor [146] abolishes the arrest (data not shown). After an extended period of time in mitotic arrest, loss of cohesion was observed in Sgo2-depleted cells (Fig. 52) implicating Sgo2 in the protection of centromeric cohesion. However, the loss of cohesion occurs late and could therefore be a secondary effect. Recently, Sgo2 was reported to be required for centromeric localization of PP2A in mammalian cells [131, 136, 147]. Furthermore, PP2A was implicated in the protection of centromeric cohesion [131, 136, 147]. Given that several PP2A subunits were identified as Sgo2-interacting proteins (Table 3), it is possible that the observed loss of cohesion in Sgo2-depleted cells is secondary to loss of PP2A at centromeres.

While kinetochore-microtubule attachment was intact after Sgo2 depletion, a strong increase in syntelic and a minor increase in monotelic attachment were observed (Fig. 50 and 51). Normally, monotelic attachment is seen early in mitosis after nuclear envelope breakdown when microtubules begin to invade the nuclear space. However, as mitosis progresses, chromosomes become bipolarly attached. Syntelic attachment, on the other hand, is rarely seen in mitotic cells, because it is immediately detected by the spindle assembly checkpoint and removed by Aurora B kinase. Despite Aurora B kinase function being intact, it appears that the increase in syntelic attachment in Sgo2-depleted cells may be beyond the capacity of an Aurora B-mediated correction mechanism. However,

no changes in Aurora B kinase activity were observed, suggesting that upon depletion of Sgo2 the frequency of syntelic attachment was increased over the capacity of Aurora B kinase to correct it.

Moreover, the dependency of Sgo2 kinetochore localization on Bub1 and BubR1 expression was investigated (Fig. 62). As in yeast [112], depletion of Bub1 by siRNA resulted in loss of Sgo2 from kinetochores. Furthermore, down-regulation of BubR1 expression also reduced the levels of Sgo2 at kinetochores, while depletion of Sgo2 from HeLa cells had no effect on BubR1 localization. Although both Bub1 and BubR1 are required for Sgo2 localization, it appears that they mediate this function by different mechanisms. BubR1 seems to mediate Sgo2 localization by physical and possible functional interaction, as indicated by the interaction studies, while Bub1's function in Sgo2 localization is solely indirect.

8.4   Sgo2's function in maintenance of a rigid kinetochore structure

Closer examination of the kinetochore structure of Sgo2-depleted cells revealed distortions of the inter-kinetochore axis, especially in chromosomes clustered around the spindle poles (Fig. 53). Because syntelic chromosomes often reside around the spindle poles, the interdependency of both phenomena was investigated. However, when syntelic attachment was induced in wild type cells, the inter-kinetochore axis was straight, while in Sgo2-depleted cells syntelic attached chromosomes often, but not always, showed distortions (Fig. 54). Thus the distortions in Sgo2-deficient kinetochores are not the product of syntelic attachment *per se*, but more likely the consequence of a particular condition of the inter-kinetochore axis due to the depletion of Sgo2. One explanation for the inter-kinetochore axial distortions in the Sgo2-depleted cells is that they reflect a loss of the rigid, back-to-back orientation of sister kinetochores that, upon monotelic binding, actively positions the sister kinetochore to the opposite spindle pole to enhance bipolar attachment and reduce the incidence of syntelic attachments.

Furthermore, under conditions of Aurora B kinase inhibition, chromosomes in Sgo2-depleted cells did not congress during recovery from monastrol arrest, while wild type cells achieved bipolar attachment (Fig. 54), possibly due to

increased syntelic microtubule attachment. It is likely that in the presence of Sgo2, inter-kinetochore rigidity leads to the orientation of the unattached kinetochore away from this spindle pole and thereby shields it from further microtubule attachment to that pole. However, if Sgo2 is depleted, the inter-kinetochore axis exhibits greater flexibility and the unattached kinetochore can be captured by microtubules emanating from the same spindle pole.

Because not every chromosome in Sgo2-depleted cells shows distortions, it is possible that loss of Sgo2 only weakens the inter-kinetochore structure and that forces applied to kinetochores by microtubules are necessary to induce distortions. Investigation of the kinetochore structure in control- and Sgo2 siRNA transfected cells treated with nocodazole revealed that under non-attachment conditions, even in wild type cells the inter-kinetochore axis of 23.6% of all kinetochores is not straight but curved (Fig. 56). Taken together, these experiments suggest that the severe distortions of the inter-kinetochore axis seen in the Sgo2-deficient cells are likely due to forces imparted by microtubules through syntelic or merotelic attachment, possibly coupled to interactions of non-kinetochore microtubules emanating from the poles. Sgo2 could be required for inducing rigidity into the kinetochore axis upon kinetochore-microtubule attachment that orients the unattached kinetochore away the pole from which the microtubule originated.

The findings of Sgo2's interaction with tubulin and the modulation of its localization by microtubule attachment status suggest that Sgo2's function in kinetochore rigidity could be microtubule-dependant. Moreover, mammalian Sgo1 was discovered in a screen for factors that stimulate microtubule formation [134]. Thus a close relationship between initial microtubule attachment, Sgo2 localization, and rigidity status of the inter-kinetochore axis is emerging.

The lack of inter-kinetochore rigidity in Sgo2-depleted cells, its loss in the absence of microtubule attachment even in wild type cells, and the observed relocalization phenotype of Sgo2 upon attachment point to a role of Sgo2 in mediating inter-kinetochore rigidity upon microtubule attachment. In the absence of microtubule attachment, the inter-kinetochore axis is quite flexible, possibly in order to favor an initial microtubule attachment. After this initial attachment, the axis becomes more rigid and distortions or curvature are no longer observed. At this point, Sgo2 spreads from localizing to a single focus to an axial distribution

and thereby possibly induces rigidity that protects the unattached kinetochore from becoming syntelically-attached. Accordingly, in the absence of Sgo2, a high flexibility of the inter-kinetochore axis persists, leading to increased attachment and thereby mis-attachment in both a bipolar and monopolar spindle. The more severe phenotype seen in monopolar spindles is probably due to a denser spatial distribution of microtubules and a higher number of unattached kinetochores. In control cells, the unattached kinetochore is aligned with the attached kinetochore and the kinetochore-microtubules and thereby shielded from syntelic attachment. However, in Sgo2 cells the unattached kinetochore can diverge from this alignment and be captured by other microtubules.

This proposed function of Sgo2 in determining the rigidity of the inter-kinetochore axis is consistent with a model of kinetochore geometry introduced by Oestergren over 50 years ago [95]. This model suggested that, after initial attachment of microtubules to one sister kinetochore, the rigid back-to-back orientation of sister kinetochores orients the unattached kinetochore to the opposite pole and thereby reduces the risk of syntelic attachment. While in *Saccharomyces cerevisiae* such a mechanism is not necessary, because only one microtubule attaches to each kinetochore, in higher organisms, each kinetochore is captured by many microtubules. Thus, kinetochore geometry is an additional and necessary mechanism to obviate attachment errors and mis-segregation. The findings presented in this work are consistent with Sgo2 playing an essential role in this process.

9. Materials

9.1 Reagents

All standard chemicals were obtained from Sigma.

$^{13}C_6$-arginine	Cambridge Isotope Labs
$^{13}C_6{}^{15}N_2$-lysine	Cambridge Isotope Labs
4',6-Diamidino-2-phenylindole dihydrochloride (DAPI)	Sigma
$^{32}P\alpha$dCTP	ICN
Affi-Gel 10	Bio-Rad
APS	Bio-Rad
Aurora B kinasae	Gift from Bedrick Gadea
Aurora B kinase inhibitor ZM447439	Gift from Tim Mitchison
Benchmark Protein Ladder Prestained	Invitrogen
Benchmark Protein Ladder	Invitrogen
Bisacrylamid	National Diagnostics
BL21 competent bacteria	Novagen
Bovine serum albumin (BSA)	Sigma
Complete mini EDTA-free protease inhibitors	Roche
Coomassie Brillant Blue R250	Sigma
DAB detection kit	Vector
Desoxynucleosid-5'-triphosphate (dNTPs) for PCR	Roche
DH5α competent bacteria	ATCC
Dimethyl pimelimidate (DMP)	Pierce
DMSO	Sigma
Dulbecco's modified Eagle's medium (DMEM)	Invitrogen
Dulbecco's modified Eagle's medium (SILAC)	Invitrogen
Ethidium Bromide	Bio-Rad
Fetal bovine serum (FBS)	Hyclone
Fetal bovine serum (dialyzed)	Hyclone
Fetal bovine serum (ES grade)	Hyclone
FIAU	Moravek Biochemicals
Fisetin	Sigma
Formaldehyde 37%	Sigma
G418	Invitrogen
Gelatin	Sigma
Glutathione Sepharose 4 Fast Flow	Amersham Bioscience
Glycerophosphate	Sigma
Hematoxylin	Fischer
HEPES sodium salt	Sigma
Lambda phosphatase	NEB
LB	Harvard Medical School
LB agarose plates	Harvard Medical School
Leukemia inhibitory factor (LIF)	Chemicon
MG132	Calbiochem
MgAMPPNP	Sigma
MgATP	Sigma
MgGTP	Sigma
Mirus293	Mirus

MOPS buffer	Invitrogen
Nocodazole	Sigma
Non-fat dry milk powder	Stop&Shop
Novex gels	Invitrogen
Oligofectamine	Invitrogen
Oligonucleotide-primers	IDT
Opti-MEM I	Invitrogen
P10 resin	BioRad
pBluescript-SK(-)	Stratagene
PEG1500	Roche
Penicillin-streptomycin (100U/ml and 100μg/ml)	Invitrogen
pGEX4T3	Amersham Bioscience
Polybrene	Sigma
Primary antibodies:	
Aurora B	Abcam
Bub1	ImmunQuest
Cenp-F	Bethyl Laboratories
CREST	ImmunoVision
Cytokeratin	Abcam
Hec1	GeneTex
Keratin 5	Covance
Keratin 8	Troma I, Hybridoma bank, University of Iowa
Loricrin	Covance
Tubulin	Sigma
Mad2	Abcam
Propidium iodide	Sigma
Proteinase K	Roche
Protein G-Sepharose	Amersham Bioscience
Puromycin	Sigma
pZero vector	Invitrogen
Restriction enzymes	NEB
RNase A	Roche
Seakem LE agarose	Biozym
SDS, 20%	Bio-Rad
Secondary antibodies:	
Anti-mouse HRP	Jackson Laboratory
Anti-rabbit HRP	Jackson Laboratory
Anti-human Alexa Fluor®488	Molecular Probes
Anti-human Alexa Fluor®568	Molecular Probes
Anti-mouse Alexa Fluor®488	Molecular Probes
Anti-mouse Alexa Fluor®568	Molecular Probes
Anti-mouse Alexa Fluor®594	Molecular Probes
Anti-mouse Alexa Fluor®674	Molecular Probes
Anti-rabbit Alexa Fluor®488	Molecular Probes
Anti-rabbit Alexa Fluor®568	Molecular Probes
Anti-rabbit Alexa Fluor®594	Molecular Probes
Anti-rabbit Alexa Fluor®647	Molecular Probes
Anti-rat Alexa Fluor®488	Molecular Probes
Sepharose4B	Amersham Bioscience

Sgo2 siRNA (SmartPool)	Dharmacom
Silencer siRNA construction kit	Ambion
SOC media	Gibco
Sodium fluoride	Sigma
Sodium molybdate	Sigma
Sodium pyrophosphate	Sigma
Sodium tartrate	Sigma
Sodium vanadate	Sigma
SuperSignal West Pico substrate kit	Pierce
Taxol	Sigma
TEMED	Bio-Rad
Tetracycline	Sigma
Thymidine	Sigma
TO-PRO-3 iodide	Molecular Probes
Triton-X100	Sigma
Trypsin-EDTA	Invitrogen
Tween20	Bio-Rad

9.2   Materials

Coverslips	VWR
Centricon	Millipore
Electroporation cuvettes	Bio-Rad
Gel blotting paper	VWR
Hybond N+ nitrocellulose membrane	Amersham Bioscience
Hyperfilm ECL	Amersham Bioscience
Nitrocellulose membrane	BioRad

9.3   Kits

Expand High Fidelity PCR System	Roche
Expand Long Template PCR System	Roche
HiSpeed Plasmid Maxi Kit	Qiagen
QIAprep Spin Miniprep Kit	Qiagen
QIAquick Gel Extraction Kit	Qiagen
QIAquick PCR Purification Kit	Qiagen
QuikChange® Site-Directed Mutagenesis Kit	Stratagene
RadPrime labeling kit	Invitrogen
Restriction enzymes	New England Biolabs
Silencer siRNA Construction Kit	Ambion
T4-DNA-ligase	New England Biolabs

9.4   Instruments

Analytical balance AG204	Mettler
Axiocam HRcm	Zeiss
Axioskop mot 2 plus	Zeiss
Bio-Rad Mini Gel system	Bio-Rad
Centrifuge 5415 D	Eppendorf

Centrifuge	Beckman
Dissection scope MZ6	Leica
Electrophoresis chamber MS-8210	Aladin Enterprise
Electroporation Gene Pulser	Biorad
Heatable magnetic stirrer	Corning
Heating block	VWR
Incubators	Forma Scientific Inc.
Kodak T-MAX developer	Kodak
Light microscope TE100	Nikon
NuPAGE Novex Gel system	Invitrogen
PCR Express	Hybaid
pH-meter 140	Corning
Phosphor-Imager	BioRad
Phosphor-Imager screen	BioRad
Power supply Power Pac 200	BioRad
Rotor SW28	Beckman
Semi-dry transfer cell	Biorad
Shaking incubators	Forma Scientific Inc.
SmartSpec™3000	BioRad
Sonifier B12 Branson	Sonic Power Company
Spinning disk confocal	Perkin Elmer
TE2000U inverted microscope	Nikon
UV-box	VWR
Vortexer Vortex Genie 2	Scientific Industries
Water treatment system Milli-Q	Millipore
Waterbath	Precision

9.5   Software

AutoDeBlur deconvolution	Media Cybernetics
MetaMorph software	Molecular Devices

9.6   Buffers

Alkaline buffer	0.4M NaOH
	1.5M NaCl
BRB80 buffer	80mM PIPES pH 6.8
	1mM MgCl2
	1mM EGTA
Coommassie brilliant blue solution	0.1% (w/v) Coomassie R250
	40% Methanol
	10% Acetic acid
Cross-linking buffer	50mM Na-HEPES pH6.8

Denhardts (100x)	2% BSA (Sigma Fraction V) 2% Ficol 2% Polyvinylpyrrolidone 3x SSPE buffer
Destaining solution	40% Methanol 10% Acetic acid
Electroporation buffer	20mM HEPES pH7.0 137mM NaCl 5mM KCl 0.7mM Na_2HPO_4 6mM glucose 0.1mM beta-mercaptoethanol
HEPES saline buffer	121mM NaCl 5.4mM KCl 0.44mM KH_2PO_4 0.3 mM Na_2HPO_4 5.56 mM glucose 20mM Hepes Phenol Red 290 mmol/kg osmolarity pH 7.3
Hybridization buffer	10% Dextran sulfate 0.375 M Na_2HPO_4 0.125 M NaH_2PO_4 1X Denhardts 1% SDS
Microtubule stabilizing buffer (MTSB)	BRB80 + 4 mM EGTA
Mounting media	90% Glycerol 100mM Tris pH8
PBS	10mM NaH_2PO_4 10mM Na_2HPO_4 150mM NaCl
PBST	PBS + 0.2% TritonX-100
PHEM	60mM Pipes 25mM Hepes 10mM EGTA 4mM MgSO4
Sample buffer (2x)	100mM Tris pH6.8 1.43M beta-mercaptoethanol 4% SDS

	20% glycerol 0.7mg/ml Bromphenol blue
SDS-PAGE running buffer (10x)	1.92M Glycine 0.25M Tris pH8.3 1% SDS
SSC buffer (20x)	3M NaCl 0.3M sodium citrate pH 7.0
SSPE buffer (20x)	3M NaCl 0.2M NaH_2PO_4 20 mM EDTA pH 7.0
TAE (50x)	2M Tris-acetate 100mM EDTA
Tail/ES cell lysis buffer	100mM Tris pH8 200mM NaCl 5mM EDTA 0.2% SDS 50μg/ml Proteinase K
Taq- PCR buffer (10x)	100mM Tris pH8.3 500mM KCl 0.01% gelatine autoclave and filter
TBS (1x)	50mM Tris 150mM NaCl
TBST (1x)	1x TBS + 0.1% Tween20
TE buffer	10mM Tris pH8 1mM EDTA
Transfer buffer (10x)	1.92M Glycine 0.25M Tris pH8.3

10.   Methods

10.1   Molecular biology methods

10.1.1 Polymerase Chain Reaction (PCR)

Reactions were performed in 50μl volume using the Expand Long Template or Expand High Fidelity PCR system from Roche according to according to manufacturer's instructions.

10.1.2 PCR purification and gel extraction

PCR purification and gel extraction were performed using the Qiagen QIAquick PCR Purification Kit and QIAquick Gel Extraction Kit according to manufacturer's instructions.

10.1.3 Restriction enzyme digest

Restriction enzymes were purchased from New England Biolabs (NEB). Enzyme concentration and buffer conditions were used as suggested by the manufacturer. Circular plasmid DNA was digested for 1hr at the recommended temperature. PCR products were usually digested overnight at the recommended temperature.

10.1.4 Ligation of DNA fragment

For ligation of DNA fragment, T4-DNA-ligase was purchased from NEB. Ligation reactions were performed in a 10μl volume containing 1μl 10x T4-Ligase buffer, 1μl digested backbone, 7μl digested insert, and 1μl T4-DNA-ligase. The reaction was incubated overnight at 16°C and transformed the next day into bacteria.

10.1.5 Cloning

After PCR amplification of the gene of interest with gene-specific primers containing overhanging ends with restriction enzyme recognition sequences, the PCR product was purified and digested with the appropriate restriction enzymes. The vector backbone was also digested with restriction enzymes. Backbone and PCR products were separated by agarose gel electrophoresis and extracted from

the gel. PCR product and backbone were ligated, the ligation mix was transformed into bacteria, and plated onto LB agarose plates. After overnight incubation at 37°C, colonies were picked, and grown in liquid culture overnight. The next day, plasmid DNA was purified and analyzed by restriction digest for insertion of the PCR product into the vector backbone.

10.1.6   Transformation of bacteria

For transformation competent bacteria (DH5α or BL21) were incubated with circular plasmid DNA or ligation mixtures for 30 min on ice, heat-shocked for 1 min at 42°C, recovered on ice for 2 min, and plated onto LB-Agar plates with appropriate antibiotics. When ligation mixtures were transformed, the bacteria were grown for 1hr at 37°C in SOC media before plating. The LB-Agar plates were incubated overnight at 37°C.

10.1.7 Plasmid DNA preparation from bacteria

Plasmid DNA was prepared from bacteria using QIAprep Spin Miniprep Kit or HiSpeed Plasmid Maxi Kit from Qiagen according to manufacturer's instructions.

10.1.8 Mutagenesis

Mutagenesis was carried out using the QuikChange® Site-Directed Mutagenesis Kit from Stratagene according to manufacturer's instructions. Mutations were verified by DNA sequencing.

10.1.9 DNA sequencing

DNA sequencing was performed by the Dana-Farber/Harvard Cancer Center DNA Resource Core. Plasmid DNA and primers were submitted at the suggested concentration and volume.

10.1.10 SDS-PAGE

Discontinuous, denaturing SDS-polyacrylamid-gelelectrophoresis was performed using the Bio-Rad Mini Gel system or NuPAGE Novex Gel system from Invitrogen [166-168].

For the Bio-Rad Mini Gel system, gels were poured with 4% stacking. The percentage of the resolving gel was chosen according to the size of the protein of interest. For the NuPAGE Novex Gel system, 4-12% BisTris gels were purchased.

Resolving gel	8.5%	10%	12%	15%
H_2O	4.6ml	4ml	3.4ml	2.4ml
1.5M Tris/HCl pH 8.8	2.5ml	2.5ml	2.5ml	2.5ml
30% Acrylamide	3ml	3.35ml	4ml	5ml
10% SDS	0.1ml	0.1ml	0.1ml	0.1ml
10% APS	0.1ml	0.1ml	0.1ml	0.1ml
TEMED	0.01ml	0.01ml	0.01ml	0.01ml

Stacking gel	4%
H_2O	6.2ml
0.5M Tris/HCl pH 6.8	2.5ml
30% Acrylamide	1.1ml
10% SDS	0.1ml
10% APS	0.1ml
TEMED	0.01ml

Protein samples were mixed 1:1 with 2x sample buffer, incubated for 10 min at 100°C, and spun down for 1 min at 13000rpm. Bio-Rad Mini Gels were run in home-made 1x SDS-PAGE buffer, NuPAGE Novex Gel were run in 1x MOPS buffer (Invitrogen). Proteins were separated at constant voltage (100V for Bio-Rad Mini Gel, 200V for NuPAGE Novex Gel).

10.1.11 Coomassie brilliant blue staining

After SDS-PAGE gel electrophoresis, the gel was placed in Coommassie brilliant blue solution and incubated for 1hr at room temperature, with rocking. The staining solution was then exchanged against de-stain solution and further incubated for about 3hr at room temperature, with rocking. To completely clear

the background, the gel was further incubated in 8% acetic acid overnight at room temperature, with rocking.

10.1.12 Western Blot

For immuno-detection, proteins were transferred to a nitrocellulose membrane using a wet-blot method [169]. For the transfer, a sandwich was assembled consisting of a pad, two pieces of Whatman paper, gel, nitrocellulose membrane, two pieces of Whatman paper, and another pad. The sandwich was placed into the transfer apparatus with the membrane facing the anode and the proteins were transferred at constant 100V for 1hr at room temperature. When the transfer was completed, the membrane was removed from the sandwich, rinsed with 1x TBS, and blocked for at least 30 min in 5% milk in TBST. After blocking, the membrane was incubated with primary antibody diluted in 5% milk in TBST for 1hr at room temperature or overnight at 4°C. The membrane was washed 3x15 min with TBST and incubated with secondary antibody for 1hr at room temperature. After washing 3x1 min with TBST, it was quickly rinsed with water before proceeding to chemiluminescence. For chemiluminescence, the SuperSignal West Pico substrate kit from Pierce was used. Equal amounts of both solutions were mixed and placed on the membrane for 1 min. The membrane was placed inside a sheet protector, bubbles and excess liquid was removed, and the membrane was exposed to an X-ray film. The film was developed in Kodak T-MAX developer.

10.1.13 Immunohistochemistry

Immunohistochemistry was performed on paraffin slides prepared by the Rodent Histopathology Core of the Harvard Medical School. Before staining, section were deparaffinized by sectional incubation in xylene (4x 3 min), 100% ethanol (2x 2 min), 95% ethanol (2x2 min), and stored in PBS. To reveal the antigen, sections were placed in 10mM citrate buffer pH6.0 and microwaved at constant temperature (199F) for 30 min. Afterwards, slides were cooled down in citrate buffer and transferred to PBS. Sections were blocked with 1% BSA in PBS for 30 min at room temperature, incubated with primary antibody in 1% BSA in PBS overnight at 4°C and washed twice for 5 min with PBST. For

immunofluorescence detection, sections were incubated with fluorescent labeled secondary antibody in 1% BSA in PBS for 1hr at room temperature. DNA was stained by DAPI for 1 min at room temperature before slides were mounted and nail-polished for long-term storage. For DAB detection, sections were incubated with biotinylated secondary antibody for 1hr at room temperature, washed twice with PBS, incubated with Vectorstain Elite ABC reagent for 5 min, and developed with peroxidase substrate solution for 2- 10min. Sections were counterstained with Hematoxylin, mounted and nail-polished for long-term storage.

10.1.14 Immunoprecipitation

For immunoprecipitation cells were collected and lysed in 150mM NaCl, 50mM Tris pH7.2, 1mM $MgCl_2$, 0.5% Triton-X100 with protease inhibitors (Roche) and phosphatase inhibitors (1mM glycerophosphate, 1mM sodium pyrophosphate, 1mM sodium vanadate, 1mM sodium fluoride, 1.15mM sodium molybdate, 4mM sodium tartrate). The lysate was cleared by centrifugation for 30 min at 20,000xg and 4°C. For pre-clearing, Sepharose4B was added to the lyaste and incubated for 3 hours with rotation at 4°C. The lysate was centrifuged again for 5 min at 1,000xg at 4°C and transferred to a new tube. Antibody chemically-crosslinked to protein G-Sepharose or protein G-Sepharose was added to the lysate for overnight incubation with rotation 4°C. Sepharose beads were collected by gravity and washed three times with lysis buffer and twice with PBS. Proteins were eluted in sample buffer at 95°C and resolved by SDS-PAGE gel electrophoresis. After staining with Coomassie blue, the gel was trypsin digested and analyzed by microcapillary reverse-phase liquid chromatography– hybrid ion trap/Fourier transform ion cyclotron resonance mass spectrometry by Dr. Scott Gerber.

10.1.15 Immunofluorescence

For immunofluorescence staining, HeLa cells were plated on 12mm coverslips and grown overnight. The next day the media was aspirated and cells were fixed with 3% formaldehyde in PBS for 7 min at room temperature. After fixation, cells were washed four times with PBST (PBS/0.1% Triton-X100) and blocked with 3% milk or 1% BSA in PBST for 30 min at room temperature. Cells

were incubated with primary antibody for 1hr at room temperature, followed by washing three times with PBST and incubation with secondary antibody for 30 min at room temperature. The cells were three times washed with PBST and DNA stained with Hoechst 33258 diluted in PBST to 1μg/ml or for confocal imaging with TO-PRO-3 iodide (Molecular Probes) for 1 min at room temperature.

 Afterwards, cells were washed with PBST and coverslips were mounted onto microscope slides and sealed with nail polish. For Aurora B, Bub1, BubR1, Cenp-F, CREST, Hec1, Sgo2 and tubulin staining, cells were extracted for 30sec with microtubule stabilizing buffer (MTSB) + 0.5% TritonX-100 before fixation and fixed with 3% formaldehyde. For Mad2 staining cells were lysed in PHEM + 0.5% Triton X-100 for 5 min and then fixed in 1% formaldehyde for 20 min. For calcium depolymerization of microtubules, $CaCl_2$ was added to a final concentration of 5mM to MTSB + 0.5% TritonX-100 or PHEM + 0.5% TritonX-100 for 5 min before fixation.

10.1.16 Microscopy

        All images were collected as Z-stacks with 0.267μm spacing using a 100X, 1,35NA objective on a Nikon TE2000U inverted microscope with spinning disk confocal (Perkin Elmer) and processed using AutoDeBlur deconvolution and MetaMorph software. To determine the number of paired and single kinetochores, cells were stained with CREST autoimmune serum and the anti-Hec1 antibody. Z-stacks though the entire spindle were collected and deconvolved. For spindle length and kinetochore distance measurements, cells were stained with CREST and tubulin antibodies. Spindle length was determined on maximal intensity projections of z-stacks. Kinetochore distance was measured on single planes. Mad2 intensity was measured in a circular area of fixed size though all planes of the kinetochore, each plane was background-subtracted and values added together. Values up to 400,000 were binned every 10,000 pixels, while values above 400,000 were binned every 100,000 pixels. The moving average over three neighboring bins was calculated for graphical display. P63 intensity was measured in a circular area of fixed size in every cell, background-subtracted, and values were averaged.

10.1.17 Lambda phosphatase treatment

Dephosphorylation of all serine, threonine, and tyrosine residues was carried out by addition of lambda-phosphatase to lysates. 50µl of lysates were supplemented with 2mM $MnCl_2$ and 400 units of lambda phosphatase and incubated at 30°C for 30 min.

10.1.18 Antigen preparation

Using sequence specific primers with overhanging ends containing restriction enzyme recognition sites, four regions of approximately 800 to 900bp of the BubR1 and Sgo2 cDNA were amplified cloned into the pGEX-4T3 vector for bacterial expression of GST-fusion proteins. By sequencing, confirmed clones were transformed into BL21 bacteria. For protein expression, bacteria were grown in liquid culture in LB medium at 37°C until OD_{600} reached 0.5 to 0.6. At that point IPTG was added to a final concentration of 1mM and bacteria were incubated at 37°C for three more hours. Afterwards, bacteria were collected by centrifugation and lysed in 2X sample buffer. Lysed proteins were resolved by SDS-PAGE gel electrophoresis and revealed by Coomassie blue staining. The gel was destained, equilibrated in deionized water to remove acetic acid and methanol, and ground into fine particles. Gel particles were resuspended in PBS and used for mice injection.

10.1.19 Antibody purification

For purification of polyclonal antibodies, GST-fused antigens used for immunization against Sgo2 were purified using Glutathione Sepharose 4 Fast Flow resin. After binding of bacterial expressed GST-tagged Sgo2 antigens to the resin for 3 hours at 4°C with rotation, it was washed three times (50mM Tris pH8, 100mM NaCl, 1mM EDTA). The recombinant protein was eluted from the resin using 10mM reduced glutathione in 50mM Tris pH8 and concentrated using Centricons. Purified and concentrated antigene was coupled to Affi-Gel10 resin according to manufacturer's instructions. The serum containing the polyclonal antibody was diluted with 50mM Tris pH8 and incubated with the antigen-coupled resin overnight at 4°C rotating. The next day, the resin was washed and antibodies were eluted from the resin using glycine-HCl pH 2.5. After

neutralization, the purified antibody was dialyzed against PBS and concentrated using Centricons.

10.1.20 Cross-linking

Directed cross-linking of antibodies to ProteinG-Sepharose4B beads was performed using dimethyl pimelidate dihydrochloride (DMP). Antibody from hybridoma cell culture was adjusted to a concentration of 1mg/ml and incubated with ProteinG-Sepharose4B overnight at 4°C with rotation. Antibody-ProteinG-Sepharose4B beads were washed three times with PBS and equilibrated with 10 bed volumes cross-linking buffer (50mM Na-HEPES, pH 6.8). Beads were washed three times with 2 bed volumes DMP solution (5µg DMP/ 1ml of 300mM Na-HEPES), followed by three times incubation in DMP solution for 10 min at room temperature. The cross-linking reaction was stopped by incubating the beads with 50mM ammonium bicarbonate. Then the beads were washed once with cross-linking buffer and once with PBS and stored at 4°C.

10.1.21 *In vitro* Kinase assay

Recombinant Aurora B kinase was diluted in to a concentration of 37.5µg/ml in kinase dilution buffer (20mM HEPES-KOH pH 7.7, 50mM HCl, 1mM DTT) to make a 15X kinase stock. Histones were diluted to a final concentration of 1mg/ml in GF buffer (10mM HEPES-KOH pH 7.7, 300mM KCl, 1mM DTT). Immuno-precipitated BubR1 from 3 million cells was washed with GF buffer. For the kinase reaction 1µl kinase stock and immuno-precipitated BubR1 or 1µl histones were mixed in kinase buffer (20mM HEPES-KOH pH7.7, 5mM $MgCl_2$, 1mM EGTA, 1mM DTT, 50µM ATP, 2µCi γ-^{32}P-ATP in a total volume of 25µl. The kinase reaction was incubated at 30°C for 20 min and terminated by adding 2x Sample buffer. Proteins were resolved by SDS-PAGE gel electrophoresis and the dried gel was exposed overnight at -80°C to X-ray film.

10.1.22 Generation of TA-p63 targeting construct

For the specific deletion of TA-p63 isoforms in the mouse genome without disruption of ΔN-p63 isoform expression, a targeting construct was designed to

replace exon 2 and 3 as well as the intermediated intron with a neomycin resistance gene (Neo^r).

The targeting construct was prepared by cloning genomic p63 sequences, a positive as well as a negative selection marker into pBluescript-SK(-). For manipulation of the genomic p63 sequences, a ~15 kb long NotI-NotI fragment containing exon 2 and 3 and flanking intronic regions of p63 was subcloned from of a previously identified phage clone from a 129/SvJ genomic library into the pZero vector (Invitrogen). In the first step of cloning the targeting construct, the HSV thymidine kinase (HSV-TK) gene under the control of the MC1 promoter was cloned via SacII and NheI into the SacII and SpeI sites of pBluescript-SK(-) (Stratagene). Ligating the NheI site into the SpeI site destroyed both sites. Then the genomic p63 clone was digested with BstBI and SalI and cloned into the ClaI and SalI sites of pBluescript-SK(-)-(HSV-TK) leading to the destruction of the BstBI/CalI sites. A~2.4 kb fragment containing exon 2 and 3 and flanking regions of p63 was deleted from the construct by SpeI digest. A neomycin resistance gene (Neo^r) driven by the mouse phosphoglycerol kinase (PGK1) promoter and linked to the PGK1 poly (A) sequences with NheI sites on the 5' and 3' end was ligated into the SpeI sites of the constructs destroying the SpeI/NheI sites. After completion of cloning, the construct was sequenced to confirm that it did not contain any mutations. For electroporation, the constructed was linearized by SacII digest. The final targeting construct consists of HSV-TK gene on the 5' prime end, a 1.6kb short arm homologous to genomic DNA upstream of exon 2, the Neo^r, and a 3.7kb long arm homologous to genomic DNA downstream of exon 3.

10.1.23 Isolation of genomic DNA from ES cells

ES cells were plated onto 12-well plate without feeder cells and grown until confluency. When cells were confluent, media was removed and lysis buffer with proteinase K was added to the well and incubated overnight at 37°C. On the next day an equal volume of 100% isopropanol was added and placed on a rotating shaker until DNA precipitated. DNA threads were spooled out, washed with 70% ethanol, dissolved in 250μl TE buffer, and incubated at 55°C overnight.

10.1.24 Isolation of genomic DNA from mice tail

Mice tails were cut and incubated in lysis buffer with proteinase K overnight at 55°C.   On the next day an equal volume of 100% isopropanol was added and tubes were vortexed until DNA precipitated. DNA threads were spooled out, washed with 70% ethanol, dissolved in 250μl TE buffer, and incubated at 55°C overnight.

10.1.25 Polymerase Chain Reaction (PCR) for genotyping

Reactions were performed in 25μl volume containing 0.4μM of each primer (TAKO4,5,6), 0.1mM of each dNTP, 1.5mM $MgCl_2$, 1X PCR buffer, 15-30ng genomic DNA, and 2.5U Taq polymerase.

Following conditions were used for the PCR:

Initial denaturation	95°C	5 min	1Cycle
Denaturation	95°C	30s	
Annealing	60°C	30s	30 Cycles
Elongation	72°C	30s	
Final elongation	72°C	7 min	1 Cycle

TAKO4	ATCTAGCAGCAAGATTAACAA
TAKO5	GGGAACTTCCTGACTAGGG
TAKO 6	GCATAGTTCCTACGTTTCAC

10.1.26 Southern Blot analysis

For Southern Blot analysis genomic DNA was digested with BglII overnight at 37°C. The next day, DNA was resolved on a 0.8% agarose gel and stained with Ethidium Bromide. Gel was acid treated with 0.25N HCl for 10 min and neutralized in alkaline buffer for 10 min. DNA was transferred from the gel onto Hybond N+ membrane by capillary transfer overnight at room temperature. After transfer, the membrane was rinse in 2XSSC buffer and pre-hybridized for at least 2 hours at 65°C. Labeled probe was added and hybridized to the DNA overnight at 55°C. The membrane was washed with washing buffer three times for 15 min at 65°C and exposed to the phosphor-imager screen for 2 hours or film overnight at -80°C.

10.1.27 Random Prime labeling of Southern Blot Probe

The PCR-generated Southern Blot Probe was labeled with $^{32}P\alpha dCTP$ using a RadPrime labeling kit from Invitrogen. 25ng of DNA probe was diluted into 17μl water and mixed with 16μl 2.5x RadPrime buffer, 2.4μl 125μM dNTP's (without dCTP), and 4μl $^{32}P\alpha dCTP$ (>3000 Ci/mmol). The mixture was boiled for 90s and immediately placed on ice. When the tube was chilled, 1μl Klenow enzyme was added to the reaction and incubated for more than 30 min at room temperature. The labeling reaction was stopped by the addition of 2μl of 2%SDS.

The labeled probe was purified from unincorporated dNTP's by spin dialysis. To do this, the cap of a 0.5ml tube was cut off and using 26 gauge needle a hole was poked into the bottom of tube. Approximately 30μl of spin dialysis glass beads were added to the tube to cover the bottom and the tube was filled up to the top with P10 resin. The column was packed by centrifugation for 3 min and 15s at 3000rpm. The stopped labeling reaction was loaded onto the column and spun for 4 min at 3500rpm. The eluted probe was diluted with 300μl TE buffer, boiled for 5 min, and snap-cooled in an ice bath before addition to the membrane.

10.2   Cell biology methods

10.2.1   Cell culture

HeLa, HeLa-H2B-GFP, and NSO-1 cells were cultured in Dulbecco's modified Eagle's medium (DMEM) with 10% fetal bovine serum and penicillin-streptomycin (100U/ml and 100μg/ml), at 37°C in a humidified atmosphere with 5% CO_2.

10.2.2 SILAC

For SILAC experiments, HeLa cells were grown in arginine- and lysine-free DMEM with 10% dialyzed fetal bovine serum and penicillin-streptomycin (100U/ml and 100μg/ml) supplemented with either 50mg/l $^{13}C_6$$^{15}N_2$-and 50mg/L $^{13}C_6$-arginine (Cambridge Isotope Labs) or normal lysine and arginine for at least six cell doublings. The extent of incorporation was verified as ≥ 95% by mass spectrometric analysis of multiple peptides from several proteins of heavy-only, SDS-PAGE- fractionated whole cell lysates.

10.2.3 Cell synchronization

HeLa cells were synchronized in interphase by addition of 2mM thymidine for 18 hours. Thymidine was washed out and cells were grown in DMEM with 10% FBS for 8 hours, before they thmidine was added again for 18 hours.

For arrest in mitosis, HeLa cells were synchronized by a double thymidine block in interphase. After thymidine wash-out, cells were cultured in DMEM with 10% FBS for 3 hours before addition of 100nM Taxol or 100ng/ml nocodazole for 18 hours.

10.2.4 Drug treatments

The Aurora B kinase inhibitor ZM447439 was used at a final concentration of 2μM. In addition the proteasome inhibitor MG132 was added at a final concentration of 10μM to prevent cells from precociously exiting mitosis. Fisetin, a Cdk1 inhibitor, was added to a final concentration 10μM.

10.2.5 siRNA transfection

HeLa cells were transfected with duplex siRNAs at 50% confluency. Oligofectamine and siRNA were separately diluted in Opti-MEM I and incubated for 20 min at room temperature. Oligofectamine and siRNA were combined and incubated for another 20 min. Cells were washed with Opti-MEM I media and Oligofectamine/siRNA mixture was added for 4 hours. Afterwards, the transfection mixture was replaced with DMEM with 10% FBS. Cells were analyzed for down-regulation of protein expression 30 hours and 48 hours after start of transfection,.

Sgo2 SmartPool siRNA was obtained from Dharmacom. All other siRNAs were synthesized using the Silencer siRNA construction kit from Ambion according to manufacturer's instructions. The Sgo2 control siRNA was based on the Sgo2 sequenced and contained point mutations (5'-AATAATGCCATGTTGTGGTGC-3'). Primers for siRNAs against Sgo1, Bub1, and BubR1 were designed based on published sequences (Sgo1 [133], BubR1 [117], Bub1[138]).

10.2.6 Retrovirus packing and transduction

Retroviral particles were produced in the GPG-293 packing cell line, which was maintained in DMEM media supplemented with 10% FBS, $1\mu g/ml$ tetracycline, $2\mu g/ml$ puromycin, and $300\mu g/ml$ G418. The gene of interest was cloned into the retroviral packing vector pMX and the vector was transfected into GPG-293 cells using Mirus293 transfection reagent. For transfection, GPG-293 cells were grown on a 10cm dish to 50% confluency and pre-fed with DMEM media with 10% FBS one hour before transfection. $800\mu l$ Opti-MEM media was mixed with $24\mu l$ Mirus reagent and incubated for 20 min at room temperature. $8\mu g$ of plasmid DNA was added and incubated for another 20 min before addition to the cells. Media was exchanged on the next morning (day 2) and on day 3.5. Media containing retroviral particles was collected on day 5, 7, and 9.

For transduction, HeLa cells were incubated with retroviral supernatant supplemented with $8\mu g/ml$ polybrene for 6 hours.

10.2.7 Generation of murine embryonic fibroblasts (MEFs)

For ES cell feeder layers, murine embryonic fibroblasts were prepared from mice expressing neomycin resistance gene (Neo^r). To accomplish this, pregnant females were sacrificed 13.5 to 15.5 days *post coitum*, the uterus was isolated, and individual embryos were dissected out. The embryos were rinsed several times in PBS. Under the microscope, the head and inner organs were removed from the embryo and the carcass was placed in 2.5ml 0.25% trypsin-EDTA for 10 min at 37°C. The trypsinized cells were filtered through a 100μm cell strainer into 15ml DMEM + 10%FBS and plated onto a 10cm dish. When cells reached confluency, they were split in a 1:5 ratio or frozen away.

10.2.8 Generation of MEF feeder layers for ES cells

To avoid differentiation, murine ES cells are grown on mitotically inactivated MEF feeder layers. For each electroporation experiment, 18 T-175 flasks of MEFs were grown. Frozen MEFs were thawed out under shaking in a water bath at 37°C, diluted into 25ml of MEF media, and spun down at 1000rpm for 5 min to remove the DMSO. The media was aspirated and the pellet resuspended in 50ml of MEF media and plated into two T-175 flasks. When cells reached confluency, MEFs were rinsed twice with HEPES saline and trypsinized with 2ml 0.25% trypsin+2ml HEPES saline for 2-3 min at 37°C. MEFs were pipetted up and down for complete resuspension, transferred to a 15ml tube, and centrifuged at 100rpm for 5 min. Afterwards, media was aspirated, cells resuspended in MEF media and plated to 3 new T-175 flasks. MEFs were cultured at 37°C and 5% CO_2. For mitotic inactivation, cells were trypsinized as described above and 6 T-175 flasks were pooled into one 50ml Falcon tube. MEFs were γ-irradiated using a Cobalt source for 3500rads and frozen down in aliquots of 1/4 or ½ T-175 flasks.

10.2.9 J1 ES cell culture

ES cells were cultured on mitotically inactivated MEF feeder layers. One day before thawing of ES cells, a T-75 flask was coated with 5ml of 0.2% gelatin for 5 min. After 5 min, the gelatin was aspirated and one vial of mitotically inactivated MEFs in ES media was plated on the gelatin. The next day, one vial

of J1 ES cells was thawed out under shaking in a water bath at 37°C, diluted into 10ml of ES cells media supplemented with leukemia inhibitory factor (LIF), and spun down to remove the DMSO. The media was aspirated from the MEFs and ES cells, the ES cells were resuspended in 10ml, and plated onto the MEFs. ES cells were cultured at 37°C and 5% CO_2. When ES cells reached 50-60% confluency, they were split. ES cells were rinsed twice with HEPES saline, 1ml of 0.25% trypsin was added, and cells were incubated for 90s at 37°C. Using a plugged Pasteur pipet, the ES cells were dissociated by pipetting up and down and returned for another 2 min to 37°C. ES cells were resuspended in 7ml ES media plus LIF, centrifuged for 5 min at 1000rpm, media was aspirated, and ES cells were plated onto five T-75 flasks containing MEF feeder layers. ES cells were fed each day with ES media plus LIF.

10.2.10 Freezing of ES cells

For freezing, ES cells were trypsinzed as described above, spun down, media was aspirated, and cells equal to one T-75 were resuspended in 2.5ml of ES media plus LIF. An equal volume of 2x freezing media was added to the cells and 1ml of this mixture was aliquoted into freezing vials on ice. Freezing vials were transferred to a Styrofoam box and placed at -80°C. After two days, vials were transferred to liquid-nitrogen for long-term storage.

10.2.11 Electroporation of ES cells

The day before electroporation, MEF feeder cells were plated on to eight gelatin-treated 10cm dishes. One hour before electroporation, ES cells were fed with fresh ES media plus LIF and fresh electroporation buffer was prepared. For the electroporation, ES cells were trypsinzed as described above, the pellet was washed once more with ES media plus LIF, and ES cells were collected by centrifugation at 1000rpm for 5 min. The cell pellet was resuspended in 10ml electroporation buffer and the cell number was counted. ES cells were centrifuged at 1000rpm for 5 min and resuspended in electroporation buffer at a concentration of $1X10^7$ cells/ml. The linearized targeting construct was added to the ES cells at a final concentration of 25µg/ml. Into each electroporation cuvette, 0.8ml of ES cell/DNA mixture was added. ES cells were electroporated

at $25\mu F$ and 400V. Afterwards, ES cells were transferred to 6ml of media and 2ml were plated onto 10cm dished with MEF feeder cells in fresh ES media plus LIF. ES cells were incubated for 24 hours at $37^\circ C$ and 5% CO_2, before $300\mu M$ G418 was added to the culture. 48 hours post-transfection, $0.2\mu M$ FIAU was added in addition to G418. ES cells were cultured in ES media plus LIF, G418 and FIAU until picking of colonies was started.

10.2.12 Picking of ES cells colonies

Picking of ES cell colonies started 7 days after electroporation. On the day before, MEF feeders were plated on 24-well plates coated with gelatin. One hour before picking, ES cells were fed with ES cell media plus LIF and G418. Clones were identified by eye and circled with a marker on the bottom of the plate. The media was aspirated from the ES cells and replaced with HEPES saline. Under a dissection scope in a tissue culture hood, ES cell colonies were dislodged from the plate, pipetted up, and resuspended in a round-bottom 96-well plate containing 0.25% Trypsin-EDTA. Trypsinized cells were plated onto MEF feeders in 24-well plates. When ES cells reached 80% confluency, ES cells were trypsinzed, 2/3 of the cells were mixed with 2x freezing media and frozen down and the remaining 1/3 was plated onto a 12-well dish without gelatin or feeder for harvesting DNA.

10.2.13 Expansion of ES cells clones for blastocyte injection

Clones that were positive for homologous recombination were expanded for injection into blastocytes at the Transgenic Core Facility of the Brigham and Women's Hospital, Boston. ES cell clones were thawed out on feeder cells into one well of a 6-well dish and grown until they reached 80% confluency. They were then trypsinized and replated into a T-75 flask with feeder cells. When the T-75 flask was confluent, ES cells were frozen down into six aliquots. One day before injection, one vial of ES cells was thawed out into two wells of a 6-well plate only treated with gelatin. On the day of the injection, ES cells were pre-fed, trypsinized, once washed with ES media with LIF, collected by centrifugation at 1000rpm for 5 min, and resuspended on 1ml of ES cell media plus LIF.

10.2.14 Monoclonal antibody

For immunization mice were challenged every 21 days with the antigen of interest. After three injections, mice were bled and the serum was tested for immune response. Positive animals were injected one more time and four days later used for fusion. The day before the fusion, macrophage feeder cells were prepared. To do this, mice were euthanized and the skin was removed from the peritoneal cavity. 5ml cold 0.34M sucrose solution was injected with a 27 gauge needle intraperitoneal. Macrophages were dislodged from the peritoneal cavity by shaking the mouse. Afterwards the sucrose solution containing the macrophages was collected with an 18 gauge needle and diluted into DMEM media containing 10% FBS. In general, macrophages from one mouse were plated over five 96-well plates. For the fusion, NSO-1 myeloma cells were fed and dislodged from the plate by clapping in the morning. After a few hours recovery, the cells were collected, counted, and wash with serum-free DMEM. The spleen was removed from the animal and disrupted under agitation and up and down pipetting in serum-free DMEM. The cell suspension was filtered though a 40μm mesh net into a 50ml Falcon tube to remove cell debris and the cell number was determined. NSO-1 myeloma and spleen cells were mixed in a 1 to 4 ratio and collected by centrifugation. The media was aspirated and the cell pellet mixed and disturbed by tapping the Falcon tube. In a 37$°$C water bath, 0.5ml of PEG1500 was slowly added to the cells over 60s. For the next 90s cells were incubated in the water bath under slow swirling. PEG1500 was diluted out by addition of 20ml serum-free DMEM over 2 min to 5 min while incubating the cells in a 37$°$C water bath. The first 5ml of DMEM was added drop by drop. After the fusion, the cell suspension was diluted into 150ml HAT media and plated over 10 96-well plates containing macrophage feeder cells (150μL per well). After 7 to 10 days clones were screened by immunofluorescence for antibody expression. Positive clones were sub-cloned and expanded.

10.2.15 Polyclonal antibody

For immunization mice were challenged every 21 days with the antigen of interest. After three injections, mice were bled and the serum was tested for

immune response. Positive animals were euthanized and blood was collected. After coagulation, serum was removed and stored at -80°C.

10.2.16 FACS

30 hours after transfection with control, Sgo1, or Sgo2 siRNA, cells were collected and fixed in 70% ethanol. Total cellular DNA content was determined by flow cytometric analysis after washing fixed cells in PBS, followed by incubation with 250 μg/ml RNAse A and 10 μg/ml propidium iodide in PBS for 1hr at room temperature. Cells stained with propidium iodide were analyzed on a FACScalibur flow cytometer (Becton-Dickinson, San Jose, CA) using Cellquest software.

10.2.17 Microtubule pelleting assay

For microtubule spindown, Taxol arrested HeLa cells were collected, lysed and the lysate was cleared of debris by a high speed spin. Cleared lysates were supplemented with 0.5mM MgGTP, 2mM MgATP, or 2mM MgAMPPNP, and warmed to room temperature. 20μM Taxol was added and the lysates were incubated at 37°C for 30 min. Afterwards, polymerized tubulin was pelleted though a 1M sucrose cushion in BRB80 buffer, containing 0.5mM MgATP and 10μM Taxol. Lysate, supernatant and pellet were analyzed by Western Blot.

11. References

1. Yang, A., et al., *p63, a p53 homolog at 3q27-29, encodes multiple products with transactivating, death-inducing, and dominant-negative activities.* Mol Cell, 1998. **2**(3): p. 305-16.
2. Augustin, M., et al., *Cloning and chromosomal mapping of the human p53-related KET gene to chromosome 3q27 and its murine homolog Ket to mouse chromosome 16.* Mamm Genome, 1998. **9**(11): p. 899-902.
3. Osada, M., et al., *Cloning and functional analysis of human p51, which structurally and functionally resembles p53.* Nat Med, 1998. **4**(7): p. 839-43.
4. Hibi, K., et al., *AIS is an oncogene amplified in squamous cell carcinoma.* Proc Natl Acad Sci U S A, 2000. **97**(10): p. 5462-7.
5. Kaghad, M., et al., *Monoallelically expressed gene related to p53 at 1p36, a region frequently deleted in neuroblastoma and other human cancers.* Cell, 1997. **90**(4): p. 809-19.
6. Shimada, A., et al., *The transcriptional activities of p53 and its homologue p51/p63: similarities and differences.* Cancer Res, 1999. **59**(12): p. 2781-6.
7. Ishida, S., et al., *Adenovirus-mediated transfer of p53-related genes induces apoptosis of human cancer cells.* Jpn J Cancer Res, 2000. **91**(2): p. 174-80.
8. Levrero, M., et al., *The p53/p63/p73 family of transcription factors: overlapping and distinct functions.* J Cell Sci, 2000. **113 (Pt 10)**: p. 1661-70.
9. Mills, A.A., et al., *p63 is a p53 homologue required for limb and epidermal morphogenesis.* Nature, 1999. **398**(6729): p. 708-13.
10. Yang, A., et al., *p63 is essential for regenerative proliferation in limb, craniofacial and epithelial development.* Nature, 1999. **398**(6729): p. 714-8.
11. Zheng, B., A.A. Mills, and A. Bradley, *A system for rapid generation of coat color-tagged knockouts and defined chromosomal rearrangements in mice.* Nucleic Acids Res, 1999. **27**(11): p. 2354-60.
12. Koster, M.I., et al., *p63 is the molecular switch for initiation of an epithelial stratification program.* Genes Dev, 2004. **18**(2): p. 126-31.
13. Bamberger, C. and H. Schmale, *Identification and tissue distribution of novel KET/p63 splice variants.* FEBS Lett, 2001. **501**(2-3): p. 121-6.
14. Yang, A. and F. McKeon, *P63 and P73: P53 mimics, menaces and more.* Nat Rev Mol Cell Biol, 2000. **1**(3): p. 199-207.
15. Serber, Z., et al., *A C-terminal inhibitory domain controls the activity of p63 by an intramolecular mechanism.* Mol Cell Biol, 2002. **22**(24): p. 8601-11.
16. Schultz, J., et al., *SAM as a protein interaction domain involved in developmental regulation.* Protein Sci, 1997. **6**(1): p. 249-53.
17. Kurita, T., et al., *Differential expression of p63 isoforms in female reproductive organs.* Mech Dev, 2005. **122**(9): p. 1043-55.
18. Byrne, C., M. Tainsky, and E. Fuchs, *Programming gene expression in developing epidermis.* Development, 1994. **120**(9): p. 2369-83.

19. Fuchs, E. and C. Byrne, *The epidermis: rising to the surface.* Curr Opin Genet Dev, 1994. **4**(5): p. 725-36.

20. Alonso, L. and E. Fuchs, *Stem cells of the skin epithelium.* Proc Natl Acad Sci U S A, 2003. **100 Suppl 1**: p. 11830-5.

21. Rochat, A., K. Kobayashi, and Y. Barrandon, *Location of stem cells of human hair follicles by clonal analysis.* Cell, 1994. **76**(6): p. 1063-73.

22. Lechler, T. and E. Fuchs, *Asymmetric cell divisions promote stratification and differentiation of mammalian skin.* Nature, 2005. **437**(7056): p. 275-80.

23. Blanpain, C. and E. Fuchs, *Epidermal Stem Cells of the Skin.* Annu Rev Cell Dev Biol, 2005.

24. Presland, R.B., et al., *Characterization of the human epidermal profilaggrin gene. Genomic organization and identification of an S-100-like calcium binding domain at the amino terminus.* J Biol Chem, 1992. **267**(33): p. 23772-81.

25. Markova, N.G., et al., *Profilaggrin is a major epidermal calcium-binding protein.* Mol Cell Biol, 1993. **13**(1): p. 613-25.

26. Rice, R.H., et al., *Keratinocyte differentiation markers: involucrin, transglutaminase, and toxicity.* J Natl Cancer Inst Monogr, 1992(13): p. 87-91.

27. Gandarillas, A., *Epidermal differentiation, apoptosis, and senescence: common pathways?* Exp Gerontol, 2000. **35**(1): p. 53-62.

28. Potten, C.S., *Epidermal transit times.* Br J Dermatol, 1975. **93**(6): p. 649-58.

29. Carroll, D.K., et al., *p63 regulates an adhesion programme and cell survival in epithelial cells.* Nat Cell Biol, 2006. **8**(6): p. 551-61.

30. De Felici, M., et al., *Establishment of oocyte population in the fetal ovary: primordial germ cell proliferation and oocyte programmed cell death.* Reprod Biomed Online, 2005. **10**(2): p. 182-91.

31. Barlow, C., et al., *Atm deficiency results in severe meiotic disruption as early as leptonema of prophase I.* Development, 1998. **125**(20): p. 4007-17.

32. de Vries, S.S., et al., *Mouse MutS-like protein Msh5 is required for proper chromosome synapsis in male and female meiosis.* Genes Dev, 1999. **13**(5): p. 523-31.

33. Edelmann, W., et al., *Mammalian MutS homologue 5 is required for chromosome pairing in meiosis.* Nat Genet, 1999. **21**(1): p. 123-7.

34. Yoshida, K., et al., *The mouse RecA-like gene Dmc1 is required for homologous chromosome synapsis during meiosis.* Mol Cell, 1998. **1**(5): p. 707-18.

35. Zinn, A.R. and J.L. Ross, *Turner syndrome and haploinsufficiency.* Curr Opin Genet Dev, 1998. **8**(3): p. 322-7.

36. Modi, D.N., S. Sane, and D. Bhartiya, *Accelerated germ cell apoptosis in sex chromosome aneuploid fetal human gonads.* Mol Hum Reprod, 2003. **9**(4): p. 219-25.

37. Gilbert, S.F., *Developmental Biology.* 6 ed. 2000, Sunderland: Sinauer Associates, Inc.

38. Roop, D.R., et al., *Transcriptional control of high molecular weight keratin gene expression in multistage mouse skin carcinogenesis.* Cancer Res, 1988. **48**(11): p. 3245-52.

39. Sun, T.T., et al., *Keratin classes: molecular markers for different types of epithelial differentiation.* J Invest Dermatol, 1983. **81**(1 Suppl): p. 109s-15s.

40. Mehrel, T., et al., *Identification of a major keratinocyte cell envelope protein, loricrin.* Cell, 1990. **61**(6): p. 1103-12.

41. Dale, B.A., J.D. Lonsdale-Eccles, and K.A. Holbrook, *Stratum corneum basic protein: an interfilamentous matrix protein of epidermal keratin.* Curr Probl Dermatol, 1980. **10**: p. 311-25.

42. Rothnagel, J.A., et al., *The gene for mouse epidermal filaggrin precursor. Its partial characterization, expression, and sequence of a repeating filaggrin unit.* J Biol Chem, 1987. **262**(32): p. 15643-8.

43. Koster, M.I., S. Kim, and D.R. Roop, *P63 deficiency: a failure of lineage commitment or stem cell maintenance?* J Investig Dermatol Symp Proc, 2005. **10**(2): p. 118-23.

44. Calautti, E., et al., *fyn tyrosine kinase is involved in keratinocyte differentiation control.* Genes Dev, 1995. **9**(18): p. 2279-91.

45. Pellegrini, G., et al., *p63 identifies keratinocyte stem cells.* Proc Natl Acad Sci U S A, 2001. **98**(6): p. 3156-61.

46. McKeon, F., *p63 and the epithelial stem cell: more than status quo?* Genes Dev, 2004. **18**(5): p. 465-9.

47. Keyes, W.M., et al., *p63 deficiency activates a program of cellular senescence and leads to accelerated aging.* Genes Dev, 2005. **19**(17): p. 1986-99.

48. Leube, R.E. and T.J. Rustad, *Squamous cell metaplasia in the human lung: molecular characteristics of epithelial stratification.* Virchows Arch B Cell Pathol Incl Mol Pathol, 1991. **61**(4): p. 227-53.

49. Koster, M.I. and D.R. Roop, *Transgenic mouse models provide new insights into the role of p63 in epidermal development.* Cell Cycle, 2004. **3**(4): p. 411-3.

50. Candi, E., et al., *Differential roles of p63 isoforms in epidermal development: selective genetic complementation in p63 null mice.* Cell Death Differ, 2006. **13**(6): p. 1037-47.

51. van Bokhoven, H. and F. McKeon, *Mutations in the p53 homolog p63: allele-specific developmental syndromes in humans.* Trends Mol Med, 2002. **8**(3): p. 133-9.

52. van Bokhoven, H., et al., *p63 Gene mutations in eec syndrome, limb-mammary syndrome, and isolated split hand-split foot malformation suggest a genotype-phenotype correlation.* Am J Hum Genet, 2001. **69**(3): p. 481-92.

53. Celli, J., et al., *Heterozygous germline mutations in the p53 homolog p63 are the cause of EEC syndrome.* Cell, 1999. **99**(2): p. 143-53.

54. McGrath, J.A., et al., *Hay-Wells syndrome is caused by heterozygous missense mutations in the SAM domain of p63.* Hum Mol Genet, 2001. **10**(3): p. 221-9.

55. van Bokhoven, H., *p63 mutations in eec, hay-wells, adult syndromes and in split hand/foot malformation reveal a genotype-phenotype correlation.* Am J Hum Genet, 2000. **67** (Supplement 2, abstract 149).

56. Amiel, J., et al., *TP63 gene mutation in ADULT syndrome.* Eur J Hum Genet, 2001. **9**(8): p. 642-5.

57. Flores, E.R., et al., *p63 and p73 are required for p53-dependent apoptosis in response to DNA damage.* Nature, 2002. **416**(6880): p. 560-4.

58. Flores, E.R., et al., *Tumor predisposition in mice mutant for p63 and p73: evidence for broader tumor suppressor functions for the p53 family.* Cancer Cell, 2005. **7**(4): p. 363-73.

59. Zaika, A.I., et al., *DeltaNp73, a dominant-negative inhibitor of wild type p53 and TAp73, is up-regulated in human tumors.* J Exp Med, 2002. **196**(6): p. 765-80.

60. Park, B.J., et al., *Frequent alteration of p63 expression in human primary bladder carcinomas.* Cancer Res, 2000. **60**(13): p. 3370-4.

61. Pozniak, C.D., et al., *An anti-apoptotic role for the p53 family member, p73, during developmental neuron death.* Science, 2000. **289**(5477): p. 304-6.

62. Li, N., et al., *TA-p63-gamma regulates expression of DeltaN-p63 in a manner that is sensitive to p53.* Oncogene, 2006. **25**(16): p. 2349-59.

63. Bamberger, C., et al., *Expression of different p63 variants in healing skin wounds suggests a role of p63 in reepithelialization and muscle repair.* Wound Repair Regen, 2005. **13**(1): p. 41-50.

64. Ince, T.A., et al., *p63 Coordinates anogenital modeling and epithelial cell differentiation in the developing female urogenital tract.* Am J Pathol, 2002. **161**(4): p. 1111-7.

65. eds Heim, S.M., F, *Cancer Cytogenetics* Wiley Liss Inc., New York, 1995.

66. Flemming, W., *Zur Kenntnis der Zelle und ihrer Theilungserscheinungen.* Schr. naturwiss. Verein Schleswig-Holstein, 1878. **3**: p. 23-27.

67. Boveri, T., *Ueber mehrpolige Mitosen als Mittel zur Analyse des Zellkerns.* Verh. d. phys.med. Ges. Wuerzburg N.F., 1902. **35**: p. 67-90.

68. Flemming, W., *Zellsubstanz, Kern und Zelltheilung.* F.C.W. Vogel, Leipzig, 1882.

69. Paweletz, N., *Walther Flemming: pioneer of mitosis research.* Nat Rev Mol Cell Biol, 2001. **2**(1): p. 72-5.

70. van Hansemann, D., *Ueber asymmetrische Zellteilung in epithelkrebsen und deren biologischer Bedeutung.* Virschows Arch. Pathol. Anat., 1890. **119**: p. 299-326.

71. Boveri, T., *Zur Frage der Entstehung maligner Tumoren.* Gustav Fischer Verlag, 1914.

72. Lodish, H., et al., *Molecular Cell Biology.* 4 ed. 2000: W. H. Freeman.

73. Alberts, B., et al., *Molecular Biology of the Cell.* 4 ed. 2002, New York: Garland Science.

74. Murray, A.W., *Recycling the cell cycle: cyclins revisited.* Cell, 2004. **116**(2): p. 221-34.

75. Hunt, T., *Maturation promoting factor, cyclin and the control of M-phase.* Curr Opin Cell Biol, 1989. **1**(2): p. 268-74.

76. Maller, J., et al., *Maturation-promoting factor and the regulation of the cell cycle.* J Cell Sci Suppl, 1989. **12**: p. 53-63.

77. Nurse, P., *Genetic control of cell size at cell division in yeast.* Nature, 1975. **256**(5518): p. 547-51.

78. Masui, Y. and C.L. Markert, *Cytoplasmic control of nuclear behavior during meiotic maturation of frog oocytes.* J Exp Zool, 1971. **177**(2): p. 129-45.

79. Smith, L.D. and R.E. Ecker, *The interaction of steroids with Rana pipiens Oocytes in the induction of maturation.* Dev Biol, 1971. **25**(2): p. 232-47.

80. Moreno, S., J. Hayles, and P. Nurse, *Regulation of p34cdc2 protein kinase during mitosis.* Cell, 1989. **58**(2): p. 361-72.

81. Pines, J. and T. Hunter, *Human cyclins A and B1 are differentially located in the cell and undergo cell cycle-dependent nuclear transport.* J Cell Biol, 1991. **115**(1): p. 1-17.

82. Li, J., A.N. Meyer, and D.J. Donoghue, *Nuclear localization of cyclin B1 mediates its biological activity and is regulated by phosphorylation.* Proc Natl Acad Sci U S A, 1997. **94**(2): p. 502-7.

83. King, R.W., et al., *A 20S complex containing CDC27 and CDC16 catalyzes the mitosis-specific conjugation of ubiquitin to cyclin B.* Cell, 1995. **81**(2): p. 279-88.

84. Fang, G., H. Yu, and M.W. Kirschner, *The checkpoint protein MAD2 and the mitotic regulator CDC20 form a ternary complex with the anaphase-promoting complex to control anaphase initiation.* Genes Dev, 1998. **12**(12): p. 1871-83.

85. Golan, A., Y. Yudkovsky, and A. Hershko, *The cyclin-ubiquitin ligase activity of cyclosome/APC is jointly activated by protein kinases Cdk1-cyclin B and Plk.* J Biol Chem, 2002. **277**(18): p. 15552-7.

86. Kotani, S., et al., *PKA and MPF-activated polo-like kinase regulate anaphase-promoting complex activity and mitosis progression.* Mol Cell, 1998. **1**(3): p. 371-80.

87. Rudner, A.D. and A.W. Murray, *Phosphorylation by Cdc28 activates the Cdc20-dependent activity of the anaphase-promoting complex.* J Cell Biol, 2000. **149**(7): p. 1377-90.

88. Kraft, C., et al., *Mitotic regulation of the human anaphase-promoting complex by phosphorylation.* Embo J, 2003. **22**(24): p. 6598-609.

89. Ciosk, R., et al., *An ESP1/PDS1 complex regulates loss of sister chromatid cohesion at the metaphase to anaphase transition in yeast.* Cell, 1998. **93**(6): p. 1067-76.

90. Zou, H., et al., *Identification of a vertebrate sister-chromatid separation inhibitor involved in transformation and tumorigenesis.* Science, 1999. **285**(5426): p. 418-22.

91. Hwang, L.H., et al., *Budding yeast Cdc20: a target of the spindle checkpoint.* Science, 1998. **279**(5353): p. 1041-4.

92. Sudakin, V., G.K. Chan, and T.J. Yen, *Checkpoint inhibition of the APC/C in HeLa cells is mediated by a complex of BUBR1, BUB3, CDC20, and MAD2.* J Cell Biol, 2001. **154**(5): p. 925-36.

93. Pinsky, B.A. and S. Biggins, *The spindle checkpoint: tension versus attachment.* Trends Cell Biol, 2005. **15**(9): p. 486-93.

94. Nicklas, R.B. and C.A. Staehly, *Chromosome micromanipulation. I. The mechanics of chromosome attachment to the spindle.* Chromosoma, 1967. **21**(1): p. 1-16.

95. Ostergren, G., *The mechanism of co-orientation in bivalents and multivalents.* Hereditas, 1951. **37**: p. 85-156.

96.   Nicklas, R.B., *Mitosis.* Adv Cell Biol, 1971. **2**: p. 225-97.

97.   Rieder, C.L., *The formation, structure, and composition of the mammalian kinetochore and kinetochore fiber.* Int Rev Cytol, 1982. **79**: p. 1-58.

98.   Mitchison, T. and M. Kirschner, *Dynamic instability of microtubule growth.* Nature, 1984. **312**(5991): p. 237-42.

99.   Nicklas, R.B., *Chance encounters and precision in mitosis.* J Cell Sci, 1988. **89 (Pt 3)**: p. 283-5.

100.   Li, R. and A.W. Murray, *Feedback control of mitosis in budding yeast.* Cell, 1991. **66**(3): p. 519-31.

101.   Hoyt, M.A., L. Totis, and B.T. Roberts, *S. cerevisiae genes required for cell cycle arrest in response to loss of microtubule function.* Cell, 1991. **66**(3): p. 507-17.

102.   Weiss, E. and M. Winey, *The Saccharomyces cerevisiae spindle pole body duplication gene MPS1 is part of a mitotic checkpoint.* J Cell Biol, 1996. **132**(1-2): p. 111-23.

103.   Taylor, S.S. and F. McKeon, *Kinetochore localization of murine Bub1 is required for normal mitotic timing and checkpoint response to spindle damage.* Cell, 1997. **89**(5): p. 727-35.

104.   Taylor, S.S., E. Ha, and F. McKeon, *The human homologue of Bub3 is required for kinetochore localization of Bub1 and a Mad3/Bub1-related protein kinase.* J Cell Biol, 1998. **142**(1): p. 1-11.

105.   Jin, D.Y., F. Spencer, and K.T. Jeang, *Human T cell leukemia virus type 1 oncoprotein Tax targets the human mitotic checkpoint protein MAD1.* Cell, 1998. **93**(1): p. 81-91.

106.   Li, Y. and R. Benezra, *Identification of a human mitotic checkpoint gene: hsMAD2.* Science, 1996. **274**(5285): p. 246-8.

107.   Abrieu, A., et al., *Mps1 is a kinetochore-associated kinase essential for the vertebrate mitotic checkpoint.* Cell, 2001. **106**(1): p. 83-93.

108.   Rieder, C.L., et al., *Anaphase onset in vertebrate somatic cells is controlled by a checkpoint that monitors sister kinetochore attachment to the spindle.* J Cell Biol, 1994. **127**(5): p. 1301-10.

109.   Waters, J.C., et al., *Localization of Mad2 to kinetochores depends on microtubule attachment, not tension.* J Cell Biol, 1998. **141**(5): p. 1181-91.

110.   Meraldi, P. and P.K. Sorger, *A dual role for Bub1 in the spindle checkpoint and chromosome congression.* Embo J, 2005. **24**(8): p. 1621-33.

111.   Bernard, P., J.F. Maure, and J.P. Javerzat, *Fission yeast Bub1 is essential in setting up the meiotic pattern of chromosome segregation.* Nat Cell Biol, 2001. **3**(5): p. 522-6.

112.   Kitajima, T.S., S.A. Kawashima, and Y. Watanabe, *The conserved kinetochore protein shugoshin protects centromeric cohesion during meiosis.* Nature, 2004. **427**(6974): p. 510-7.

113.   Sharp-Baker, H. and R.H. Chen, *Spindle checkpoint protein Bub1 is required for kinetochore localization of Mad1, Mad2, Bub3, and CENP-E, independently of its kinase activity.* J Cell Biol, 2001. **153**(6): p. 1239-50.

114. Johnson, V.L., et al., *Bub1 is required for kinetochore localization of BubR1, Cenp-E, Cenp-F and Mad2, and chromosome congression.* J Cell Sci, 2004. **117**(Pt 8): p. 1577-89.

115. Tang, Z., et al., *Phosphorylation of Cdc20 by Bub1 provides a catalytic mechanism for APC/C inhibition by the spindle checkpoint.* Mol Cell, 2004. **16**(3): p. 387-97.

116. Chen, R.H., et al., *Spindle checkpoint protein Xmad1 recruits Xmad2 to unattached kinetochores.* J Cell Biol, 1998. **143**(2): p. 283-95.

117. Chen, R.H., et al., *The spindle checkpoint of budding yeast depends on a tight complex between the Mad1 and Mad2 proteins.* Mol Biol Cell, 1999. **10**(8): p. 2607-18.

118. Lampson, M.A. and T.M. Kapoor, *The human mitotic checkpoint protein BubR1 regulates chromosome-spindle attachments.* Nat Cell Biol, 2005. **7**(1): p. 93-8.

119. Mao, Y., A. Abrieu, and D.W. Cleveland, *Activating and silencing the mitotic checkpoint through CENP-E-dependent activation/inactivation of BubR1.* Cell, 2003. **114**(1): p. 87-98.

120. Pfleger, C.M. and M.W. Kirschner, *The KEN box: an APC recognition signal distinct from the D box targeted by Cdh1.* Genes Dev, 2000. **14**(6): p. 655-65.

121. Tanaka, T., et al., *Cohesin ensures bipolar attachment of microtubules to sister centromeres and resists their precocious separation.* Nat Cell Biol, 2000. **2**(8): p. 492-9.

122. Dewar, H., et al., *Tension between two kinetochores suffices for their bi-orientation on the mitotic spindle.* Nature, 2004. **428**(6978): p. 93-7.

123. Nasmyth, K., *Disseminating the genome: joining, resolving, and separating sister chromatids during mitosis and meiosis.* Annu Rev Genet, 2001. **35**: p. 673-745.

124. Uhlmann, F., *Chromosome cohesion and separation: from men and molecules.* Curr Biol, 2003. **13**(3): p. R104-14.

125. Gruber, S., C.H. Haering, and K. Nasmyth, *Chromosomal cohesin forms a ring.* Cell, 2003. **112**(6): p. 765-77.

126. Gimenez-Abian, J.F., et al., *Regulation of sister chromatid cohesion between chromosome arms.* Curr Biol, 2004. **14**(13): p. 1187-93.

127. Hauf, S., et al., *Dissociation of cohesin from chromosome arms and loss of arm cohesion during early mitosis depends on phosphorylation of SA2.* PLoS Biol, 2005. **3**(3): p. e69.

128. Uhlmann, F., F. Lottspeich, and K. Nasmyth, *Sister-chromatid separation at anaphase onset is promoted by cleavage of the cohesin subunit Scc1.* Nature, 1999. **400**(6739): p. 37-42.

129. Kerrebrock, A.W., et al., *The Drosophila mei-S332 gene promotes sister-chromatid cohesion in meiosis following kinetochore differentiation.* Genetics, 1992. **130**(4): p. 827-41.

130. Miyazaki, W.Y. and T.L. Orr-Weaver, *Sister-chromatid misbehavior in Drosophila ord mutants.* Genetics, 1992. **132**(4): p. 1047-61.

131. Marston, A.L., et al., *A genome-wide screen identifies genes required for centromeric cohesion.* Science, 2004. **303**(5662): p. 1367-70.

132. Rabitsch, K.P., et al., *Two fission yeast homologs of Drosophila Mei-S332 are required for chromosome segregation during meiosis I and II.* Curr Biol, 2004. **14**(4): p. 287-301.

133. Erickson, J. and D.L. Hartl, *Cytogenetic analysis of homozygous segregation distorter males of Drosophila melanogaster.* Can J Genet Cytol, 1976. **18**(2): p. 287-96.

134. Salic, A., J.C. Waters, and T.J. Mitchison, *Vertebrate shugoshin links sister centromere cohesion and kinetochore microtubule stability in mitosis.* Cell, 2004. **118**(5): p. 567-78.

135. Clarke, A.S., et al., *POLO kinase regulates the Drosophila centromere cohesion protein MEI-S332.* Dev Cell, 2005. **8**(1): p. 53-64.

136. Kitajima, T.S., et al., *Shugoshin collaborates with protein phosphatase 2A to protect cohesin.* Nature, 2006. **441**(7089): p. 46-52.

137. McGuinness, B.E., et al., *Shugoshin prevents dissociation of cohesin from centromeres during mitosis in vertebrate cells.* PLoS Biol, 2005. **3**(3): p. e86.

138. Kitajima, T.S., et al., *Human Bub1 defines the persistent cohesion site along the mitotic chromosome by affecting Shugoshin localization.* Curr Biol, 2005. **15**(4): p. 353-9.

139. Tang, Z., et al., *Human Bub1 protects centromeric sister-chromatid cohesion through Shugoshin during mitosis.* Proc Natl Acad Sci U S A, 2004. **101**(52): p. 18012-7.

140. Indjeian, V.B., B.M. Stern, and A.W. Murray, *The centromeric protein Sgo1 is required to sense lack of tension on mitotic chromosomes.* Science, 2005. **307**(5706): p. 130-3.

141. Resnick, T.D., et al., *INCENP and Aurora B promote meiotic sister chromatid cohesion through localization of the Shugoshin MEI-S332 in Drosophila.* Dev Cell, 2006. **11**(1): p. 57-68.

142. Biggins, S. and A.W. Murray, *The budding yeast protein kinase Ipl1/Aurora allows the absence of tension to activate the spindle checkpoint.* Genes Dev, 2001. **15**(23): p. 3118-29.

143. Cheeseman, I.M., et al., *Phospho-regulation of kinetochore-microtubule attachments by the Aurora kinase Ipl1p.* Cell, 2002. **111**(2): p. 163-72.

144. Biggins, S., et al., *The conserved protein kinase Ipl1 regulates microtubule binding to kinetochores in budding yeast.* Genes Dev, 1999. **13**(5): p. 532-44.

145. Tanaka, T.U., et al., *Evidence that the Ipl1-Sli15 (Aurora kinase-INCENP) complex promotes chromosome bi-orientation by altering kinetochore-spindle pole connections.* Cell, 2002. **108**(3): p. 317-29.

146. Hauf, S., et al., *The small molecule Hesperadin reveals a role for Aurora B in correcting kinetochore-microtubule attachment and in maintaining the spindle assembly checkpoint.* J Cell Biol, 2003. **161**(2): p. 281-94.

147. Riedel, C.G., et al., *Protein phosphatase 2A protects centromeric sister chromatid cohesion during meiosis I.* Nature, 2006. **441**(7089): p. 53-61.

148. Tang, Z., et al., *PP2A is required for centromeric localization of Sgo1 and proper chromosome segregation.* Dev Cell, 2006. **10**(5): p. 575-85.

149. Blom, N., S. Gammeltoft, and S. Brunak, *Sequence and structure-based prediction of eukaryotic protein phosphorylation sites.* J Mol Biol, 1999. **294**(5): p. 1351-62.

150. Obenauer, J.C., L.C. Cantley, and M.B. Yaffe, *Scansite 2.0: Proteome-wide prediction of cell signaling interactions using short sequence motifs.* Nucleic Acids Res, 2003. **31**(13): p. 3635-41.

151. Ong, S.E., et al., *Stable isotope labeling by amino acids in cell culture, SILAC, as a simple and accurate approach to expression proteomics.* Mol Cell Proteomics, 2002. **1**(5): p. 376-86.

152. Blagoev, B., et al., *A proteomics strategy to elucidate functional protein-protein interactions applied to EGF signaling.* Nat Biotechnol, 2003. **21**(3): p. 315-8.

153. Barr, F.A., H.H. Sillje, and E.A. Nigg, *Polo-like kinases and the orchestration of cell division.* Nat Rev Mol Cell Biol, 2004. **5**(6): p. 429-40.

154. Gray, N.S., et al., *Exploiting chemical libraries, structure, and genomics in the search for kinase inhibitors.* Science, 1998. **281**(5376): p. 533-8.

155. Gregan, J., et al., *Novel genes required for meiotic chromosome segregation are identified by a high-throughput knockout screen in fission yeast.* Curr Biol, 2005. **15**(18): p. 1663-9.

156. DeLuca, J.G., et al., *Nuf2 and Hec1 are required for retention of the checkpoint proteins Mad1 and Mad2 to kinetochores.* Curr Biol, 2003. **13**(23): p. 2103-9.

157. Mitchison, T.J. and E.D. Salmon, *Poleward kinetochore fiber movement occurs during both metaphase and anaphase-A in newt lung cell mitosis.* J Cell Biol, 1992. **119**(3): p. 569-82.

158. Skibbens, R.V., V.P. Skeen, and E.D. Salmon, *Directional instability of kinetochore motility during chromosome congression and segregation in mitotic newt lung cells: a push-pull mechanism.* J Cell Biol, 1993. **122**(4): p. 859-75.

159. Rieder, C.L. and E.D. Salmon, *Motile kinetochores and polar ejection forces dictate chromosome position on the vertebrate mitotic spindle.* J Cell Biol, 1994. **124**(3): p. 223-33.

160. Roos, U.P., *Light and electron microscopy of rat kangaroo cells in mitosis. III. Patterns of chromosome behavior during prometaphase.* Chromosoma, 1976. **54**(4): p. 363-85.

161. Ault, J.G. and C.L. Rieder, *Chromosome mal-orientation and reorientation during mitosis.* Cell Motil Cytoskeleton, 1992. **22**(3): p. 155-9.

162. Mayer, T.U., et al., *Small molecule inhibitor of mitotic spindle bipolarity identified in a phenotype-based screen.* Science, 1999. **286**(5441): p. 971-4.

163. King, R.W., et al., *How proteolysis drives the cell cycle.* Science, 1996. **274**(5293): p. 1652-9.

164. Kapoor, T.M., et al., *Probing spindle assembly mechanisms with monastrol, a small molecule inhibitor of the mitotic kinesin, Eg5.* J Cell Biol, 2000. **150**(5): p. 975-88.

165. Heim, S.M., F, *Cancer Cytogenetics* Wiley Liss Inc., New York, 1995.

166. Rancati, G., et al., *Mad3/BubR1 phosphorylation during spindle checkpoint activation depends on both Polo and Aurora kinases in budding yeast.* Cell Cycle, 2005. **4**(7): p. 972-80.

167. Laemmli, U.K., *Cleavage of structural proteins during the assembly of the head of bacteriophage T4.* Nature, 1970. **227**(5259): p. 680-5.

168. Davis, B.J., *Disc Electrophoresis. Ii. Method and Application to Human Serum Proteins.* Ann N Y Acad Sci, 1964. **121**: p. 404-27.

169. Ornstein, L., *Disc Electrophoresis. I. Background and Theory.* Ann N Y Acad Sci, 1964. **121**: p. 321-49.

170. Towbin, H., T. Staehelin, and J. Gordon, *Electrophoretic transfer of proteins from polyacrylamide gels to nitrocellulose sheets: procedure and some applications.* Proc Natl Acad Sci U S A, 1979. **76**(9): p. 4350-4.

12.   Publications

Gerber S.A., Kettenbach A., Rush J., and Gygi S.P. (2006). **The Absolute Quantification Strategy. Application to Phosphorylation Profiling of Human Separase Serine 1126.** Methods in Molecular Biology, vol. 359: Quantitative Proteomics by Mass Spectrometry. (in print 2006)

The work presented in this thesis is summarized in the manuscript: "Sgo2 Establishes an Inter-Kinetochore Geometry Necessary for Accurate Chromosome Segregation".

Kettenbach A., Gerber S.A., Waters J.C., Gygi S.P., and McKeon F. (2006). **Sgo2 Establishes an Inter-Kinetochore Geometry Necessary for Accurate Chromosome Segregation.** (submitted 2006).

The in this thesis described investigation of the epidermal phenotype the

TA-p63 (-/-) mouse is part of the submitted manuscript "Isoform-selective Knockout Reveals an Essential role of ∆N-p63 in Epithelial Stem Cells".

Pinto F., Kettenbach A., Senoo M., Yang A., Zhu Z., Church G., Struhl K., Crum C.P., and McKeon F., (2006). **Isoform-selective Knockout Reveals an Essential Role of ∆N-p63 in Epithelial Stem Cells.** (submitted 2006).

Analysis of the effects of γ-irradiation on oocyte cell death in TA-p63 (-/-) contributed to the submitted manuscript "p63 Protects the Female Germline during Meiotic Arrest".

Suh E., Yang A., Kettenbach A., Bamberger C., Michaelis A., Zhu Z., Ervin J., Crum C.P., and McKeon F. (2006). p63 Protects the Female Germline during Meiotic Arrest. (submitted 2006).

13.   Acknowledgements

So that is now it! And the only thing left for me to do is to thank everybody for their help and support in the last three and a half years.

The first person I would like to thank is my supervisor, Prof. Frank McKeon, for his support, guidance, enthusiasm, and encouragement through out my thesis. Most of what I learned in the lab, I learned from him.

I would like to thank Annie Yang for working together, especially for the many hours spent in the ES cell room, for correcting my writing attempts that finally led to this thesis, and for dealing with all of my other frustrations.

I would like to thank Karen Easley for keeping us all supplied and organized and for all her help in general.

I would like to thank Prof. Volker Doetsch for collaborating, being on my thesis committee, and of course not to forget Mario and Mazdak.

I would like thank Prof. Hans-Georg Rammensee for representing this work in front of the "Fakultaet fuer Chemie und Pharmazie".

I would like to thank Prof. Peter Ruth and Prof. Thilo Stehle for being on my thesis committee.

I would like to thank my mom, Angelika Kettenbach, for her support though out my studies.

Thanks also go to all those who gave me the possibility to complete this thesis.

And finally, I would like to thank Scott Gerber for collaborating inside and outside the lab.

14.   Academic teachers

Academic teachers at the Eberhard-Karls-Universitaet, Tuebingen

Prof. Albert, Prof. Bisswanger, Prof. Bohley, Prof. Brendle, Prof. Eisele,
Prof. Gauglitz, Prof. Grabmayer, Prof. Hagenmaier, Prof. Hamprecht, Prof.
Hoffmann, Prof. Jung, Prof. Lindner, Prof. Maier, Prof. Mecke, Prof. Nakel,
Prof. Ninnemann, Prof. Nordheim, Prof. Oberhammer, Prof. Pfeiffer, PD Dr.
Pommer, Prof. Poralla, Prof. Probst, Prof. Rammensee, Prof. Reutter,
Prof. Schurig, Prof. Schwarz, Prof. Dr. Stevanovic, PD Dr. Stoeva, Prof.
Voelter,
Prof. Weber, Prof. Weser, Prof. Wiesinger, Prof. Wohlleben.

Academic teachers at the Harvard Medical School, Boston

Prof. Frank McKeon

__Lebenslauf__

Arminja Nadine Kettenbach
76 South St#3
Jamaica Plain, MA 02130, USA
E-mail: akettenb@fas.harvard.edu
Telefone: 617-515-6554

__Geboren:__   2. Januar 1978 in Wiesbaden-Sonnenberg, Deutschland

__Studium:__

März 2003-heute	**Anfertigung der Doktorarbeit** Arbeitsgruppe von Prof. Frank McKeon Institut fuer Zellbiologie Harvard Medical School Boston, MA 02115, USA
Jan. 2003-Feb. 2003	Mitarbeit in der Arbeitsgruppe von Prof. Nordheim Interfakultäres Institut fuer Zellbiologie Abteilung Molekularbiologie Eberhard-Karls-Universität 72076 Tübingen, Deutschland
Dez. 2002	**Diplom Biochemie**
Mai 2002-Dez. 2002	**Diplomarbeit** in der Arbeitsgruppe von Prof. Nordheim Interfakultäres Institut fuer Zellbiologie Abteilung Molekularbiologie Eberhard-Karls-Universität 72076 Tübingen, Deutschland
Dez. 2001- April 2002	Muendliche Diplompruefungen (Biochemie, Organische Chemie, Zellbiologie)
April 2000	**Vordiplom Biochemie**
Okt. 1997-Dez. 2002	**Studium der Biochemie** an der Eberhard-Karls Universtät Tübingen

__Stipendien:__

Okt. 1998- Dez. 2002	Konrad-Adenauer Stiftung
Okt. 2000- Dez. 2002	Studienstiftung des dt. Volkes

Auslandsaufenthalte:

Juli 1999- Sep.1999 Mitarbeit in der Arbeitsgruppe von Prof. Koeffler
         Cedars-Sinai Medical Center
         UCLA
         Los Angles, CA 90048, USA

Sep. 2000-Oct. 2001 Arbeitsgruppe von Prof. Frank McKeon
         Institut fuer Zellbiologie
         Harvard Medical School
         Boston, MA 02115, US